91

LBNL-40886
UC-000

ERNEST ORLANDO LAWRENCE
BERKELEY NATIONAL LABORATORY

Evaluation of Mo-SiO_2 Continuous FGM's

A.P. Tomsia, R.M. Cannon, J.M. McNaney,
H. Ishibashi, E. Saiz, W. MoberlyChan,
T.J. Becker, and R.O. Ritchie

Materials Sciences Division
Center for Advanced Materials

September 1997

LBNL-40886

Evaluation of Mo-SiO_2 Continuous FGM's

A. P. Tomsia

R. M. Cannon, J. M. McNaney, H. Ishibashi, E. Saiz
W. MoberlyChan, T. J. Becker and R. O. Ritchie

Center for Advanced Materials
Materials Sciences Division
Lawrence Berkeley National Laboratory
Berkeley, CA 94720

September 1997

FINAL REPORT

This work was sponsored by the TOTO Ltd., (Contract No. BG9600300) through the U. S. Department of Energy under contract No. DE-AC03-76SF00098.

List of Contents

		Page
	Introduction	3
	Background	3
1	Processing	4
1.1	Characteristics of Mo Powder	4
1.2	Characterization of Mo powder	6
1.3	Mo Powder in water	7
1.4	Differential Thermal Analysis (DTA) and Thermogravimetric Analysis (TG) of Mo powders	9
2	SEM Analysis	12
3	FGM Properties	19
3.1	Electrical Properties	19
3.2	Hardness and Toughness	24
3.3	Bending Tests and Thermal Cycling	27
3.4	Thermal Expansion	29
4	TEM Analysis	36
5	Residual Stresses	41
6	Mechanical Strength	62
6.1	Statistical Treatment of Strength	62
6.2	Strength Testing	63
6.3	Batch Three Tests	65
6.4	Batch Four Tests	66
6.5	Residual Stress Effects	67
6.6	Slow Crack Growth Effects	68
6.7	Conclusions	70
7	Summary	71

Evaluation of Mo-SiO_2 Continuous FGM's

A. P. Tomsia

R. M. Cannon, J. M. McNaney, H. Ishibashi, E. Saiz, W. MoberlyChan, T. J. Becker and R. O. Ritchie

Introduction

The TOTO sponsored program at LBL involved characterization of continuous Mo-SiO_2 FGMs in terms of microstructure, mechanical and thermal properties and corrosion resistance which would relate to the steady state, high temperature performance as well as the heating and cooling transients that occur at the beginning and end of operation in various applications.

Background

A *functionally graded material* (FGM) is one in which composition, microstructure and properties vary continuously across the material. Such materials can be useful in applications where different properties are needed at different surfaces and where reducing the residual and applied stress distributions is critical for functionality and lifetime improvement. Although such structures have been developed heuristically, the desire to develop unified concepts for FGM design is relatively new and has prompted reformulation of key questions regarding design principles to yield materials with optimal performance and reliability.

Examples where FGM structures could be useful include: 1) joining of dissimilar materials, e.g., ceramics with superalloys for gas turbines or for turbocharger rotor-to-shaft, 2) bonding electrodes to electrolytes, as for fuel cells, 3) creating structures with thermal barriers, such as high speed air foils, 4) bonding electrodes to insulating containments, as for high energy lamps, and 5) forming environmentally compatible transition layers, as for biomaterial implants. Many of interest to TOTO entail *high temperature* applications of *metal-ceramic* combinations.

Superior properties could derive from optimization of the microstructure, from independent control of the attainable gradients, and from greater flexibility in the types of materials that can be fabricated. However, the fundamental principles required to guide the design of this class of materials (i.e., regarding the microstructural variables) for optimum mechanical behavior, largely, have not been articulated. This requires an understanding of the effects of key variables on the mechanical and thermophysical properties and the ability to control them. These variables are: 1) the smoothness of the gradient, i.e., the particle or grain size of the constituents, 2) the steepness relative to the macroscopic dimensions, 3) the degree of interconnectedness of the two phases, and 4) the anisotropies of the microstructure and properties, and 5) the residual stresses.

Research programs are, thus, needed to systematically develop and verify theory and models for the relevant mechanical responses, projects which the structural materials groups in MSD at LBL have initiated under TOTO sponsorship. However, such work depends upon the existence of exacting fabrication methods to reliably produce desired materials.

The work performed at LBNL evaluated the TOTO FGM materials both in terms of strength and the fracture resistance at room temperature and correlated the properties with detailed microstructure characteristics that relate back to processing methods. The materials were largely made at TOTO and some effects of processing were examined at LBL. Extensive microstructural and phase analysis was accomplished at LBL. The mechanical test methods that were used are modifications of those for which experience exists both for testing homogeneous materials, and for testing layered materials, particularly ceramic/metal/ceramic sandwich configurations. The strength is ultimately the quantity that controls component lifetime, but it depends upon: 1) the fracture resistance (toughness), which depends upon microstructure and composition, 2) on the flaw population which reflects internal flaws left from the specific fabrication methods and surface flaws from machining and polishing, 3) residual stresses and 4) stress concentrations from material gradients. The strengths will undoubtably be statistically variable. Thus, reliable design required testing an adequate number of samples to characterize the pertinent flaw populations, and an extreme-value statistical analysis suitable for the specific geometries. With the graded materials, further research is required to select, refine and verify the proper statistical procedures.

An additional objective of this research was to provide guidance for the refined design of these FGM materials, which depends in particular on the large and fine scale gradients. This required explicitly addressing the effects of the gradients on discontinuities on residual stresses, and the resultant effects of these on microcracking and fracture statistics. Minimization or optimization of the thermal mismatch stresses will require gradients on the order of the size of the piece. In addition, it is important to address the stress concentrations that arose near edges owing to changes in compliance as well as thermal properties. In multilayer materials, these often dictate behavior. Smaller gradients can be helpful in ameliorating these effects. Finally, for particle composites, the effects of local stresses on microcracking and toughness are pertinent. Evaluations were accomplished with a combination of analytical and finite element models (FEM).

1. Processing

1.1. Characteristics of Mo Powder

Molybdenum metal is resistant to many chemicals - especially hydrochloric, hydrofluoric, phosphoric and sulfuric acids - over a wide range of temperatures and concentrations. There is practically no attack at ordinary pressures in hydrochloric acid regardless of temperature and concentration; but, under pressure at 190°C, molybdenum shows a moderately low corrosion rate of 0.01-0.02 in./yr for all concentrations between 1 and 37% HCl. The presence of air or an oxidizing agent causes a pronounced increase in

the rate of corrosion. For example, 0.5% $FeCl_3$ is sufficient to cause a hundred-fold increase in the rate of attack in hydrochloric acid. Molybdenum resists boiling sulfuric acid up to a concentration of 60%. Under pressure at 190 and 250°C, however, it shows some attack with the rates becoming excessive at concentrations over 70% at 190°C and over about 20% at 250°C. In boiling phosphoric acid, the molybdenum has very low corrosion rates for concentrations of 1 to 85%. Under pressure at 190°C, on the other hand, the molybdenum is attacked more rapidly in weaker than in the more concentrated solutions with rates of about 0.01-0.02 in./yr up to 40% H_3PO_4 and progressively decreasing rates at higher concentrations. Molybdenum is rapidly attacked by oxidizing acids, such as nitric acid and aqua regia, as well as by molten salts, such as potassium nitrate and fused alkalis. It resists most liquid metals, such as potassium, sodium, bismuth, lithium, magnesium and mercury.

Molybdenum begins to oxidize in air at 300°C. The oxidation proceeds by a two-step process with molybdenum dioxide (MoO_2) as the thinner inner layer and molybdenum trioxide (MoO_3) as the outer layer. Above 500°C, MoO_3 begins to volatilize, and at 600°C the rate of evaporation of MoO_3 becomes significant. At about 770°C the rate of evaporation of MoO_3 equals its rate of formation, and as temperature increases, the volatilization rate becomes extremely rapid. The ultimate oxidation rate is linear, with the rate-determining step being the oxidation of the dioxide to the trioxide.

Table 1. Reactivity and melting points of molybdenum oxides.

Oxide	Melting Point °C	Color	Reaction with water	Reaction with H_2
MoO_2	1927	brown-black	Reacts, oxidizing to MoO_3	Reacts, 950-1100°C reducing to metallic Mo
Mo_4O_{11}	824±10	red		
Mo_8O_{23}	>700	violet		
Mo_9O_{26}	800±10	violet		
MoO_3	795±2	white	Dissolves slightly, 2 grams/liter	450-470°C, Reacts reducing to MoO_2
MoO_3				800-900°C, Reacts reducing to metallic Mo

MoO_3 reacts with Mo at 580°C reducing to Mo_4O_{11}.
MoO_2 at ~1700°C, in the absence of air, dissociates to form volatile MoO_3 and metallic Mo.

The formation of molten MoO_3 above 815°C results in catastrophically accelerating effect due to the following factors: (a) the liquid oxide flows off the metal surface, (b) the rate of diffusion of oxygen through the liquid phase is high, and (c) the molten oxide can also act as a flux.

The chemistry of molybdenum suggests that a series of oxides should exists, each having a valence number from two to six. Actually, the Mo-O system is complex and not completely defined. Some of the oxides which have been reported are listed in Table 1. Many of these compounds are metastable and are prepared by prolonged heating of stoichiometric mixtures of oxides and metal, followed by quenching.

1.2 Characterization of Mo powder

Two types of powders are currently used by TOTO in the fabrication of FGM's, the powders have average particle sizes 1.5 and 0.7 μm. X-ray diffraction (XRD) analysis of several FGM specimens processed at TOTO revealed the presence of Mo oxide(s) in the Mo-SiO_2 FGMs. This prompted XRD analysis of Mo powder in the "as-received" state and FGMs after various stages of processing. X-ray diffraction analysis of the as-received powders shows only the peaks corresponding to metallic Mo (Fig. 1.1). However, after annealing in vacuum (5×10^{-3} Pa) at 600°C for 2 hours MoO_2 is detected by XRD. The relative size of the oxide peak is bigger for the 0.7 μm powder $I_{MoO2}(-1,1,1)/I_{Mo}(110)= 0.038$ for the 0.7 μm and 0.002 for the 1.5 μm).

Subsequent annealing in 90% Ar+10% H_2 at 600°C, 2 h eliminates the oxide peak. Assuming that all the oxygen was in the form of MoO_2, the weight losses after the H_2 annealing correspond to an oxide content of 1.6 wt % for the 1.5 μm powder and 4.4 wt % for the 0.7 μm powder. There is not a significant difference in weight loss with annealing temperatures in the range 600 to 900°C. Finally, after the H_2 annealing the powder was fired again in vacuum at 600°C for 2 h. After this firing, no MoO_2 peak could be detected by XRD on the 1.5 μm powder and only a small peak in the 0.7 μm powder (Fig. 1.1).

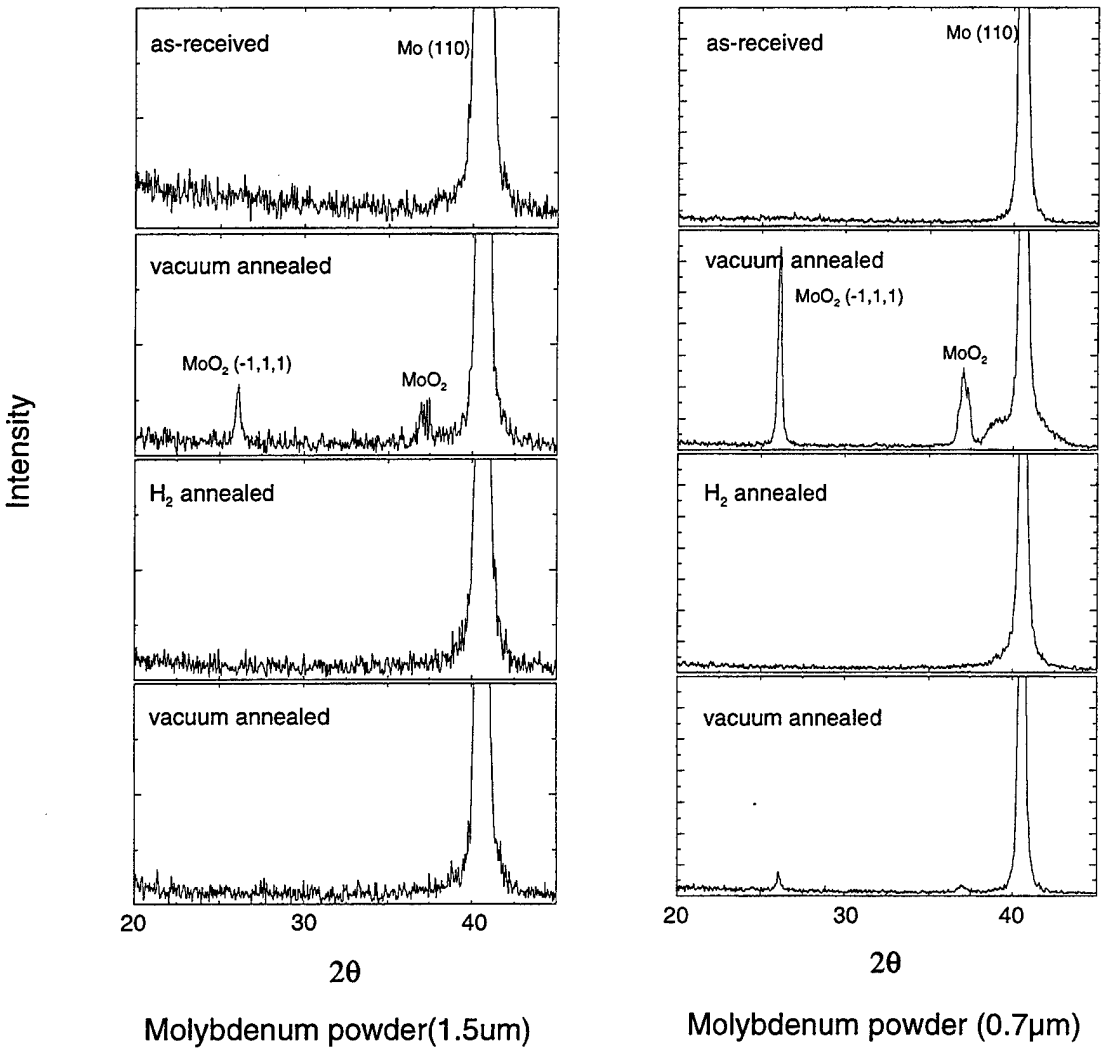

Figure 1.1. XRD of the as-received Mo powders and after different thermal treatments.

The results show that H_2 annealing at temperatures in the range 600-900°C effectively reduces MoO_2. If elimination of the oxide is beneficial for making Mo-SiO_2 FGM, the reducing annealing should be included in the processing schedule (e.g. for the as received powders or during presintering).

1.3 Mo Powder in water

Silica-Mo FGMs are processed by pressure slip casting using water slurries. It is therefore important to study the behavior of Mo powder in water.

The experiments performed with Mo powder immersed in water for about 1 day indicated immediate discoloration of water to blue color, indicative of Mo oxides. The so-called "molybdenum blue" is caused by $Mo_2O_5 \times H_2O$, with varied amounts of Mo and O. The blue solution was decanted from the remaining powder and heated at 90°C to

drive off all the water. The black residue was pressed into pellet and analyzed by XRD (Figure 1.2).

The XRD spectrum indicates that the dissolved compound(s) is amorphous. EDS analysis of the residue revealed only presence of 20 at.% of Mo and 80 at.% of O. The discoloration of water to bluish color would thus indicate that even as-received Mo powder contain small amount of oxides not detected by XRD analysis. EDS analysis of the as-received powder indicates that indeed a small amount of oxygen is present in the powder. During final sintering of the FGM, the oxide remains in the system and may affect FGM properties.

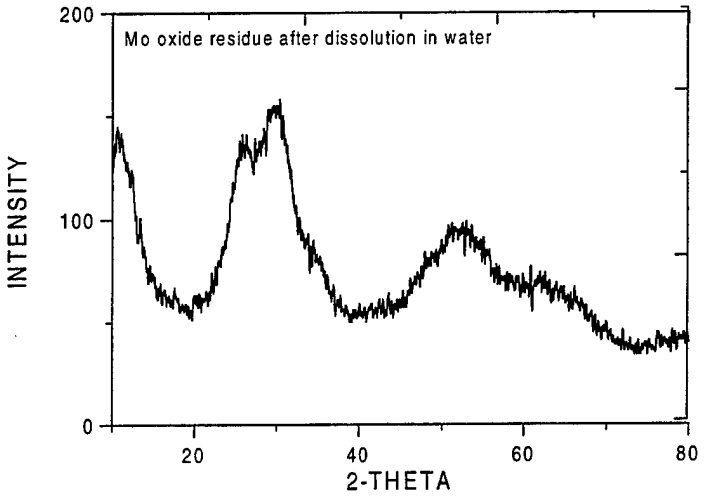

Fig. 1.2. XRD of the Mo oxide deposit dissolved in water

Subsequent experiments were designed to reduce the oxide in green FGM specimen and determine its weight loss. Green FGM specimens processed in TOTO were subjected to heat-treatment in H_2 for 2 h at 600°C. The weight loss (average of 5 specimens) of a green FGM after hydrogen annealing was 0.56%. This corresponds to 5.9% loss recalculated for Mo content in FGM.

In order to study the dissolution of Mo oxides using pH similar to that of the FGM slurry, two solutions with 5 g of Mo in 1 liter of water were kept at constant pH (3 and 5) for 4 - 24 hours and the dissolution rate was measured after 4, 8, 16 and 24 hours. The water used was bi-distilled and the pH was maintained with 0.5N HCl and 0.05N NaOH. The dissolution results are presented in Figure 1.3. The Mo cations in solution were analyzed by ICP using the liquid separated from the solid by centrifugation. The dissolution was more rapid during the initial 4 hours and dropped off to nearly zero in both pH at times ranged between 8 and 16 hours.

The amount of Mo oxide dissolved at pH 3 (~5 wt.%) correlates well with the amount lost during hydrogen annealing of green FGM. We believe, however, that the annealing temperature of 600°C was too low to reduce completely Mo oxides present

after presintering stage. The SEM photos presented later for FGM processed in TOTO and H_2 annealed at LBNL show presence of oxide in both cases, although the amount for H_2 annealed specimen is very small. The values given in Table 1 suggest that if MoO_2 is present, H_2 annealing should be performed >800°C.

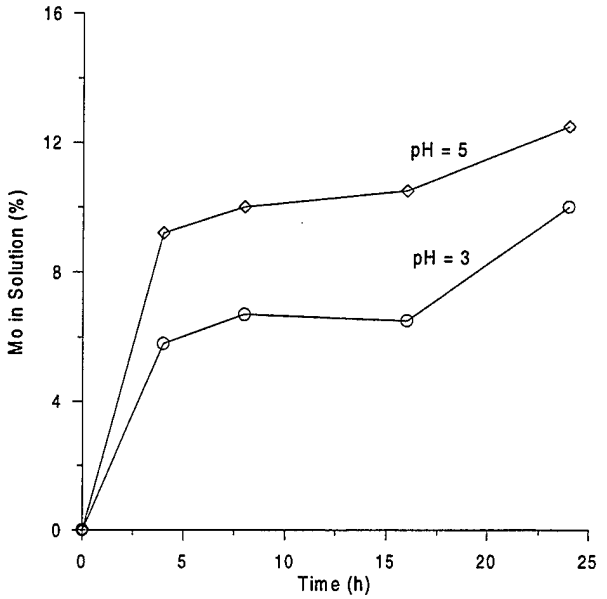

Figure 1.3. Dissolution of Mo oxides at constant pH 3 and 5 at room temperature.

In parallel, as received and H_2 annealed powders were placed in water. For the as received powder a blue coloration could be observed in the water after ~2 h. However, for the H_2 annealed powder the water remained clear for times up to 24 h.

The results of these experiments are consistent with the presence of Mo hydroxide in the as received powders. By annealing in vacuum the hydroxide loses water and turns into oxide that is reduced afterwards by firing in H_2. The experiments (XRD and weight loss) indicate that the amount of oxide is bigger in the 0.7 μm powder. Subsequent vacuum annealing at 600°C reoxidizes the metal slightly. The hydroxide dissolves in water and is the reason for the blue coloration observed after placing as-received powders in water.

1.4 Differential Thermal Analysis (DTA) and Thermogravimetric Analysis (TG) of Mo powders

DTA-TG of the Mo powder was performed from room temperature to 700°C using a mixture of 95%N_2/5%H_2 with a heating rate of 5°C/min (Fig. 1.4). Similar DTA-TG experiments were performed using Ar atmosphere. (Fig. 1.5)

DTA analysis combined with XRD confirmed the presence of $MoO(OH)_2$ hydroxide as an inner layer. After loosing constituent water at about 150°C, this oxide crystallizes at 330°C as observed by the sharp exothermic peak on DTA curve, giving MoO_2, which is in agreement with the XRD pattern. The MoO_3 is reduced to MoO_2 in H_2

atmosphere with a loss of O_2 (~3 wt.%) up to 700°C. The XRD analysis after DTA-TG analysis in N_2/H_2 and Argon is presented in Figure 1.6 and 1.7.

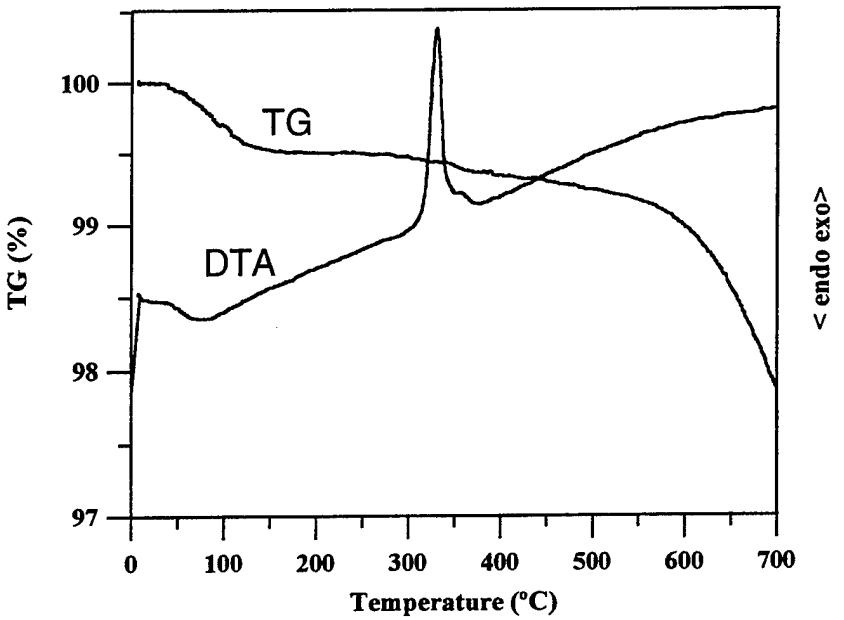

Figure 1.4. DTA-TG of the Mo powder in H_2 atmosphere

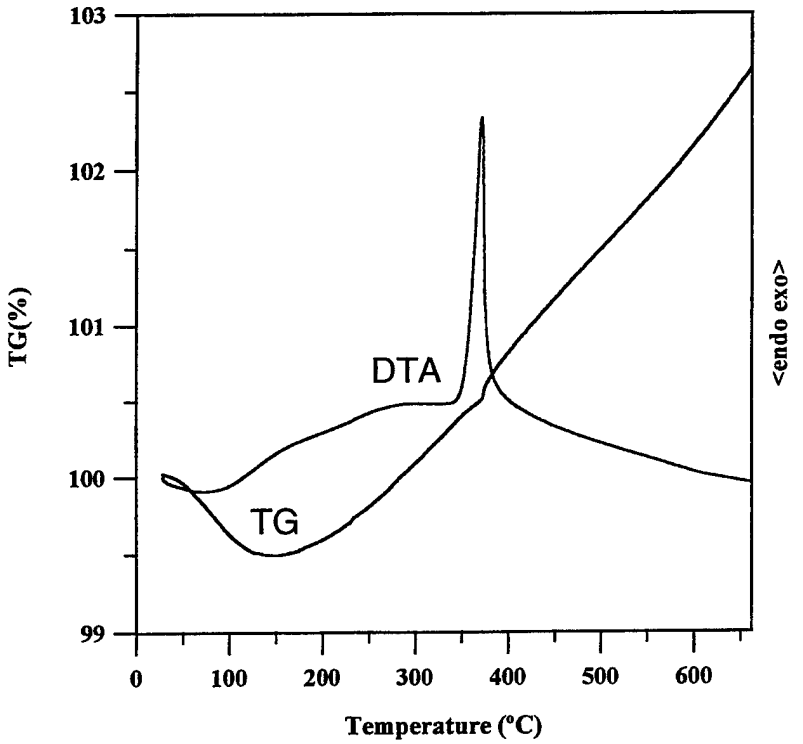

Figure 1.5. DTA-TG of the Mo powder in Ar atmosphere

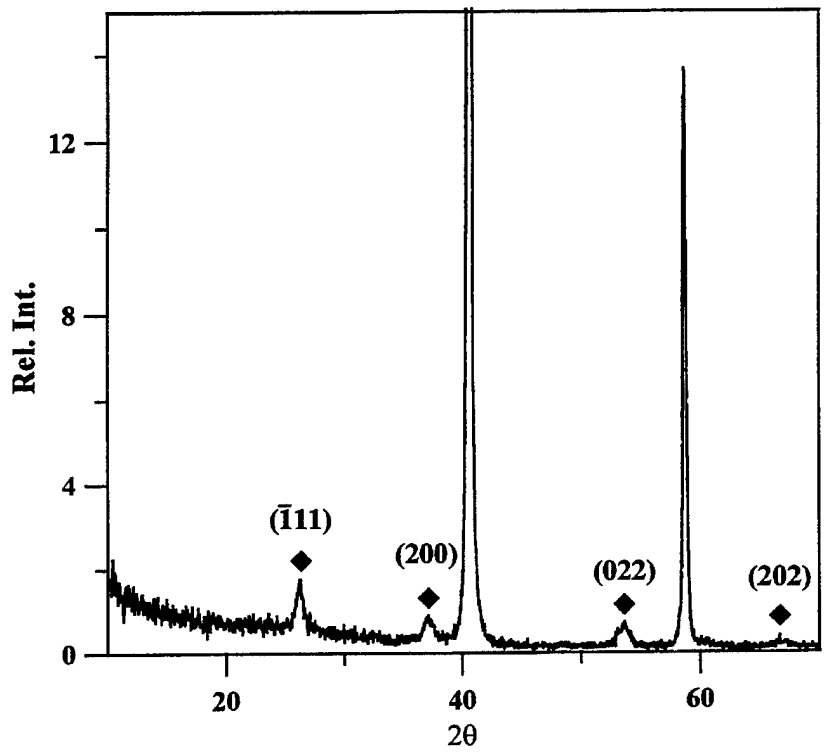

Figure 1.6. XRD pattern obtained from Mo powder subjected to DTA-TG analysis in H_2
◆ = MoO_2

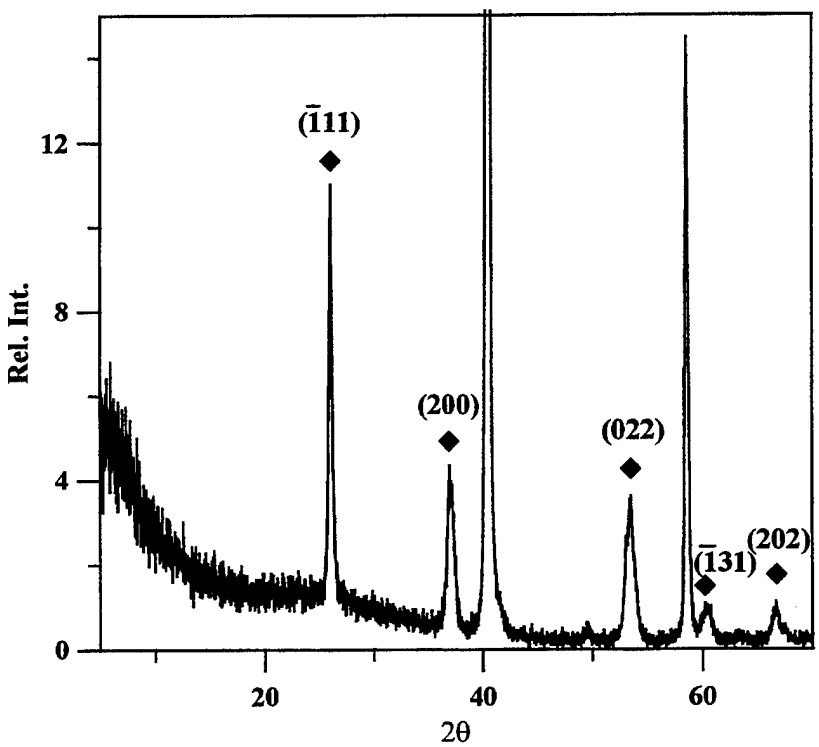

Figure 1.7. XRD pattern obtained from Mo powder subjected to DTA-TG analysis in Ar.
◆ = MoO_2

2. SEM Analysis

SEM and microprobe analysis was used on all materials to characterize the metal particle morphology, the type and extent of any chemical reactions and any tendency for interfacial delamination.

Figures 2.1-2.4 present high resolution SEM images of two types of FGMs. The figure on top is for FGM manufactured at TOTO, and the figure at the bottom shows images for FGM made at LBL, with a 600°C heat treatment in Ar-H_2 atmosphere to reduce Mo oxides present from presintering stage. Four different magnifications are presented, 2000, 5000, 10000, and 20000x. The dark area in the SEM images is SiO_2, the bright particles are Mo, and the grey particles are Mo slightly below the surface and also the Mo oxide phase. The oxide phase is difficult to distinguish because it also contains about 6 wt.% SiO_2, as determined by TEM analysis. The role of this phase on FGM properties has yet to be determined. Several features are evident.

Cracking of the molybdenum and debonding at the Mo-SiO_2 interface is evident for many Mo particles. Analysis of about 300 Mo particles for each specimen showed that interface cracking was observed in about 20-25% of particles for each firing schedule. However, FGMs fired in H_2 have significantly higher amount of Mo particles which are cracked (Figure 2.5). This likely represents the effect of better interface bonding causing cracking of the particles instead of the interface. In contrast, the Mo-oxide/SiO_2 interfaces are rarely cracked.

Figures 2.6 and 2.7 present high resolution SEM images of two types of FGMs. Figure 2.6 is for FGM manufactured at TOTO, and the figure 2.7 shows images for FGM made at LBL, with a 600°C heat treatment in Ar-H_2 atmosphere to reduce Mo oxides present from presintering stage. The figures are similar to those presented above, except the specimens were etched in HF to better reveal the difference between pure Mo and its oxides. The dark area in the SEM images is SiO_2, the bright particles are Mo, and the gray particles are Mo oxides. The oxide phase contains about 6 at.% Si as determined by EDS analysis.

Careful analysis of theses and other images taken at even higher magnifications, indicate several features. The specimens processed at TOTO contain spherical or rounded particles not present in H_2 fired FGMs. This shape plus the presence of silica would indicate that the oxide was molten at the firing temperature and dewetted the molybdenum particle. The Mo oxide(s) probably has a higher thermal expansion coefficient than the other constituents. If a continuous layer remains between grains it would profoundly affect the properties.

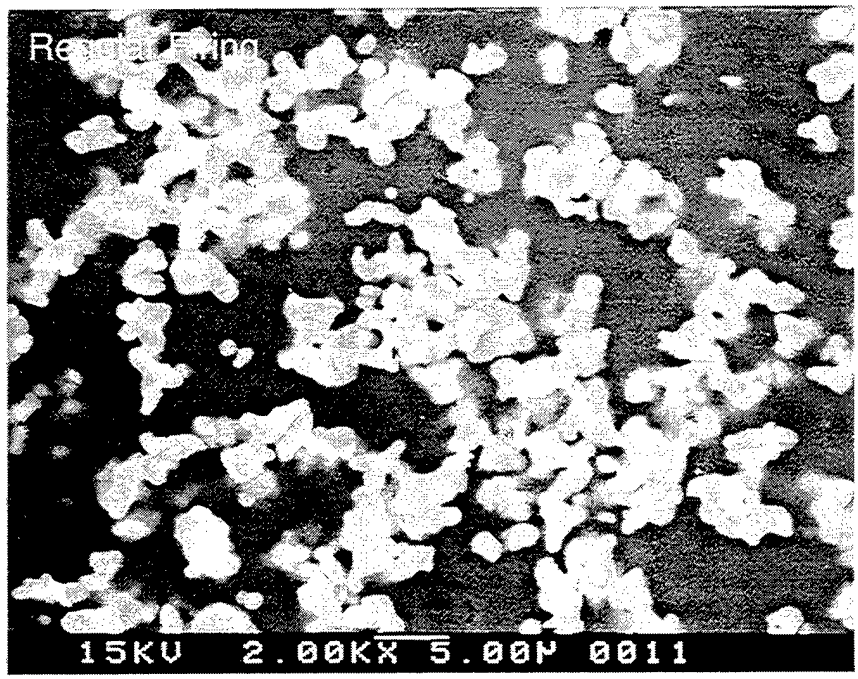

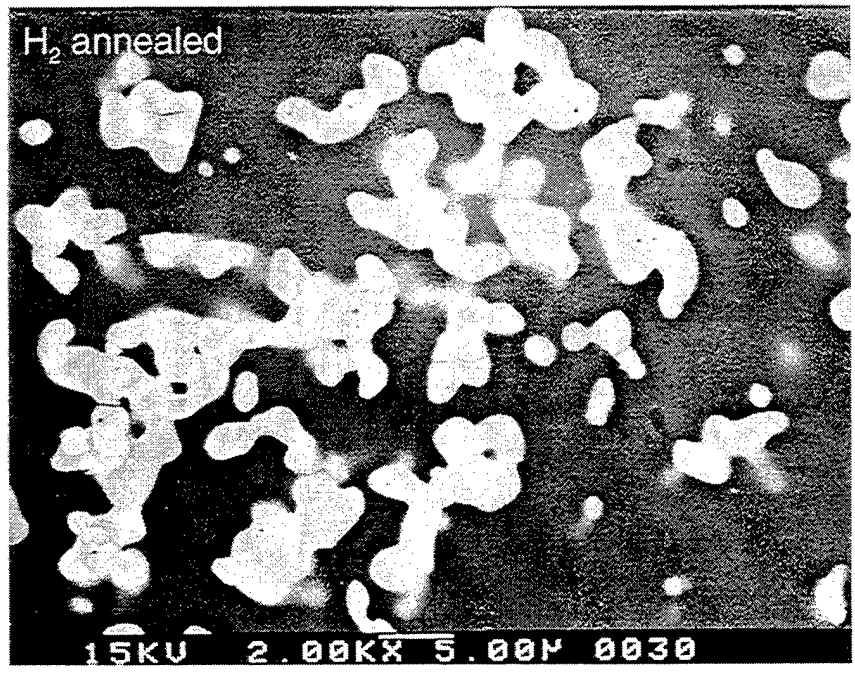

Figures 2.1. SEM images of Mo-SiO_2 FGMs

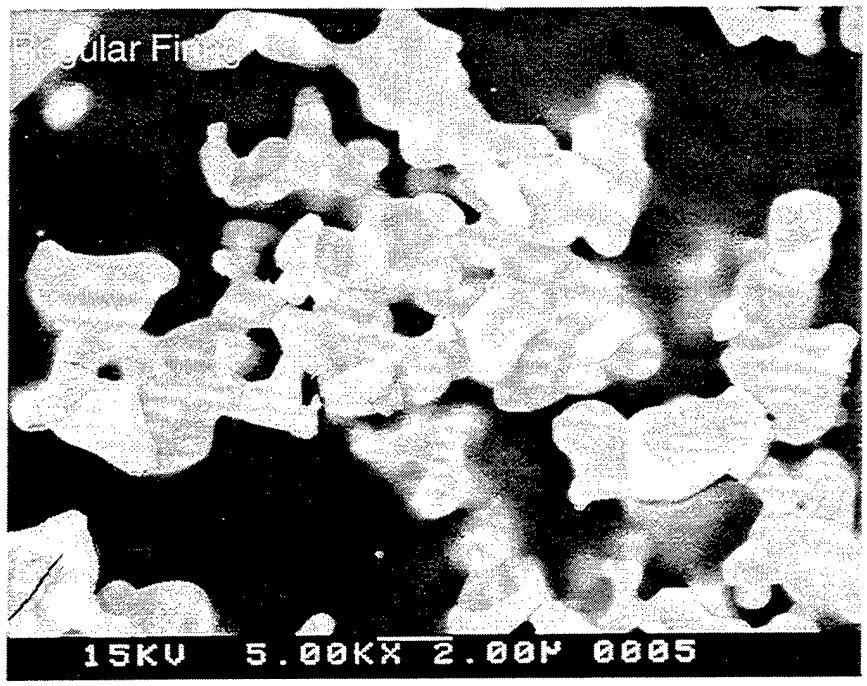

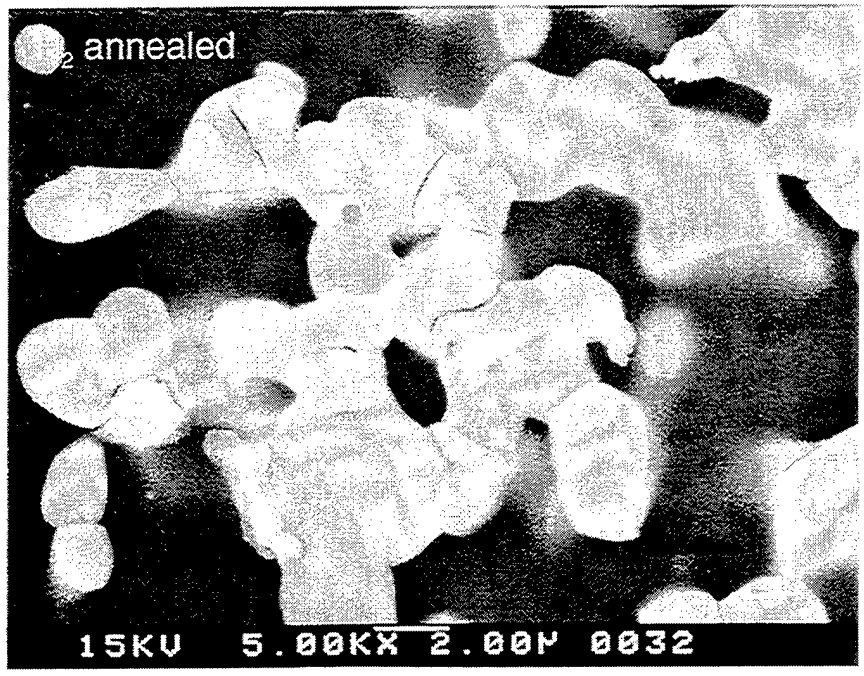

Figures 2.2. SEM images of Mo-SiO_2 FGMs

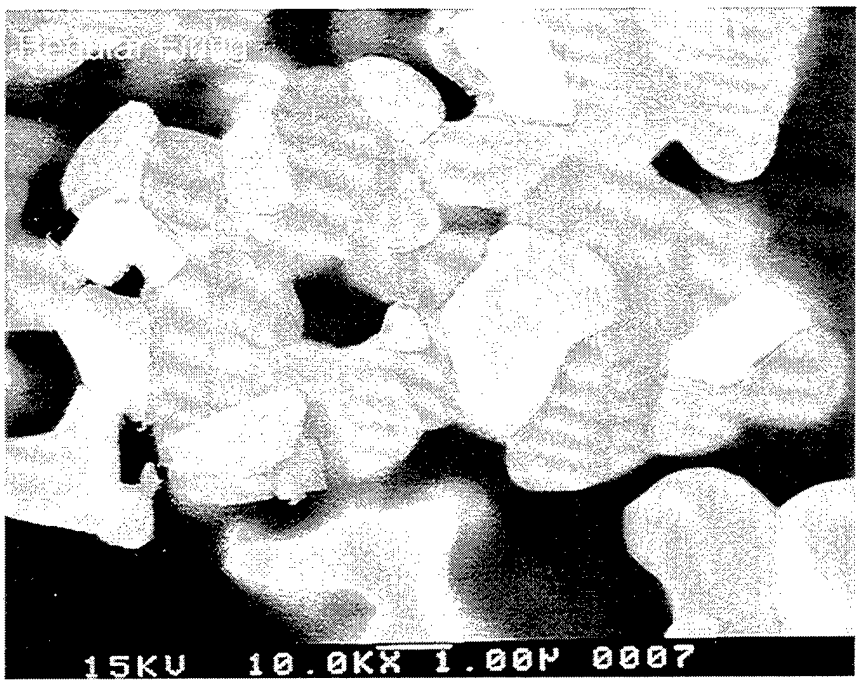

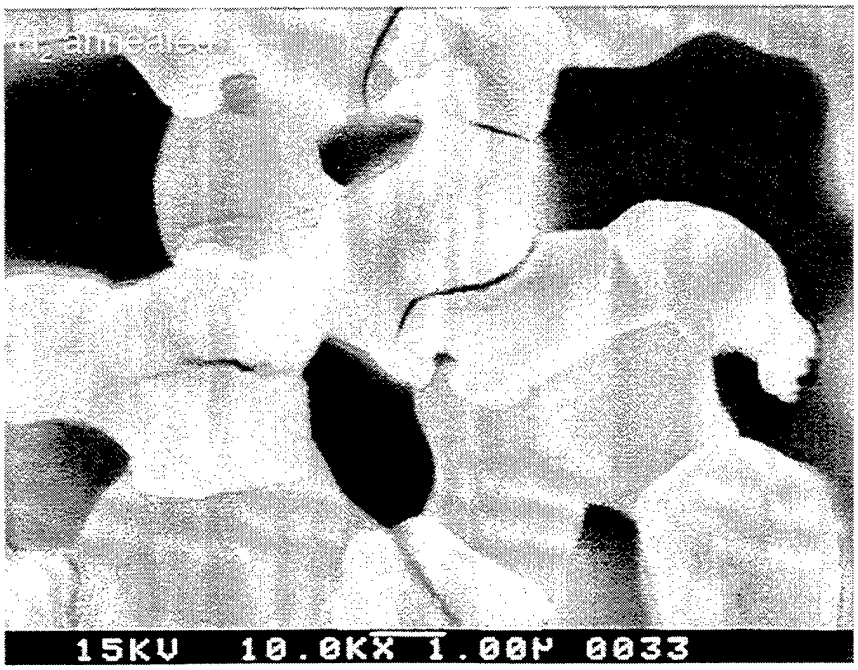

Figures 2.3. SEM images of Mo-SiO_2 FGMs

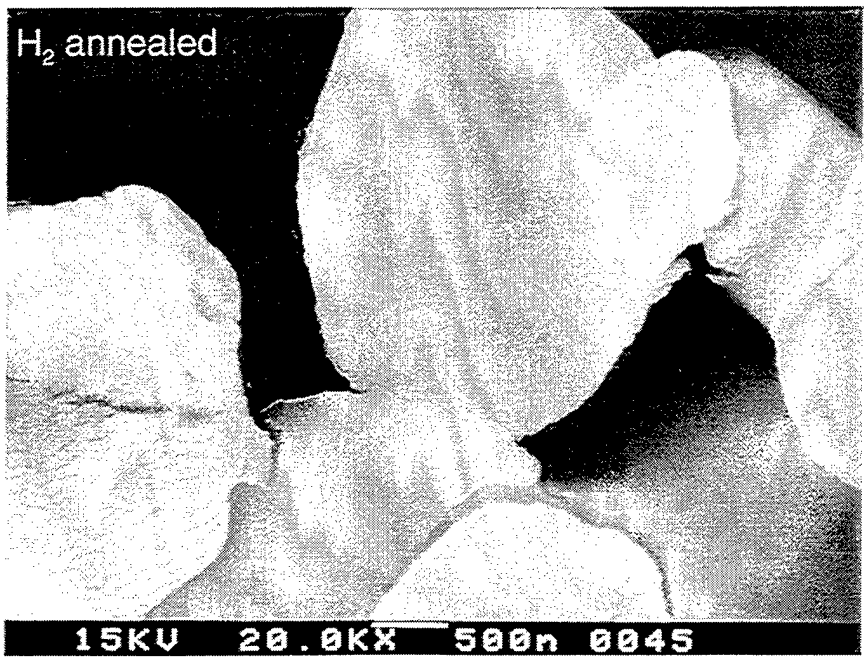

Figures 2.4. SEM images of Mo-SiO_2 FGMs

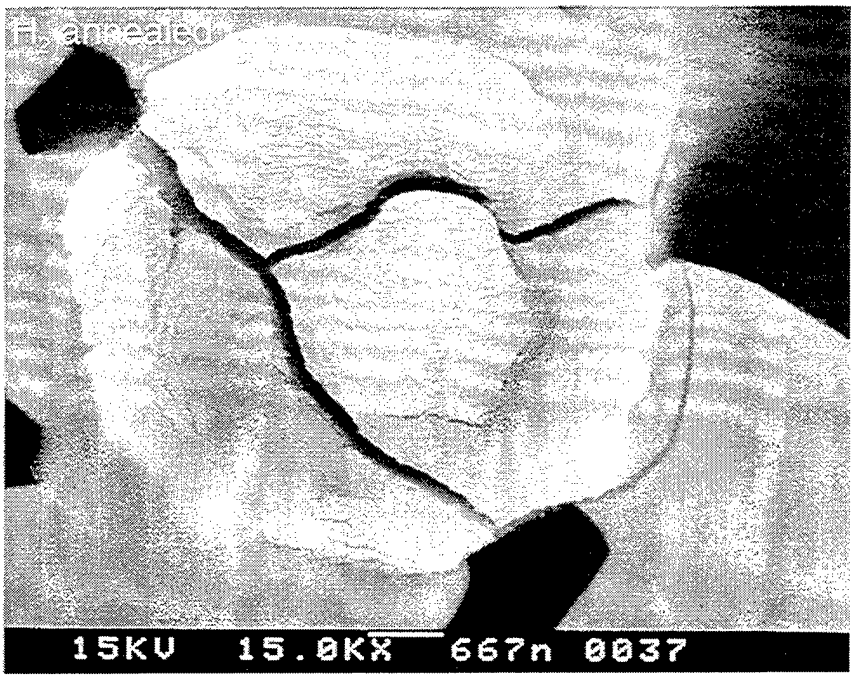

Figures 2.5. SEM images of Mo-SiO_2 FGMs

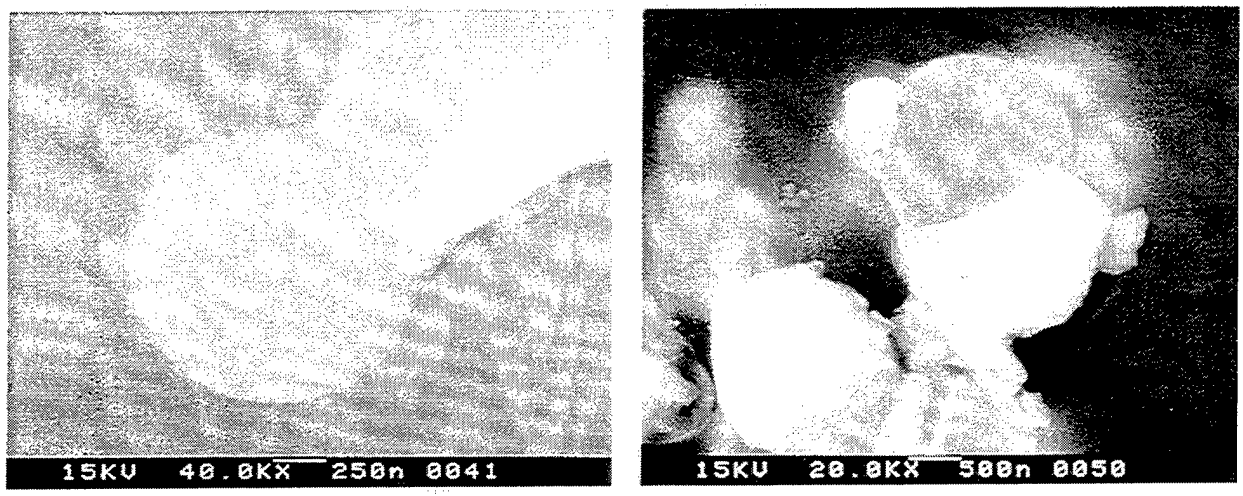

Fig. 2.6. SEM micrographs of specimen processed at TOTO after 1 min etching in 5% HF.

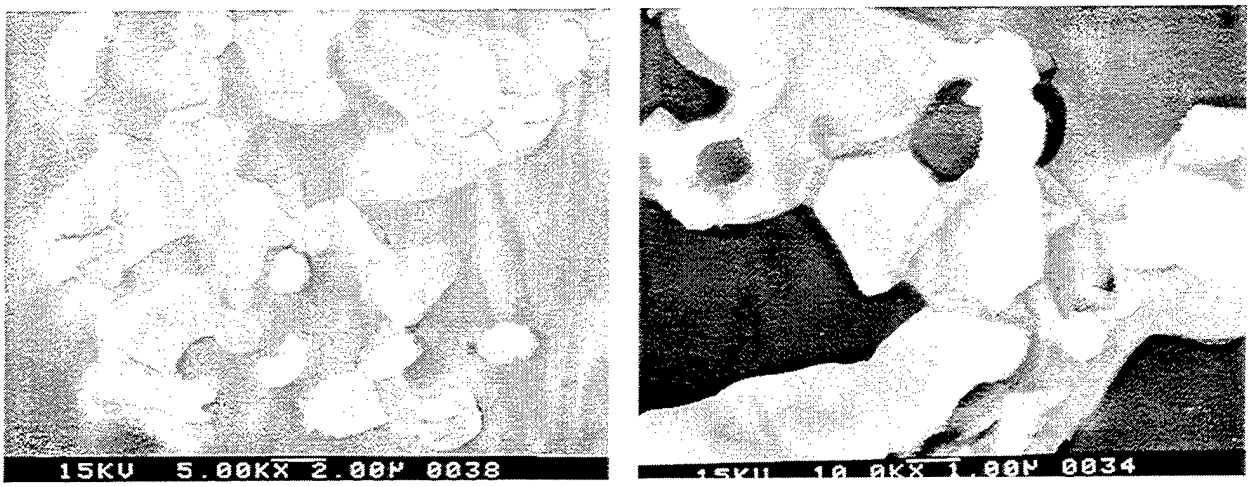

Fig. 2.7. SEM micrographs of specimen presintered at TOTO, H_2 fired for 2 h at 600°C at LBNL and finally sintered at 1740°C for 5 min. The cross-section was etched 1 min in 5% HF.

3. FGM Properties

3.1. Electrical properties

In order to perform resistivity measurements on Mo-SiO_2 composites, slices (~ 1 mm thick) where cut perpendicular to the gradient from FGM samples provided by TOTO. Resistivity measurements on each slice were performed using the 4-point d.c. method with currents between 0-500 mA, using silver paint contacts and pure copper wiring (Fig. 3.1.1). Mo content in each slice was determined by EDS analysis.

Figure 3.1.2 shows the resistivity vs. Mo content for slices cut from samples 662 (sintered in TOTO) and 498 (sintered in LBL after H_2 annealing). The resistivity of a Mo-ceramic composite can be modeled using the General Effective Media Equations, McLachlan, (1990) as:

$$\rho_c = \rho_{Mo}(1-\frac{1-f_{Mo}}{1-f_c})^{-t} \qquad [1]$$

where ρ_c is the resistivity of the composite, f_{Mo} the volume fraction of the composite, f_c the critical volume fraction needed for conductivity (for Mo contents lower than f_c the slice is insulating) and t is an exponent that is fitted from the experimental data and depends on the composite microstructure.

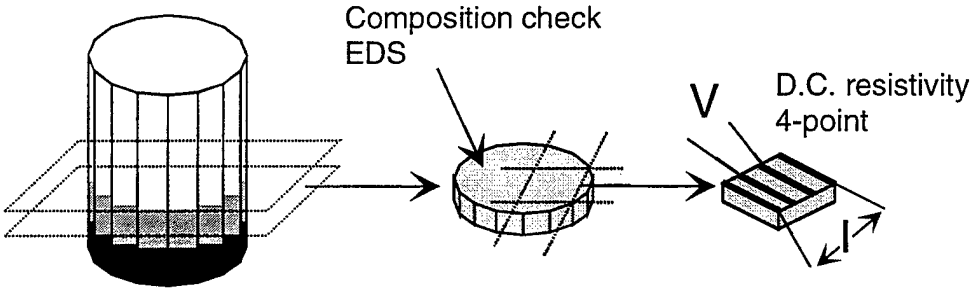

Fig. 3.1.1. Sample preparation for resistivity measurements. Slices ~ 1 mm thick are cut perpendicular to the gradient, the composition of the slice is analyzed by EDS. Samples ~1x10x5 mm were cut form each slice and resistivity measured by the d.c. four probe method with silver paint contacts.

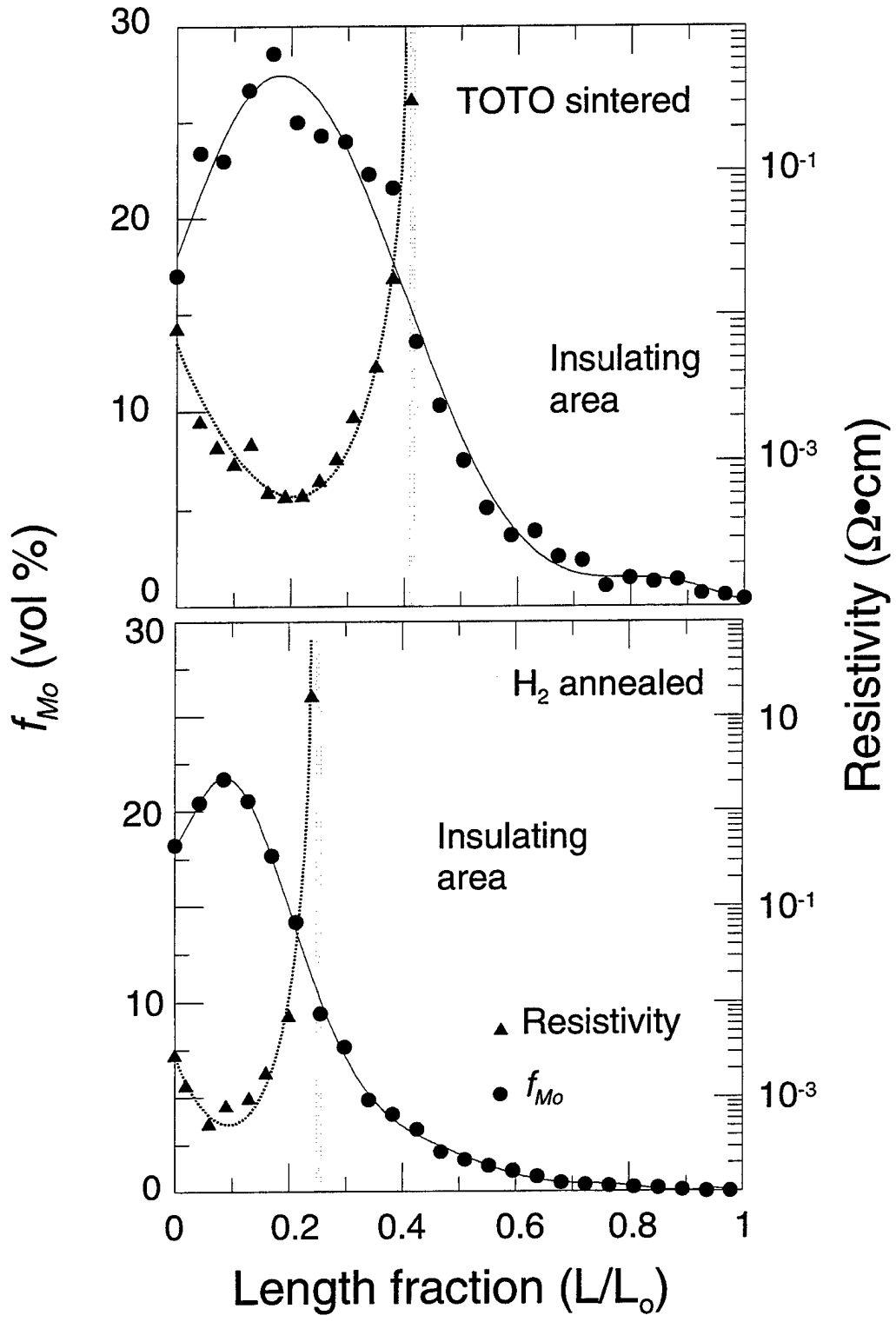

Fig. 3.1.2. Resistivity vs. composition for samples cut from a TOTO sintered FGM and for H_2 annealed one.

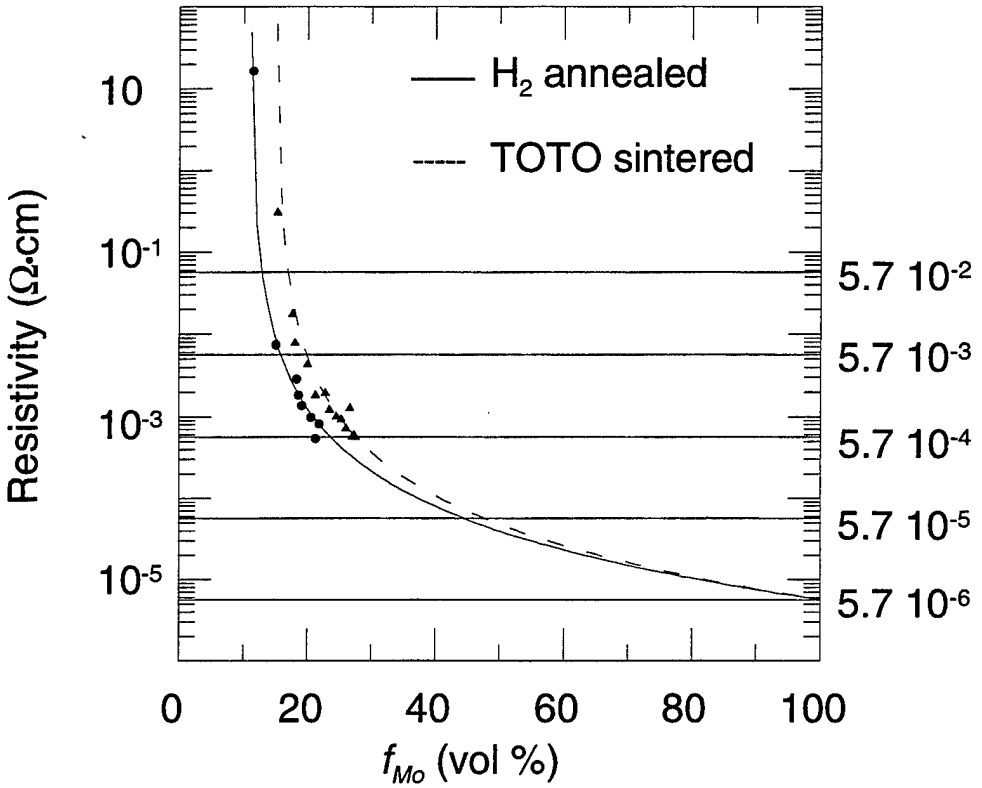

Fig. 3.1.3. Fitting of the resistivity results showed in Fig. 8 to the General Effective Media Equation, Eq. [2]. For the H_2 annealed sample t=2.4 and f_c=11 vol % and for TOTO sintered FGM t=2.35 and f_c=15 vol.%. For comparison, multiples of the Mo resistivity at room temperature (5.7 10^{-6} Ωcm) are also shown.

Fitting of the resistivity data with the General Effective Media Equation for samples 662 and 498 is shown in Fig. 3.1.3. The critical Mo volume fraction (f_c) is similar for both (15% for TOTO sintered samples and 11% for H_2 annealed specimen), the expected f_c for a random distribution of conductive and non-conductive spheres of same size is 16% which is slightly larger than measured. This can be due to the effect of particle size distribution. Possible alternatives to decrease the critical fraction of Mo needed for the conductivity (f_c) include the development of microstructures in which the conductive particles are not packed at random (e.g. have arrays of conductive particles in the form of strings) or to use Mo particles with more elongated shapes (for example, fibers).

The value of t in Eq. [1] is similar for both samples (2.4 for the hydrogen annealed sample and 2.35 for TOTO sintered). As long as the Mo particle size distribution and processing conditions are kept constant, the General Effective Media Equation with t~2.4 and f_c~11/15 can be used to predict the resistivity of Mo-SiO_2 FGM's prepared by TOTO.

For the studied FGMs the maximum Mo contents varies between 22 and 27 vol.%. As can be seen in Fig. 3.1.3, for these compositions, small changes in the fraction of conductive particles introduce large changes in resistivity (e.g. ~10% decrease in volume fraction increases resistivity one order of magnitude). This could be a source of

reliability problems. On the other hand, the conductive fraction of the sintered FGM (Fig. 3.1.4) depends on f_c, the maximum Mo content and the gradient. The samples measured have a similar gradient but a change of 6 % in the maximum Mo content has caused a decrease of 10% in the conductive fraction (equivalent to a length of ~2-3 mm). This is due to both the relatively sharp gradient and the magnitude of the Mo content which is in the critical region. In order to avoid these problems it will be necessary to increase the maximum Mo content in the FGM or to decrease the critical volume fraction f_c, and fabricate "smoother" gradients.

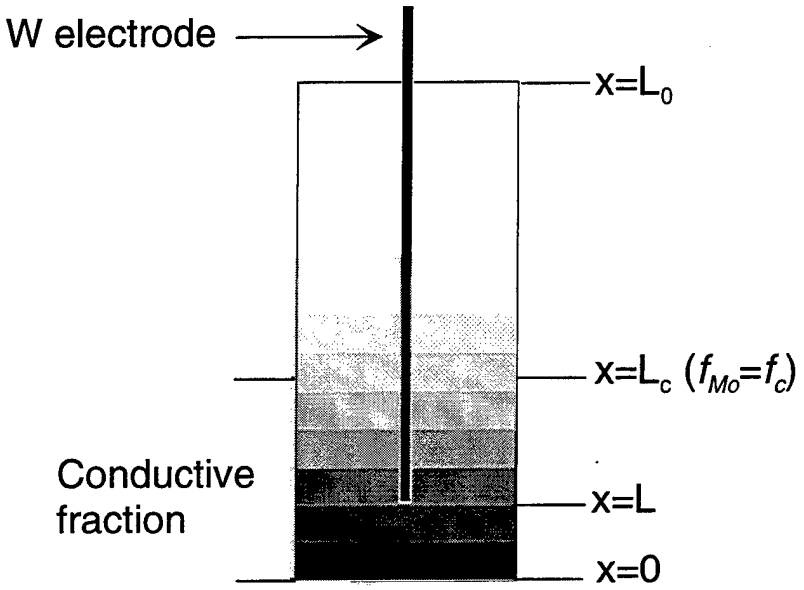

Fig. 3.1.4. Geometry of electrode connection. Total resistance of the connection will be that of the FGM from x=0 to x=L plus the resistance of the contact between the electrode and the FGM.

With the availability of the model, it is now possible to calculate the electrical resistance of the FGM between the contact and the electrode, corresponding to the resistance from x=0 to x=L as shown in Fig. 3.1.4. The FGM specimen can be modeled as a series of slices with resistance R_1, R_2,....R_n, the resistance of the slice i will be:

$$R_i = \rho_i \frac{l}{\pi r^2} \qquad [2]$$

where ρ_I is the resistivity of the slice i, that will depend on its Mo content as calculated using Eq. [1], l is the length of the slice and r is the radius of the FGM assuming it has a cylindrical shape. The total resistance of the FGM sample will be:

$$R = \sum_{n=1}^{n} R_n = \frac{1}{\pi r^2} \sum_{n=1}^{n} \rho_n l \qquad [3]$$

and in integral form:

$$R = \frac{1}{\pi r^2}\int_0^L \rho(x)dx = \frac{1}{\pi r^2}\int_0^L \rho_{Mo}\left(1-\frac{1-f_{Mo}(x)}{1-f_c}\right)^{-t}dx \qquad [4]$$

where the resistivity as a function of the position, x, has been written in terms of equation [1]. Now if we know the gradient we can express the Mo content as a function of x (f_{Mo}(x)) and integrate analytically or numerically Eq. [4] to obtain the total resistance of a fraction of the FGM. Equation [4] is only valid for the conductive part of the material, where $f_{Mo}>f_c$.

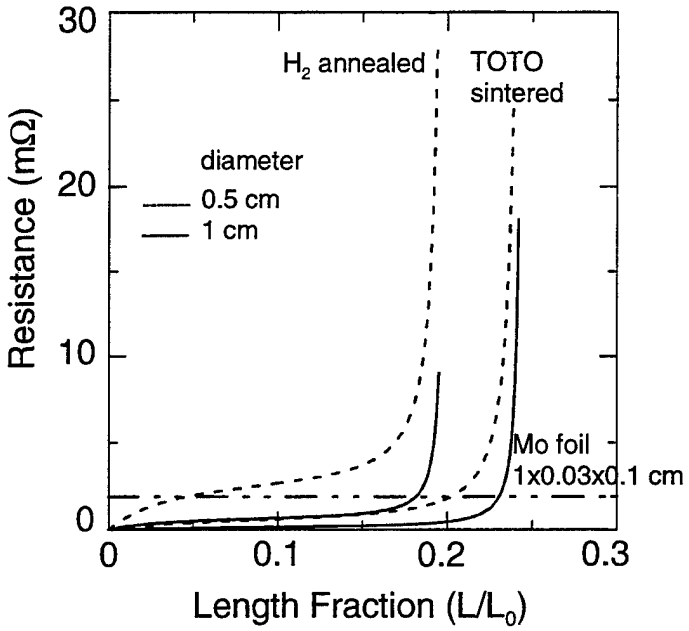

Fig. 3.1.5.- Total resistance of a portion of FGM depending on its length (x=0 correspond to the Mo rich end). The calculation has been performed using Eq. [4], and the length of the portion expressed as a fraction of the total length. The gradients utilized for the calculation correspond to samples 662 and 498. The resistance has been calculated for two FGM diameters 0.5 and 1 cm. For comparison, the resistance of a Mo foil (1x0.03x0.1 cm) is also plotted (horizontal line). Eq. [4] can be utilized to calculate the maximum length L to which the electrode hole can be drilled in order to have electrical resistance lower than some determined value.

Figure 3.1.5 shows the calculated resistance of the FGM as a function of the fraction of total length (L/L_0) for the TOTO sintered sample and the hydrogen annealed one (~1 cm diameter). For comparison the resistance of a 1x0.01x0.3cm Mo foil similar to the ones used for the contact in conventional HED lamps is also plotted. It can be observed that for lengths almost up to the critical length, where $f(x)=f_c$, the FGM present lower resistance than the Mo foil. The final resistance of the electrode connection will be composed of two parts, one is the resistance of the FGM, calculated in Eq. [4] and the other is the contact resistance between the electrode and the FGM.

Finally I-V measurements have been performed for different slices. For Mo rich composites (f_{Mo}~0.2 vol %) linear behavior has been observed with currents up to 0.6 A.

For Mo contents close to f_c the behavior is not linear probably due to the heating from the high current densities in the low conductivity areas.

3.2. Hardness and Toughness

It is intended to measure the fracture resistance for cracks growing both parallel and perpendicular to the gradient. This requires using several different test geometries as described previously. Preliminary data have been generated using indentation techniques which are less accurate but quicker.

A set of hardness tests were conducted using Vickers indentation on samples of varying Mo content. The samples were a series of cross-sectional samples cut normal to the FGM axis and polished. The loads were adjusted in order to obtain indentations having well defined radial cracks which could be used to compute the fracture toughness, but without lateral cracking or spalling. (Small loads give indentations with no cracks and excessive loads cause spalling.) This resulted in the use of loads varying from 8 to 50 N, with higher loads being required for the higher Mo contents. For the measured indentation size and crack size both the hardness and fracture toughness were calculated. The toughness was calculated from the relation given by Anstis et al (1981) as:

$$K_{IC} = 0.016(E/H)^{1/2}P/C^{3/2} \qquad (5)$$

where E is the Young's modulus; H, the hardness; P, the indentation load; and C, the measured crack length. The Mo compositions for each location along the FGM axis were measured by EDS as described in section 3 (in fact these were the same samples as used for the conductivity measurements). The elastic moduli were those calculated based on the Mo concentration, given in the semi-annual report, Tomsia et al (1996).

The hardness varied weakly with Mo content, up to the maximum in the sample of 27 vol %, as is shown in Fig. 3.2.1, and was little different for the standard samples and the H_2 fired samples. These are reasonable, although with a weaker than expected dependence on Mo content, given reported values of 7 GPa for fused SiO_2 Shand (1958) and of 2 GPa for annealed Mo, Shreir (1976).

The apparent toughness values showed a complex dependence on the Mo content, but the tests with low Mo contents are suspect as the cracks are too small. Fig. 3.2.2 shows only the results of tests with long cracks (C/a > 2, a = diagonal of the indent). Also shown are the literature values of $K_{IC} = 0.75$ MPa-$m^{1/2}$ for fused SiO_2, Lawn (1994). The experimental values indicate that the toughness increases with Mo content to a value of $K_{IC} = 2$ MPa-$m^{1/2}$ for a Mo fraction of 27%. Optical micrographs and SEM images of the indentation and of an associated crack are shown in Fig. 3.2.3. The moderate increase in toughness with Mo content is expected since Mo itself has K_{IC} of 5-10 MPa-$m^{1/2}$ for annealed or sintered material. The toughening mechanisms involves some deflection of cracks and bridging of metallic ligaments across the crack flanks as can be seen in the SEM images.

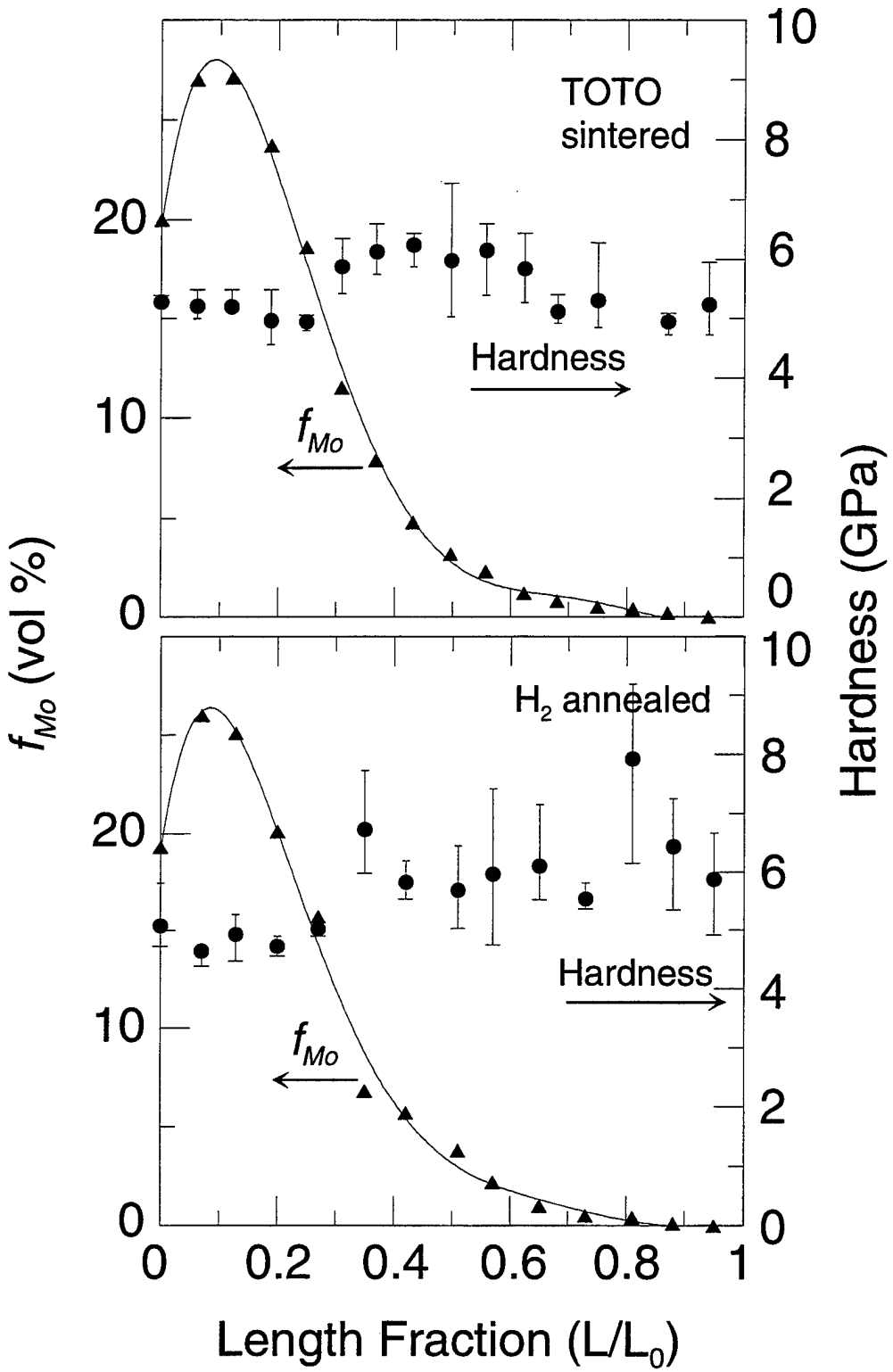

Fig. 3.2.1. Plots of Vicker's hardness and of Mo content versus position along length for Mo-SiO_2 FGM's prepared with the standard firing at TOTO and LBL with a H_2 pre-fire to remove excess oxygen.

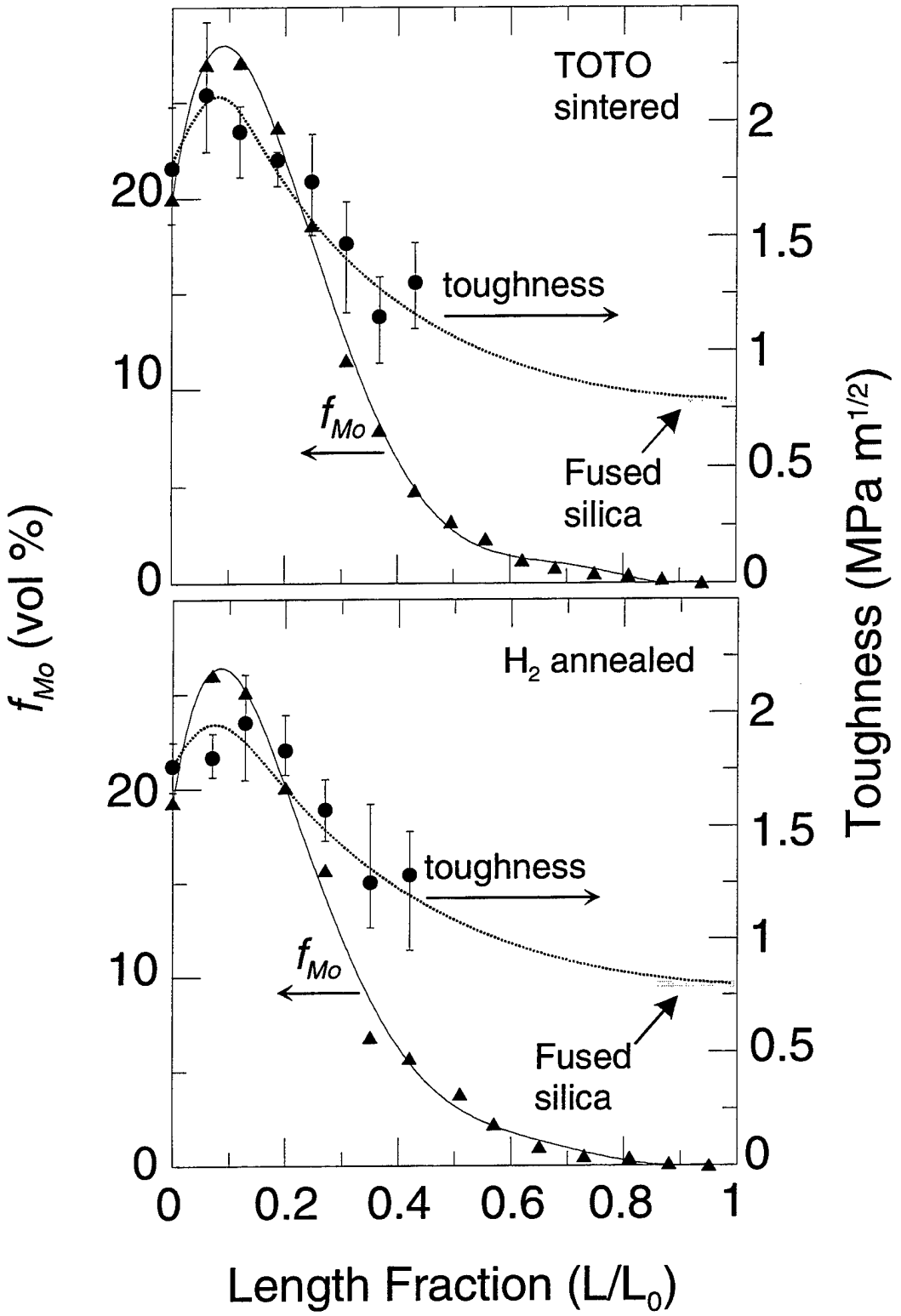

Fig. 3.2.2. Plots of fracture toughness, K_{IC}, and of Mo content versus position along length for Mo-SiO_2 FGM's prepared with the standard firing at TOTO and LBL with a H_2 pre-fire to remove excess oxygen.

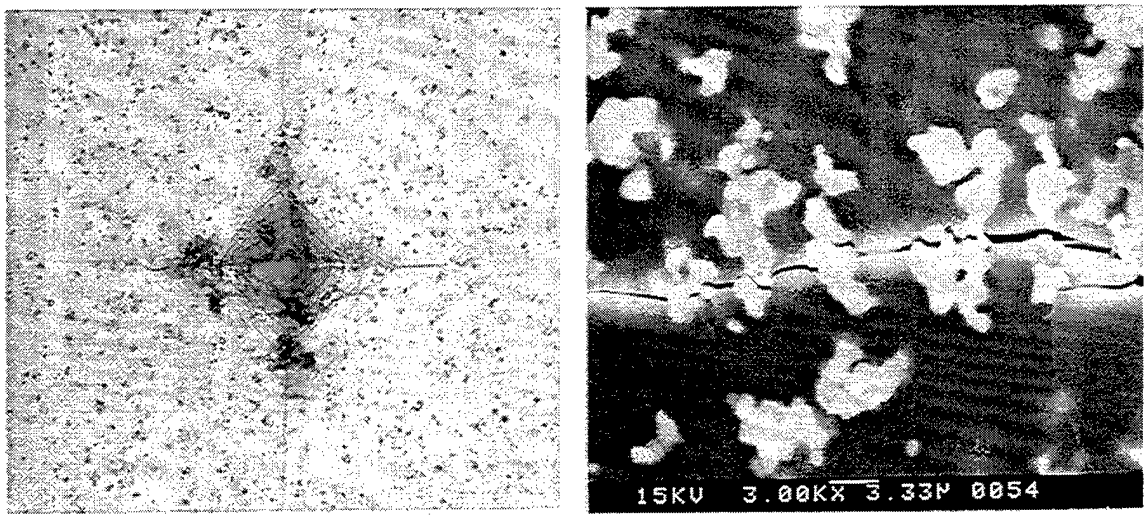

Fig. 3.2.3. Micrographs showing Vickers indentation (a) and a higher magnification image of a crack (b). The latter shows that the cracks sometimes are deflected around the metal particles, and sometimes crack through the sintered clusters. In some cases the clusters do not immediately crack, leading to a ligament which bridges the crack and increases the toughness.

The toughnesses deduced from these indentation methods can be inaccurate or incomplete. With high SiO_2 glasses some local atomic densification occurs under the indentor which results in smaller residual stresses than commonly occur and are assumed to occur for Eq (5) to be valid, Lawn (1994). This results in difficulty obtaining well developed cracks and smaller than expected cracks, especially for the low Mo contents. Although the tests can be used with the higher Mo content, in these cases some dependence upon crack length is expected which cannot be readily determined using the above method.

3.3. Bending test and thermal cycling.

Preliminary strength tests have been performed by four point bend tests of bars cut longitudinally from FGM's fired in TOTO and others H_2 annealed at LBNL (see Fig. 3.1). The bars were 3x3x20 mm. The tensile face was polished with diamond of 1 μm particle size, the edges beveled and prior to the test, ceramic extensions were glued to the bars. The samples are centered in the four point bend fixture such that the gradient zone is the one tested. Table I summarizes the strength results.

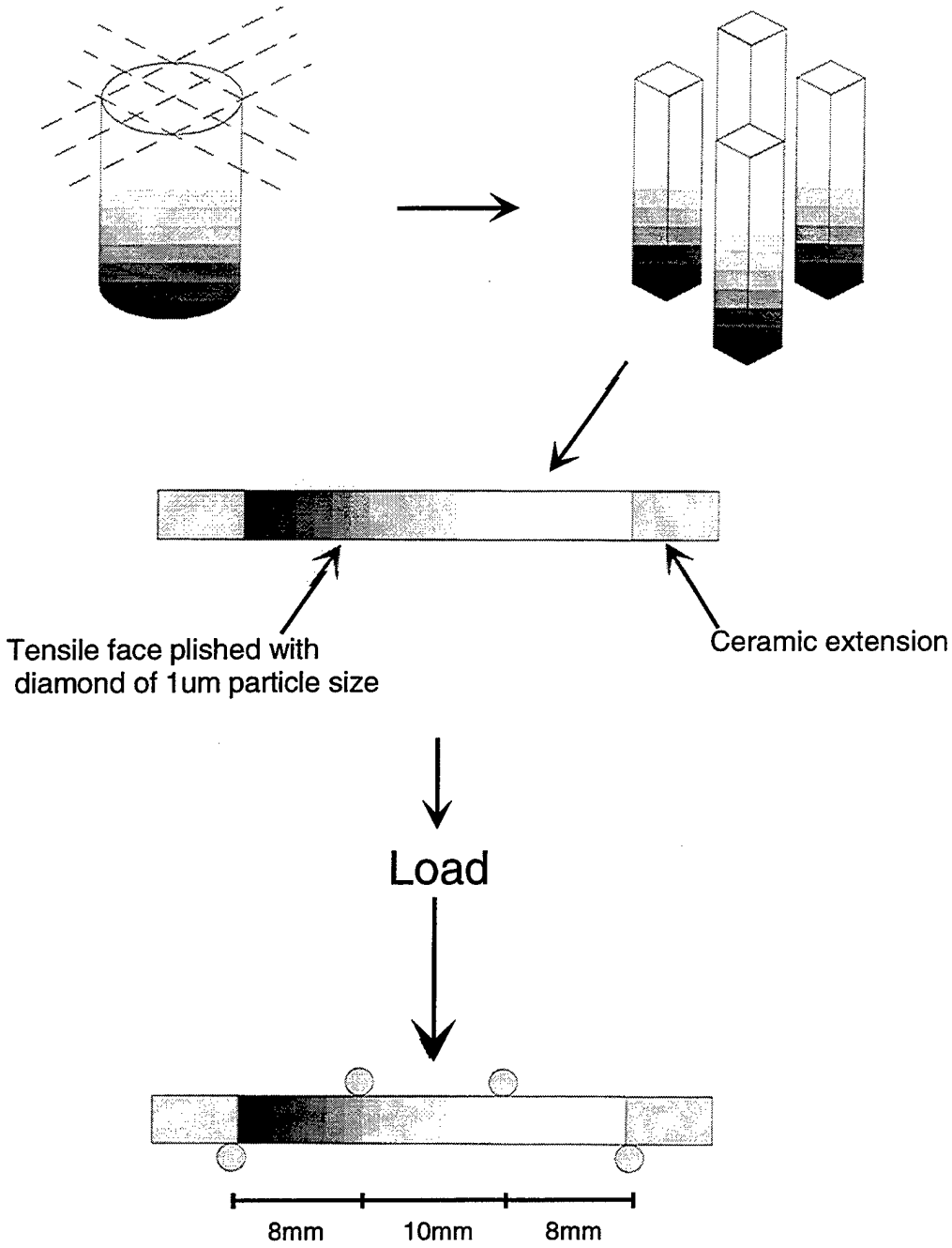

Figure 3.1.- Sample preparation for the 4-point bend test and test configuration.

Table I. Strength results of four point bend test (MPa)

	TOTO fired	H_2 annealed	After 100 cycles
	101.5	90.1	84.4
	106.2	99.4	99.3
	100.8	97.1	103.3
Strength	89.6	84.3	114.5
(MPa)	91.9	98.4	106
	80	119.2	
	102.3		
	69.1		
average	92.7±12.8	98.1±11.9	101.5±11.1

In order to study the effect of thermal cycling TOTO sintered FGM's (a complete FGM and a 6x3x20 mm plate longitudinally cut) were cycled between 250 and 1000 °C in vacuum. After cycling four point bend tests were performed in bars prepared in the way previously described (see Table I).

The strength test did not show significant differences between TOTO fired and H_2 annealed FGM's and no significant decrease in strength after 100 thermal cycles was observed.

3.4. Thermal expansion

Thermal expansion measurements have been performed on slices (0.8x8x7 mm) cut from TOTO fired and H_2 annealed FGM's in the direction perpendicular to the gradient (see Fig. 3.4.1). The composition of each slice was measured by EDX analysis on both sides of the piece. The thermal expansion was measured by dilatometry in the direction perpendicular to the gradient. The dilatometries were performed in flowing Ar using a ORTON dilatometer with an alumina holder and push rod, at temperatures between 25-600 °C and heating rate of 3 °C/min. In order to reduce the experimental error, Al_2O_3, mullite and fused silica were used as standards to calibrate the dilatometer.

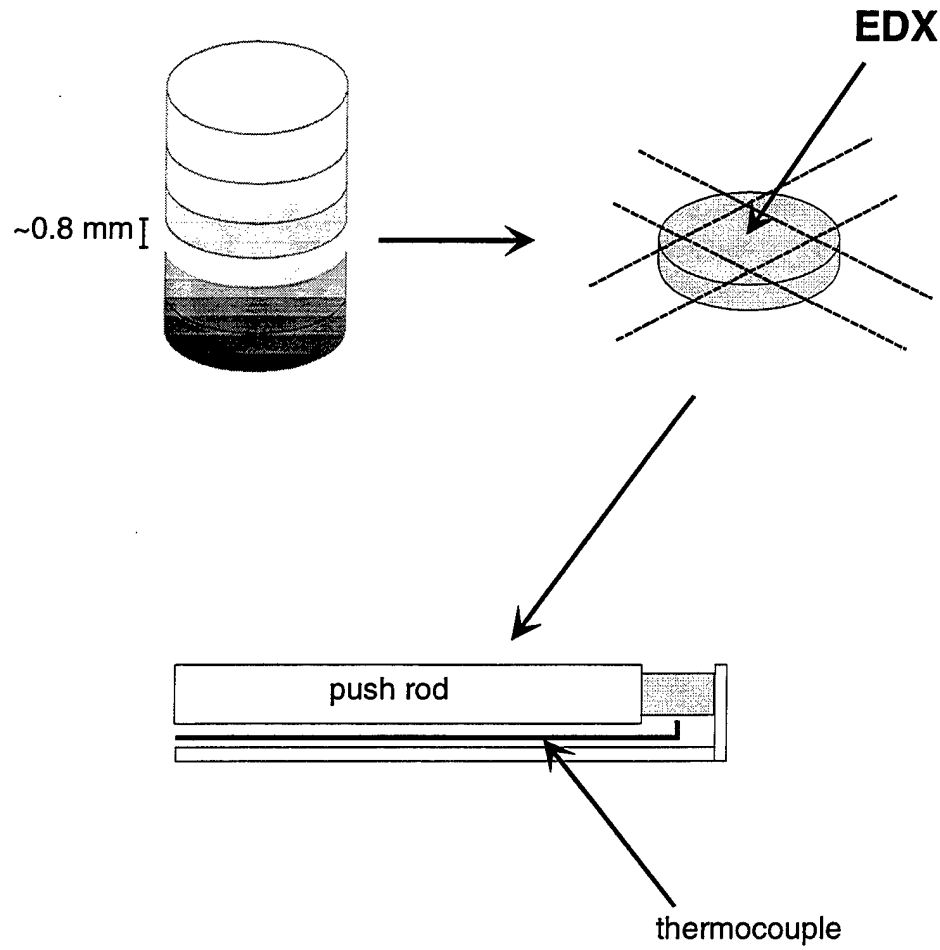

Figure 3.4.1.- Sample preparation for dilatometry

Figure 3.4.2 shows the thermal expansion of each slice vs Mo content and its corresponding position in the FGM. As expected, the thermal expansion of the sample increases with increasing Mo content (α_{Mo}= 5.1 10^{-6} °C^{-1} and α_{SiO2}= 0.55 10^{-6} °C^{-1}). The measured α values are compared with the predictions of Turner and Kernel models (Fig. 3.4.3). The Turner model assumes that no cracks develop, that the contraction of each grain is the same as the overall and that all the microstresses are pure hydrostatic tension and compression (interfacial shear is negligible). The final expression for the thermal expansion of the composite is then:

$$\alpha = \frac{\alpha_1 V_1 K_1 + \alpha_2 V_2 K_2 + ... + \alpha_n V_n K_n}{\alpha_1 V_1 + \alpha_2 V_2 + ... + \alpha_n V_n} \qquad [1]$$

where α_n is the thermal expansion of the component n, V_n its volume fraction and K_n is the bulk modulus:

$$K_n = \frac{E_n}{3(1-2\mu)} \qquad [2]$$

The Kerner model takes into account the shear effects at the grain and phase boundaries, and for a composite with two components gives an expression:

$$\alpha = \alpha_1 + V_2(\alpha_2 - \alpha_1)\frac{K_1(3K_2 - G_1)^2 + (K_2 - K_1)(16G_1^2 + 12G_1K_2)}{(4G_1 + 3K_2)[4V_2G_1(K_2 - K_1) + 3K_1K_2 + 4G_1K_1]} \qquad [3]$$

where G_n is the shear modulus of the phase n.

The experimental results for the Mo-SiO_2 composites lies between the two models. An approximate empirical relationship for samples taken from TOTO FGM's is:

$$\alpha(°C^{-1}) = 6.721\ 10^{-7} + 1.0003\ 10^{-7} f_{Mo} - 7.83605\ 10^{-10} f_{Mo}^2 + 2.22997\ 10^{-12} f_{Mo}^3 \qquad [4]$$

where f_{Mo} is the volume fraction of molybdenum in the composite.

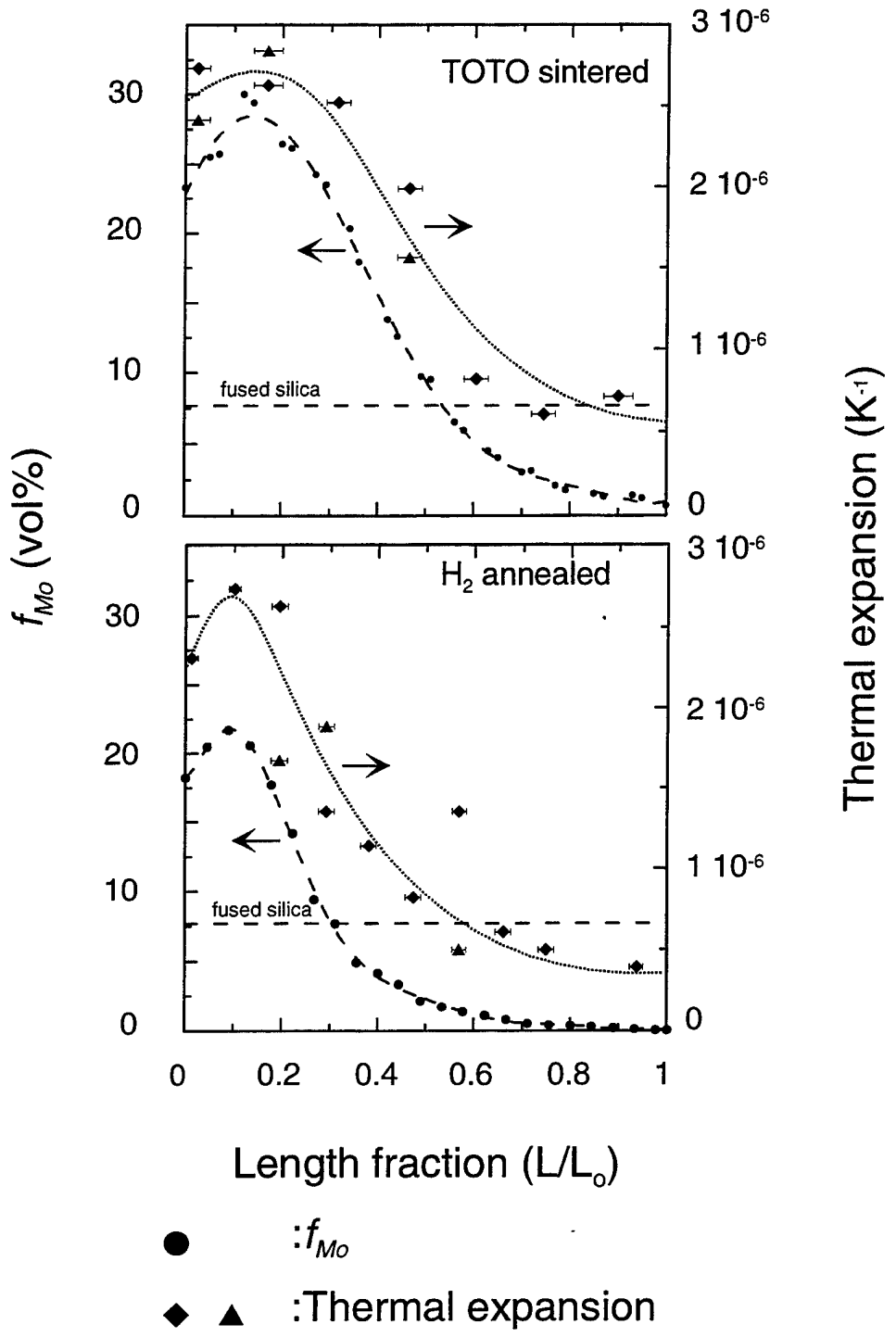

Figure 3.4.2. Measured thermal expansion coefficient of slices cut from TOTO fired and H_2 annealed FGM's. The x axis indicates the position in the FGM where the slice was cut. Its composition (discontinuous line) can be read on the left axis and its thermal expansion coefficient (two measurements have been performed on each piece) on the right.

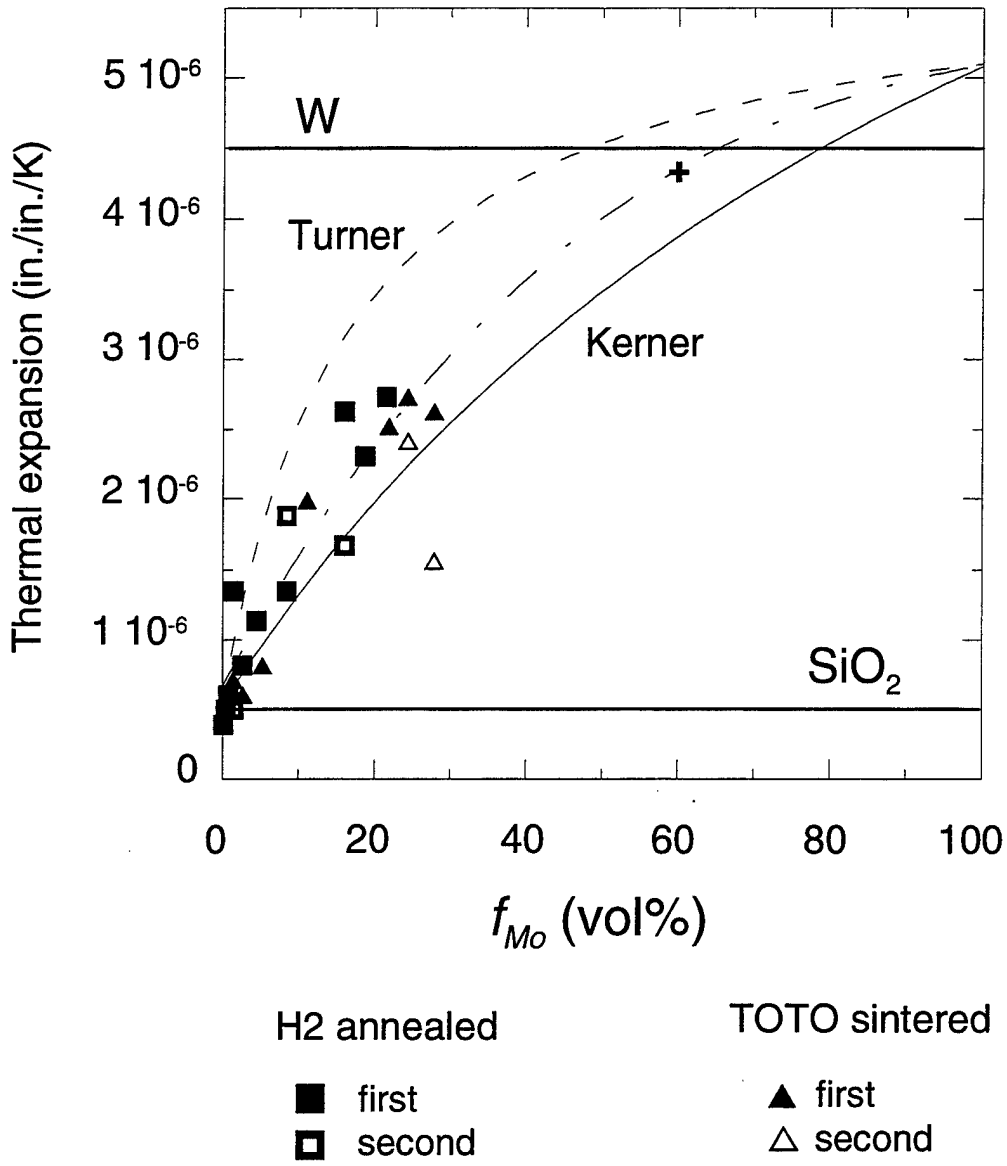

Figure 3.4.3. Thermal expansion coefficients of the Mo-SiO_2 samples vs. their Mo content. Two measurements have been performed in each sample. The predictions from Kerner and Turner models are also plotted. The middle line corresponds to an empirical fitting of the results. The horizontal lines are the thermal expansion of the electrode material (W) and of the lamp bulb (fused silica).

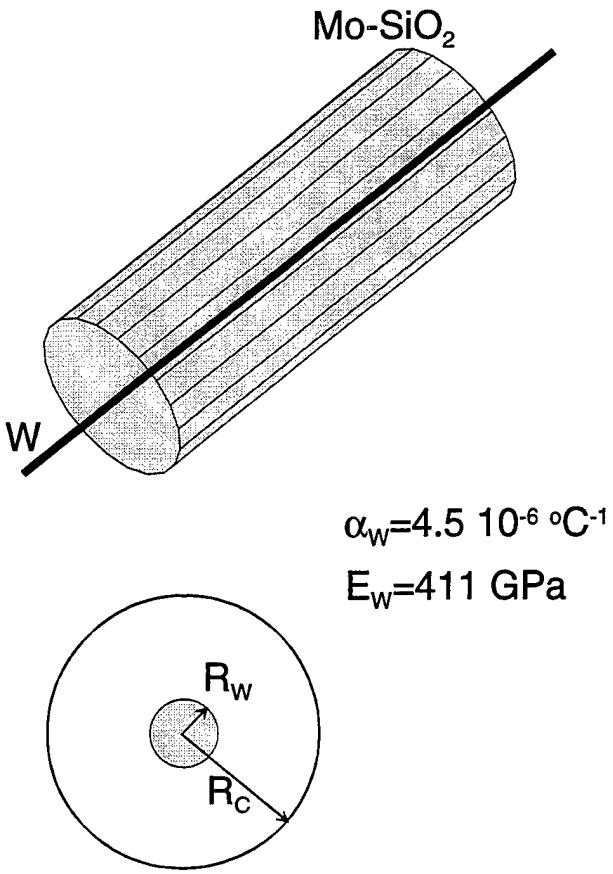

Figure 3.4.4.- Configuration of the bead seal. Glass is sealed over a metal rod in a concentric cylinder geometry. The calculations performed here are for an infinitely long two materials seal.

In the lamp configuration a tungsten electrode is placed across the FGM and the complete piece is sealed to the fused silica lamp end. In order to estimate the interfacial tensions between the FGM and the W electrode, the measured thermal expansions for the Mo-SiO_2 composites and their calculated Young modulus (see first report) have been used to determine the stresses in a bead seal between W and a Mo-SiO_2 composite. The stresses have been calculated supposing an infinitely long two material seal (the composite around the W wire) in a concentric cylindrical geometry (see Stresses in Glass-to-Metal Seals, Arun K. Varshneya, Treatise on Materials Science and Technology, Vol 22). The thermal expansion coefficient and Young Modulus for tungsten used in this calculations are: $\alpha_W=4.5\ 10^{-6}\ °C^{-1}$ and $E_W=411$ GPa.

From this preliminary calculation (Fig 3.4.5) it seems that for the maximum Mo contents measured in TOTO FGM's radial and hoop stresses of ~ 200 MPa are present at the W/composite interface. This suggests that to ensure a better sealing between the FGM and the electrode higher molybdenum concentrations are needed at the Mo rich end. It can also be seen that the radial and hoop stresses do not depend very much on the radius of the W electrode (Fig. 3.4.6).

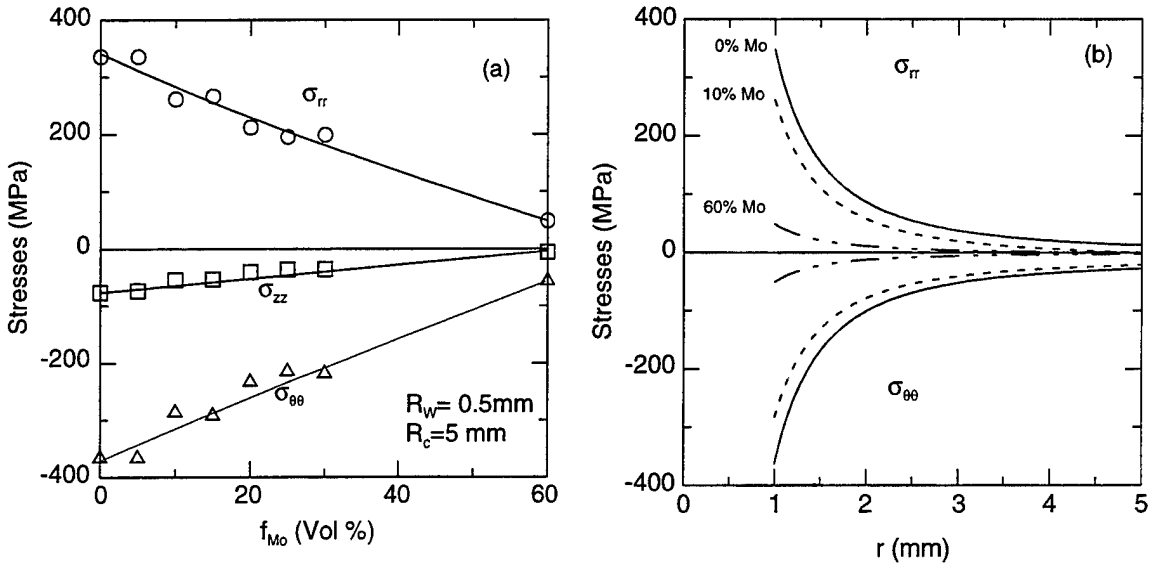

Figure 3.4.5.- Stresses in a bead seal between W and Mo-SiO_2 composites after cooling from 1300 °C to room temperature..

(a) The stresses at the W/composite interface vs Mo content in the composite.

(b) Stress distribution in the composite depending on the distance from the center of the seal.

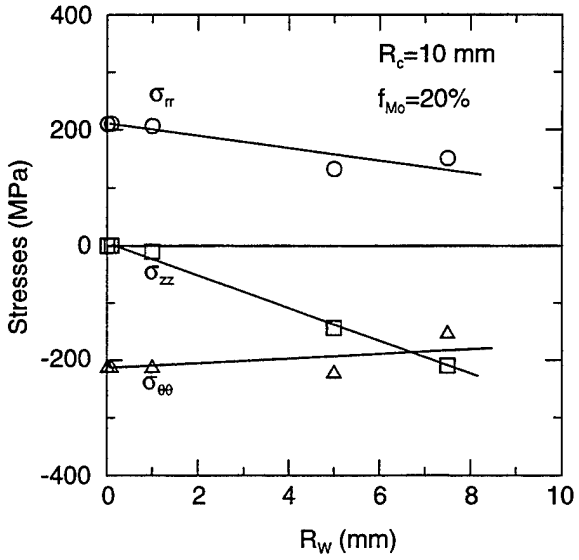

Figure 3.4.6.- Stress at the W/composite interface, after cooling from 1300 °C to room temperature, depending on the radius of the W rod (f_{Mo}=20%).

More accurate modeling is needed to calculate the final stresses in the complete electrode. It should take into account the presence of three layers (W, FGM and fused silica) and also the effect of the gradient in the FGM part.

4. TEM Analysis

TEM analysis has been conducted on samples from five different batches (#295, #486, #670, #784, #803), all of which had been processed at TOTO, without a H_2 prefire.

Following is preliminary analysis of sample #670, analyzing the Mo-rich end of sample. Although XRD did detect some Mo oxide in this sample (as well as others), Mo oxide grains were not found by TEM in this sample. Also the TEM suggested the Mo grain size is smaller than for previous samples (#295). TEM samples were prepared with ion milling. The silica etches faster, causing holes in sample where SiO_2 initially existed. The Mo etches very slowly, leaving very thick regions.

Fig. 4.1 is a low magnification image. Bright regions represent thick Mo grains, and black regions represent holes where the silica was prior to ion etching. Fig. 4.2a is a higher magnification image of a boxed area in Fig. 4.1. Brighter regions represent thick Mo grains. Gray regions represent thinner Mo grains. Many grains are smaller than 1 micron. (In sample #295 most grains were larger than 1-2 microns.). Fig. 4.2b is a diffraction pattern from a Mo grain, indicated by the round area in Fig. 4.2. Using electron diffraction on various grains, only crystalline Mo was observed. No patterns matched $MoSi_2$, MoO_2, nor crystalline SiO_2. Electron diffraction of silica regions showed only amorphous material.

Fig. 4.3 is another representative area, with bright regions being Mo grains, and some amorphous gray regions being silica and diffracting gray regions being thin Mo grains. EDS spectra 1 through 4 were acquired of areas (0.1 to 0.2 micron areas) in this region. The results showed that: spectrum 1 is from a "thin" appearing Mo grain ; spectrum 2 is from a "very thick" Mo grain; spectrum 3 is from a "medium thin" Mo grain; and spectrum 4 is from an amorphous silica region.

The O and Si peak heights track together, and this implies the Si and O detected in Spectra 1 and 3 is due to silica which overlaps the Mo grain. As the TEM sample is thinned by ion etching these overlapping areas will thin much faster than regions only having Mo. In thick regions which are only Mo grains, the O and Si signals are very low (presumably due to fluorescence artifacts of EDS analysis). No grains exhibited only Mo and O by EDS, nor did any grains exhibit uniform contributions of Mo, O and Si as indicated in sample #295.

In sample #295 grains of a second crystalline phase were analyzed and found to be similar to MoO_2, but nearly always exhibited some Si, Fig. 4.4. Based on subsequent analysis, it is concluded that the Si signal results from residual SiO_2, either not removed by ion etching, or sputtered onto the grain during ion thinning. Thus, the presence of MoO_2 is deemed to be consistent with x-ray and SEM/EDS evaluations. The more extensive x-ray and SEM studies which yield more representative statistics indicate these oxides are present in all batches received from TOTO. The experience indicates that the MoO_2 phase does not continuously coat the Mo particles but tends to be only partially

wetting between the Mo and glassy phase and. In addition, no evidence was found of oxide-rich films at the Mo-Mo grains boundaries which would diminish conductivity. Finally, the TEM images were also consistent with the SEM images and x-ray analysis indicating that there is no reaction between Mo and silica, as expected with proper control of $p(O_2)$.

The micrographs from a sample of #486, Fig. 4.5, again show the Mo and SiO_2 rich regions. The extensive agglomeration of the Mo particles is apparent. In addition, some very fine Mo-rich particles dispersed in the glassy phase are evident. It remains to be seen whether these precipitated on cooling or are cause by TEM sample preparation.

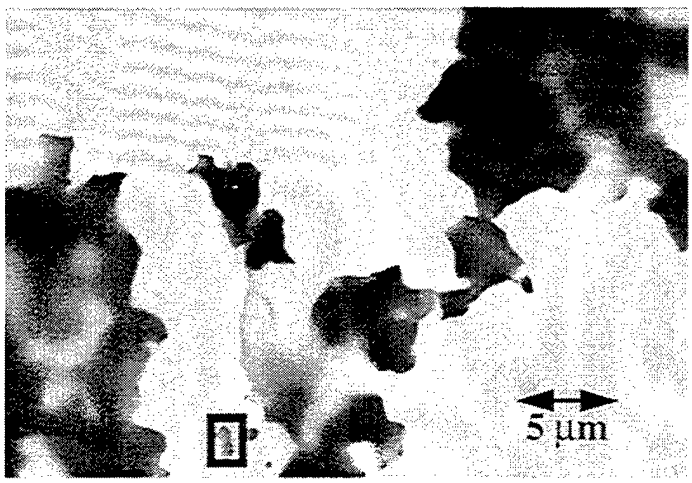

Fig. 4.1. Low magnification TEM image of sample #670 Mo/SiO_2 FGM.

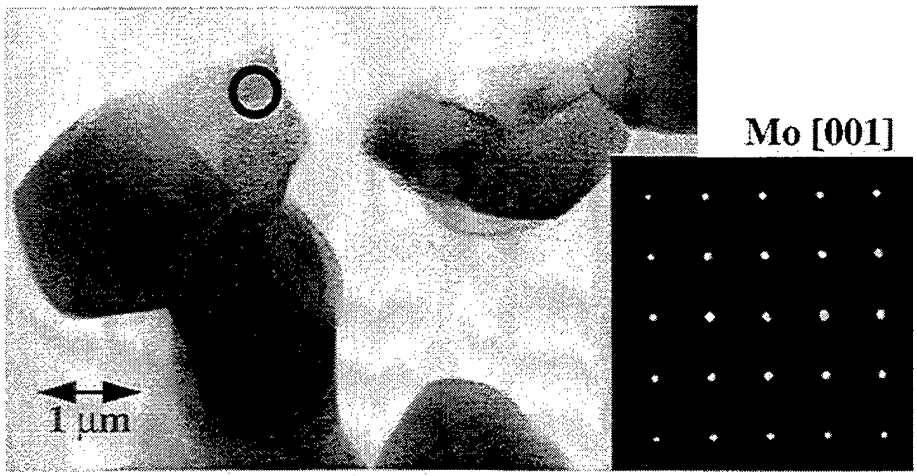

Fig. 4.2. Higher magnification TEM image of region noted by box in Fig. 4.1 (a) and SAD identifying the circled region as being Mo.

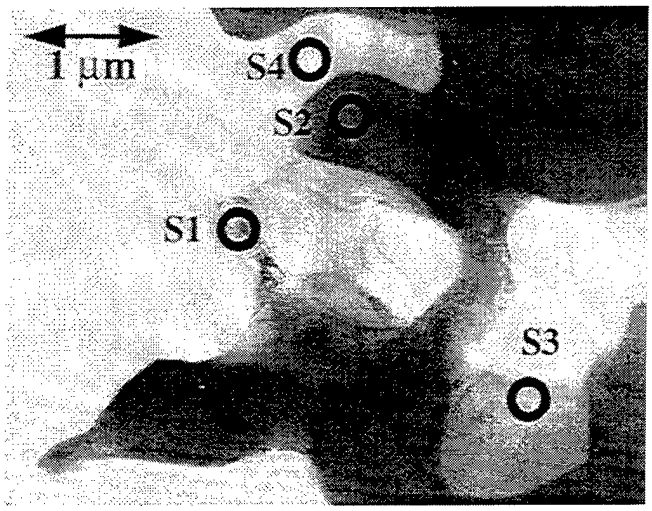

Fig. 4.3. Low magnification TEM image of sample #670 Mo/SiO_2 FGM. EDS spectra diffraction revealed regions S1, S2, and S3 to be Mo grains and S4 to be SiO_2 rich.

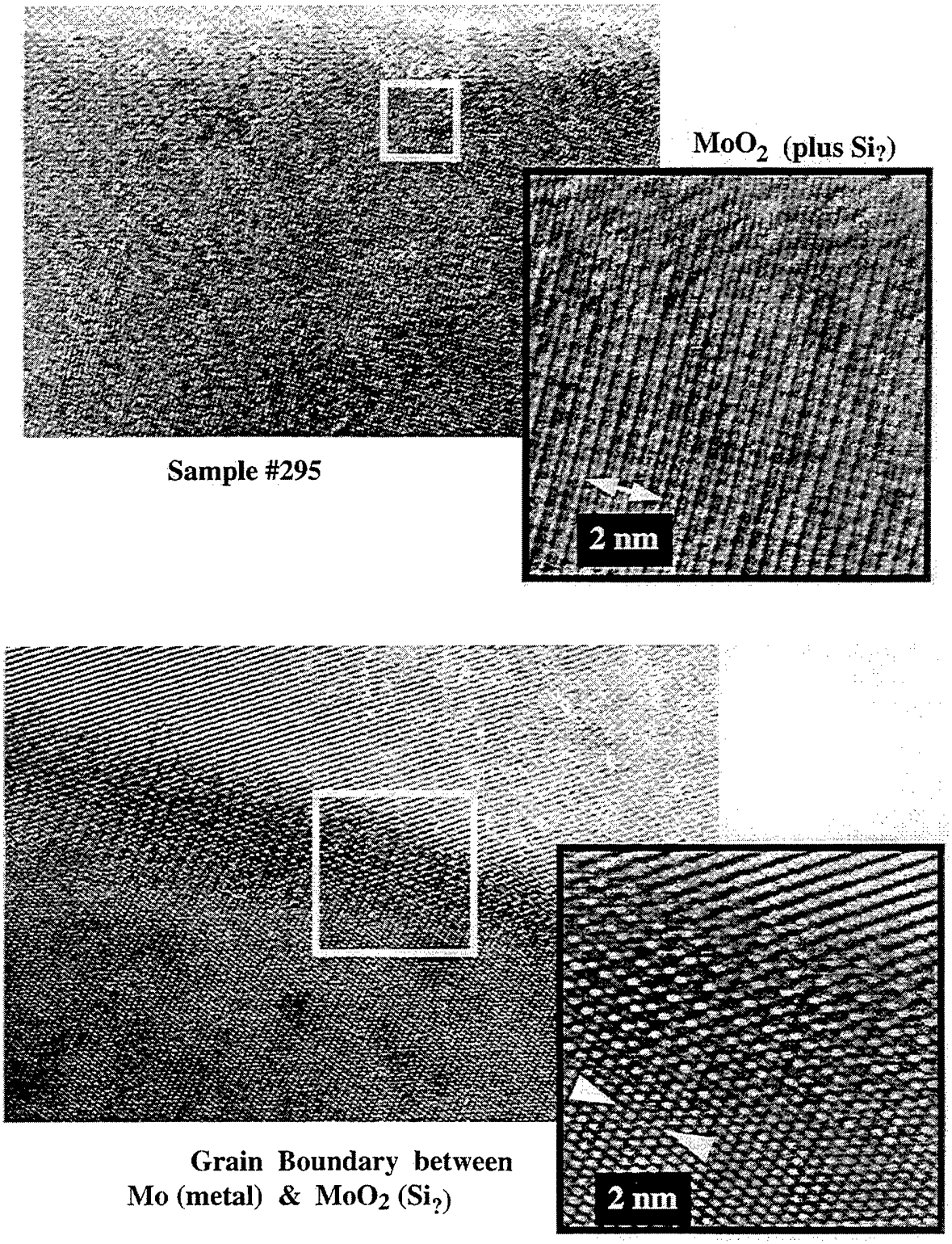

Fig. 4.4. TEM image showing MoO_2 grain next to a Mo grain (a), and a higher magnification image of the grain boundary between them (b) showing the absence of any other reaction product or intermediate phase.

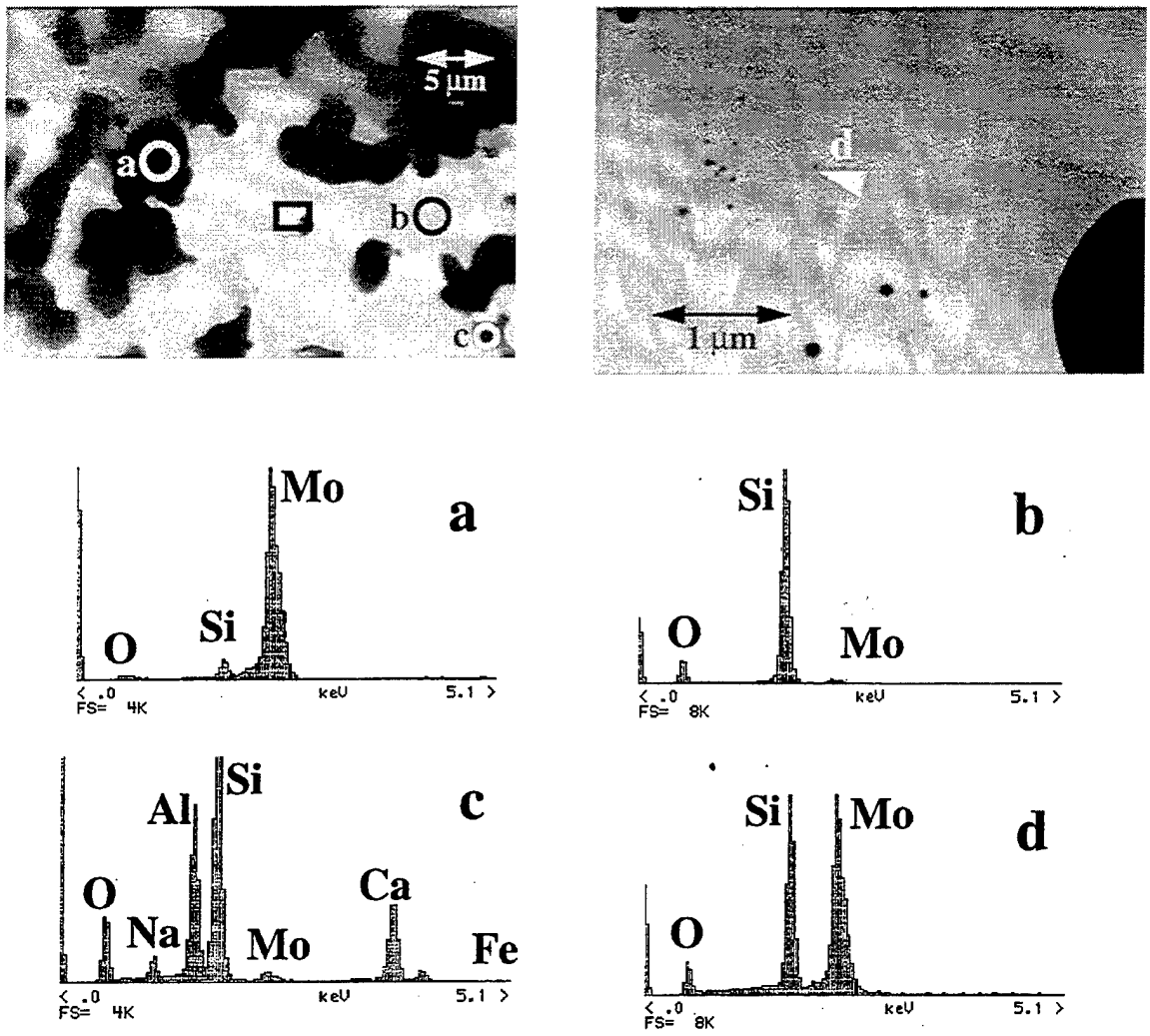

Fig. 4.5. Low and high magnification TEM images from sample #486, and EDS spectra for regions noted.

5. Residual Stresses

Two types of residual stresses were calculated. One calculation addressed the high local stresses that arise around the dispersed Mo particles which are induced by the discontinuities in thermal expansion coefficients and elastic moduli. The value of this "local" residual stress is independent of the size of the particles and is fixed by the material properties of the particle and matrix. Therefore we consider this stress to be a fixed quantity, such that its value is invariant once the materials selection has taken place. For Mo particle in a SiO_2 matrix undergoing a 1000 °C cool-down, this residual tensile stress is 590 MPa. The volume over which this stress is felt, however, scales with the particle size, such that the smaller the molybdenum particle, the smaller volume of glass effected by the local residual stress field. Therefore the only improvement that can be made with respect to the local stress is to keep the particles as small as possible.

The second type of residual stress calculated is the "gradient" stress, which results from the axial gradients in thermal expansion coefficient and elastic properties. The components of this stress(Fig 5.1) in the FGM's were computed by the finite element method (FEM). In this FEM analysis the Mo content was used to calculate homogenized properties of the SiO_2-Mo composite at discrete points along the gradient (Fig 5.2a).

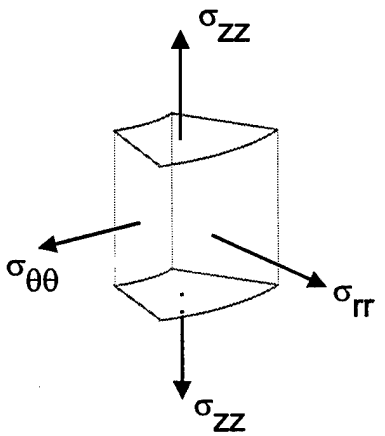

Fig 5.1. Nomenclature for components of stress in polar coordinates: radial stress, σ_{rr}, circumferential stress, $\sigma_{\theta\theta}$, and axial stress, σ_{zz}.

A cylinder of FGM of dimensions 11mm × 25 mm is modeled for analysis by an axisymmetric FEM mesh (Fig 5.2b) with a compositional gradient of TOTO or another model gradient. Assuming the surface of the cylinder is traction-free, the FEM is used to calculate the residual stresses for 1° C of cool-down, with units Pa/ °C (Fig 5.2c). (This analysis assumes that the physical properties are independent of temperature such that the stresses from any size of cool-down can be obtained from these results.)

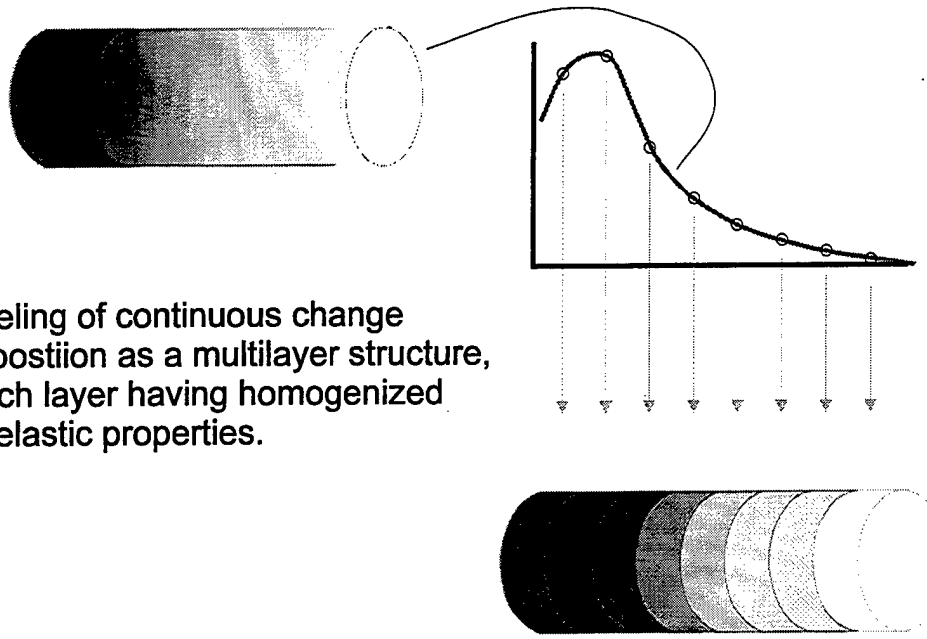

a) Modeling of continuous change in compostiion as a multilayer structure, with each layer having homogenized thermoelastic properties.

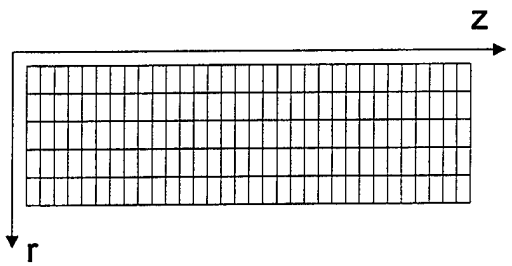

b) Modeling the multilayer using an axisymmetric finite element model. (Actual mesh used was much finer, containing rougly 400 elements.)

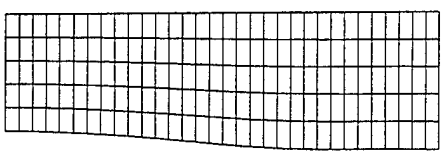

c) Finite element mesh deformed by cool-down. The gradient in effective coefficient of thermal expansion results in differential contraction along the length of the FGM. (Magnitude of deformation exagerated.)

Figure 5.2.

The results revealed that marked differences exist in these latter stresses between the samples with four different TOTO gradients, denoted 321, 662, 784, and 816 (Fig 5.3) respectively, with nearly a factor two higher surface stresses between these gradients (Fig 5.4). Thus, it is of interest to understand the origin of the difference between these two situations, but it is critically important to more generally understand the factors which determine the levels and spatial extents of residual stresses in FGM's. Four series of FEM calculations were performed to address this issue.

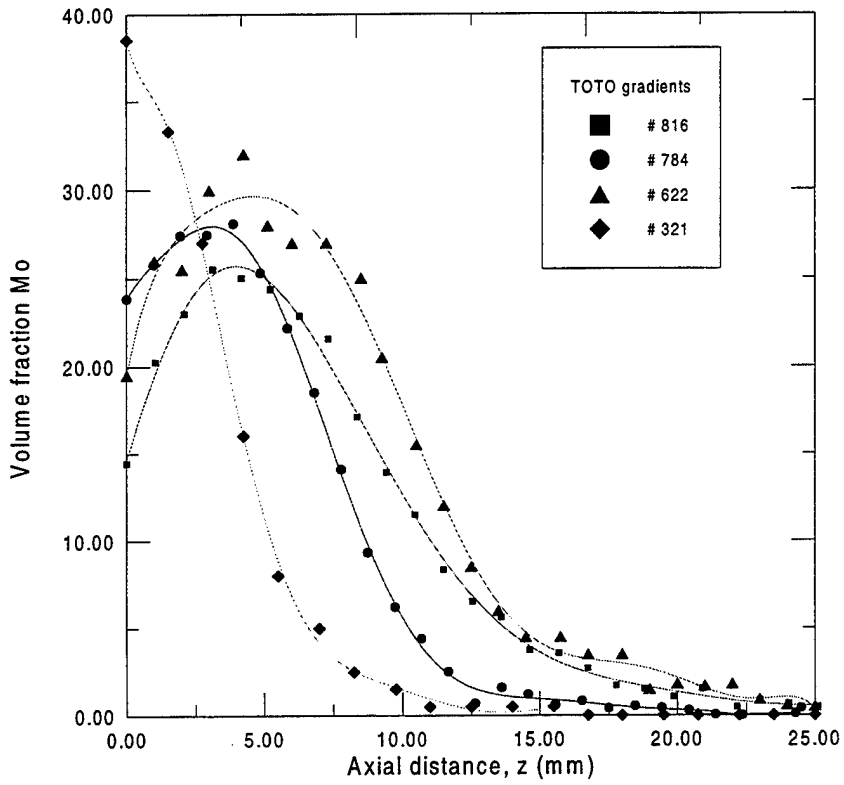

Figure 5.3. Experimentally determined composition profiles from samples from four different batches of FGM's that were used for calculations of stress distribution throughout the samples.

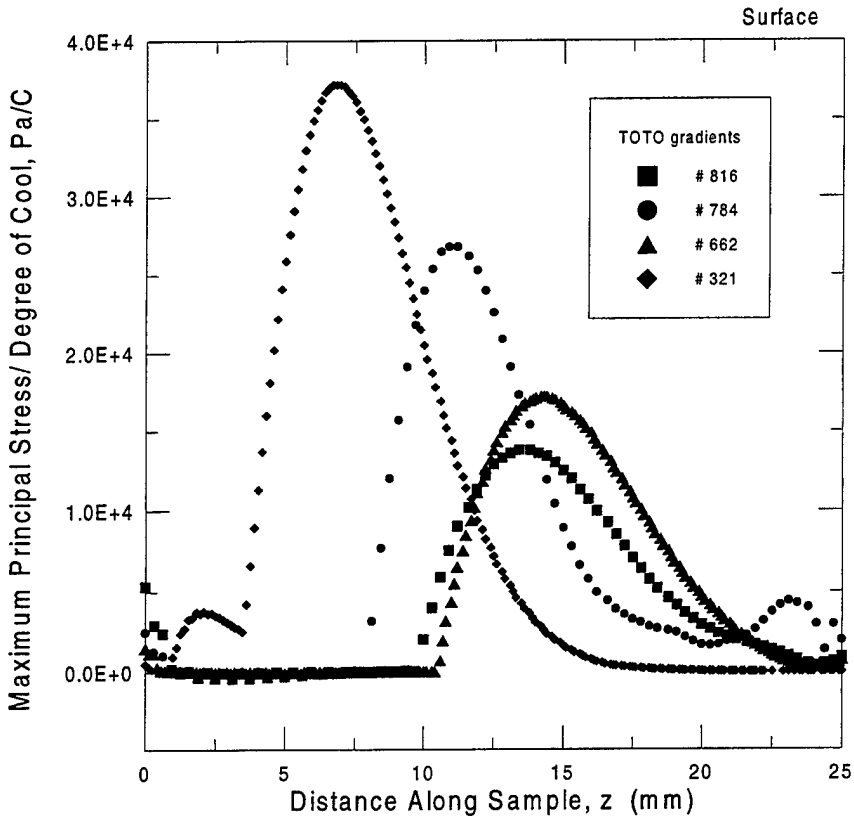

Figure 5.4. Maximum principle stress at the surface versus axial distance down the sample. The large peak represents the axial stress being the largest component; whereas, at the left the circumferential component corresponds to the largest principle stress.

The first series of calculations were done keeping the length of the samples constant and assuming the 662 gradient, but letting the diameter vary from ¼ of the standard (11 mm) value to much larger. The results are represented by plotting the stresses at the surface, Fig. 5.5, and along the center-line, Fig. 5.6, versus position along the cylinder axis. All the stress components oscillate versus position along the axis. At the center-line the radial stresses equal the circumferential ones; whereas, at the surface the radial stresses vanish. The major trend is illustrated in Fig. 5.7 for the axial stresses, and can be seen by inspection for the circumferential components from Figs. 5.5(b) and 5.6(b). As the diameter, D, decreases such that it is much less than the sample length, L, the stresses all vanish relative to the values at large D/L. In contrast, at large D/L, the stresses approach an asymptotic situation in which the in-plane stresses are significant and largest, although compressive in this case, at the sample faces. The axial stresses vanish in the interior, but are large along the surface. These surface stresses can be particularly large if there is an abrupt change in composition within a component.

A second set of calculations illustrates critical aspects of the form the gradient. The computations are all for the standard TOTO size (D/L = 0.44). Here a series of idealized gradients was assumed with the same end values and average slope, d/dx (v_{Mo}). Each of these model gradients had a constant second derivative, $\kappa = d^2/dx^2$ (v_{Mo}) (the "curvature" of the compositional gradient). The first case compares two situations with

positive and negative curvature as depicted in Fig. 5.8. The axial stresses at the surface are plotted versus axial position in Fig. 5.9. There are two interesting results, namely, that the large oscillation in stress seen previously is eliminated and secondly, the sign of the stress depends upon the sign of κ, with a negative "curvature" giving largely compressive axial stresses at the surface. Clearly, this would be advantageous for the typical situation that the surface flaws are more severe than those in the interior, where the residual stresses are of opposite sign. Further calculations varied the intensity of the curvature of the composition profile, as shown in Fig. 5.10, with all cases having negative curvature. The stresses plotted in Figs. 5.11 and 5.12 show the axial dependence for the stresses at the surface and along the center-line. With these types of gradients the axial stresses are greater in magnitude than the circumferential components. Moreover, the intensity of the stresses increases with the curvature of the composition profile as shown directly in Fig. 5.13. Finally, it is noted that the samples with constant composition gradients have small but not vanishing stresses; this arises because of a nonlinear model for the variation of the thermal expansion coefficient. For a linear variation in effective thermal expansion coefficient, the stresses exactly vanish.

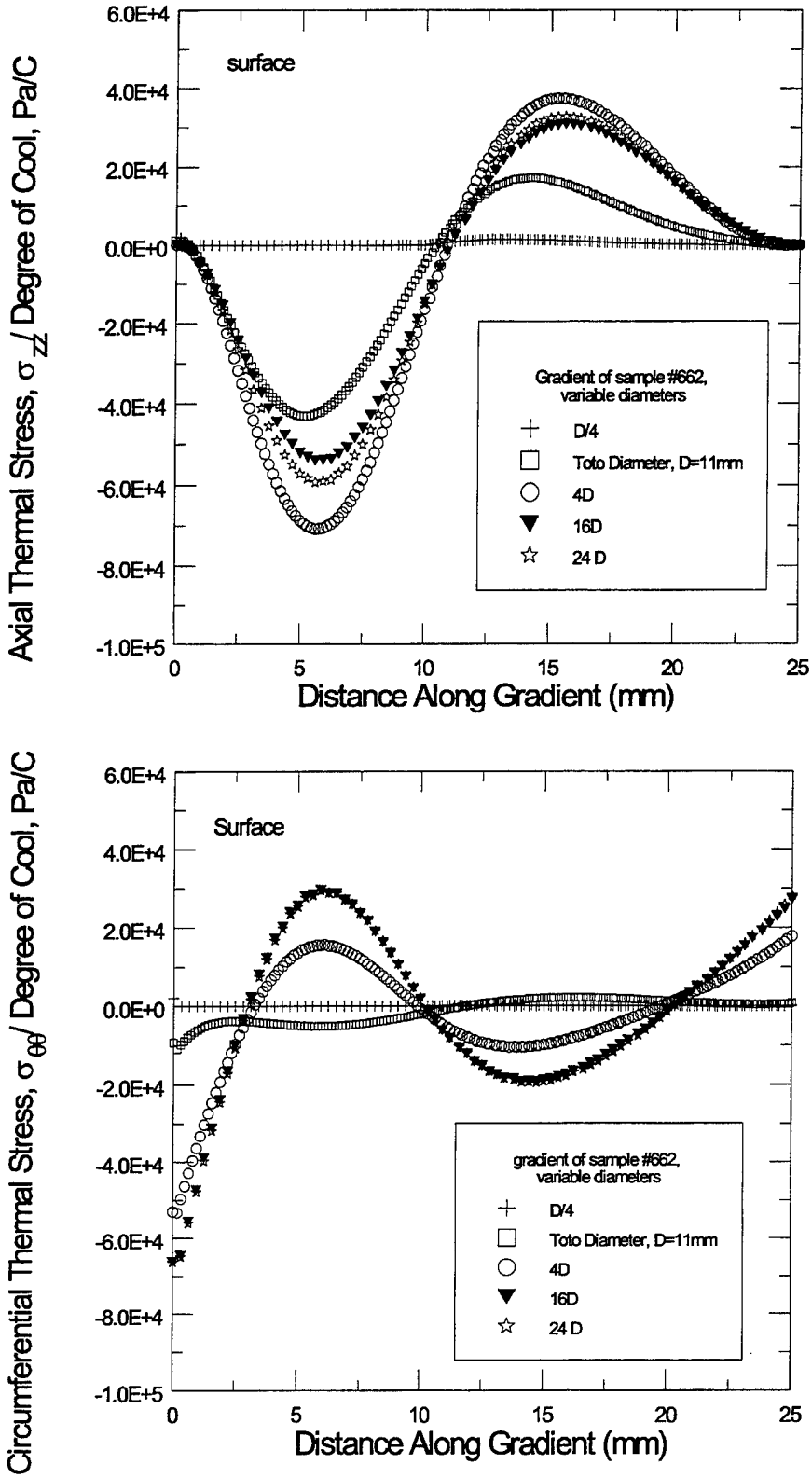

Fig. 5.5. Variation with axial position of axial (a) and circumferential (b) components of the residual stress at the surface for samples with different diameters and the 662 gradient.

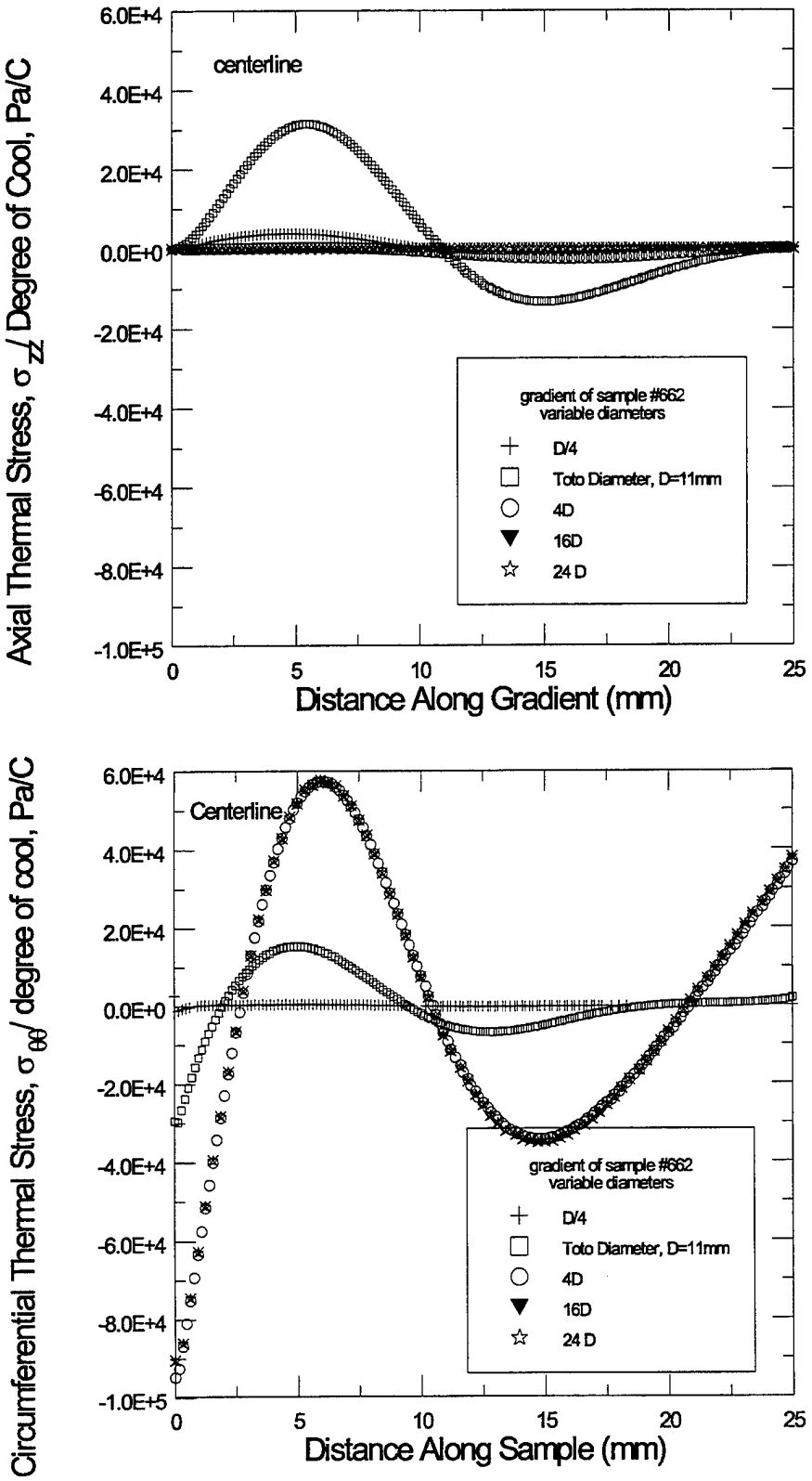

Fig. 5.6. Variation with axial position of axial (a) and circumferential (b) components of the residual stress at the center-line for samples with different diameters and the 662 gradient.

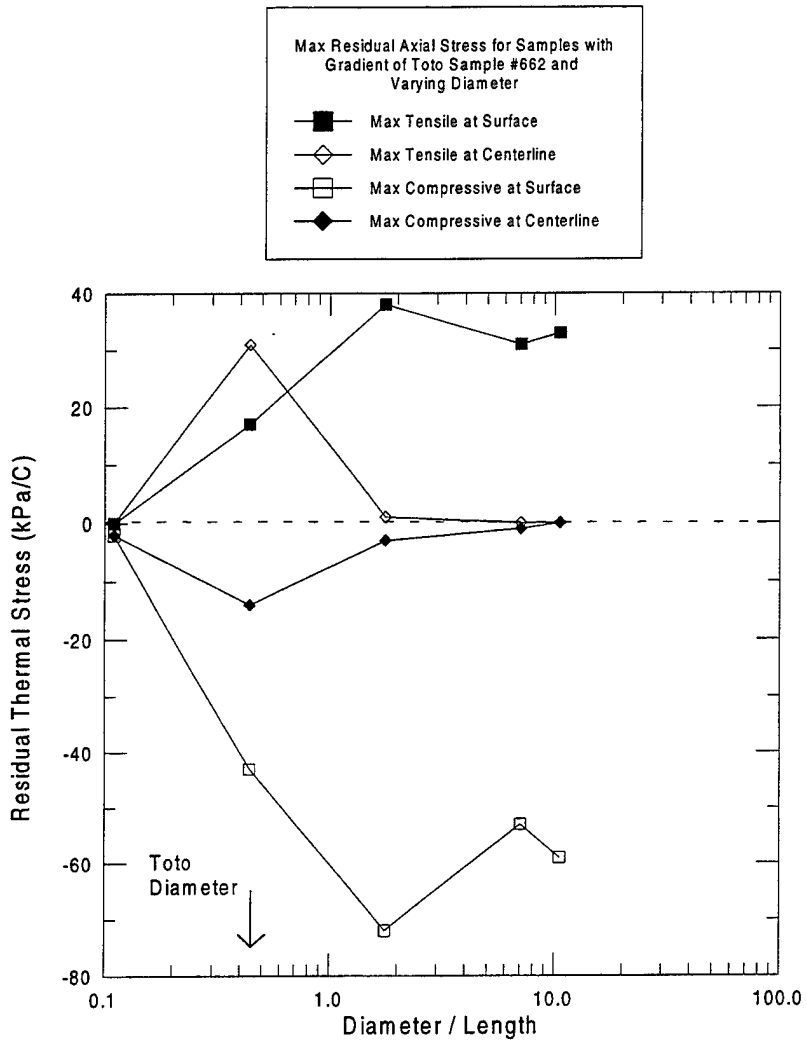

Fig. 5.7. Dependence of the peak values of the axial stress at various locations with sample diameter.

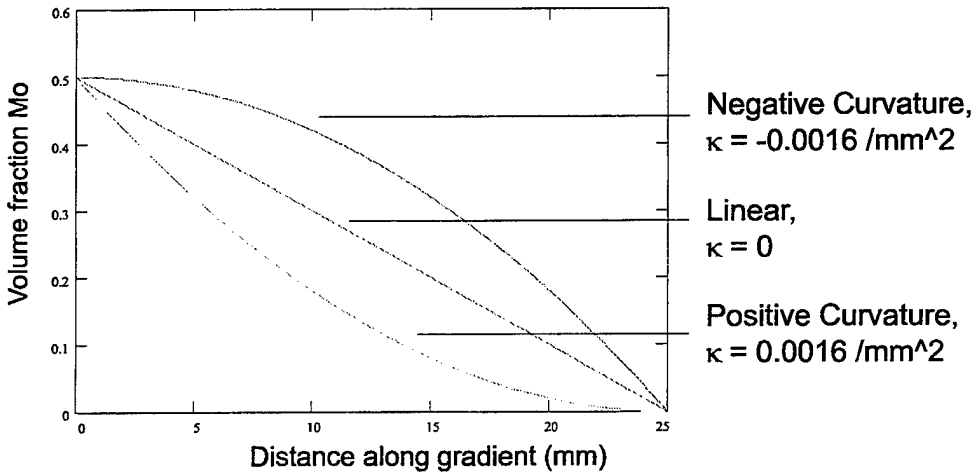

Fig. 5.8. Composition gradients with positive and negative curvature used for stress analyses.

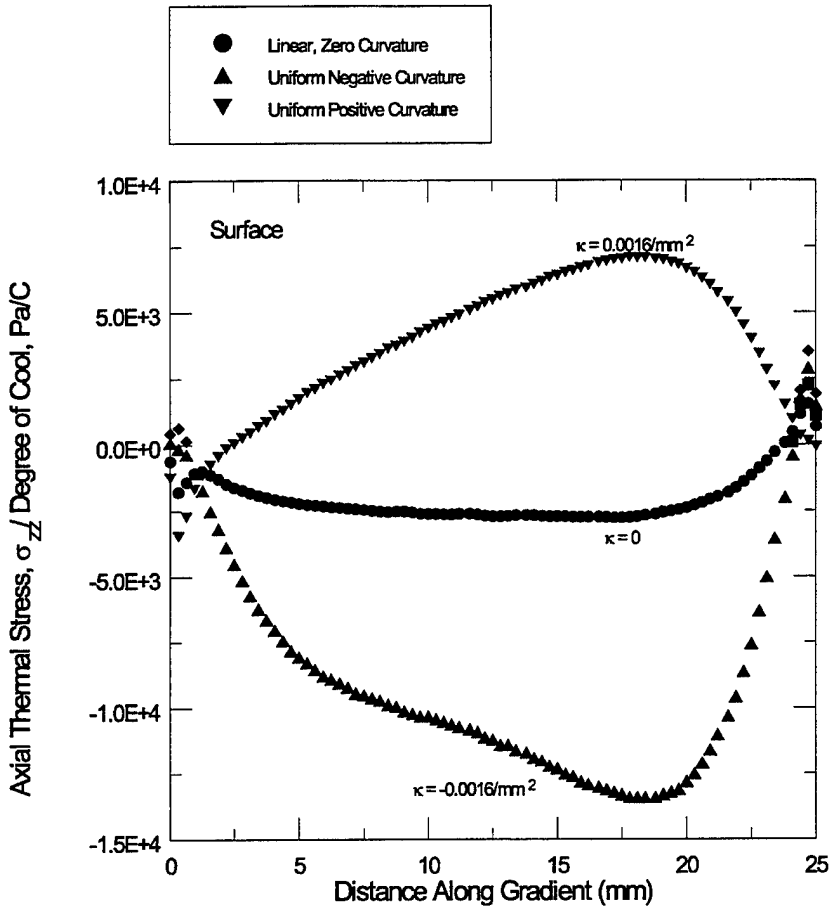

Fig. 5.9. Variation with axial position of axial component of the residual stress at the surface for samples with composition gradients having constant positive or negative curvature.

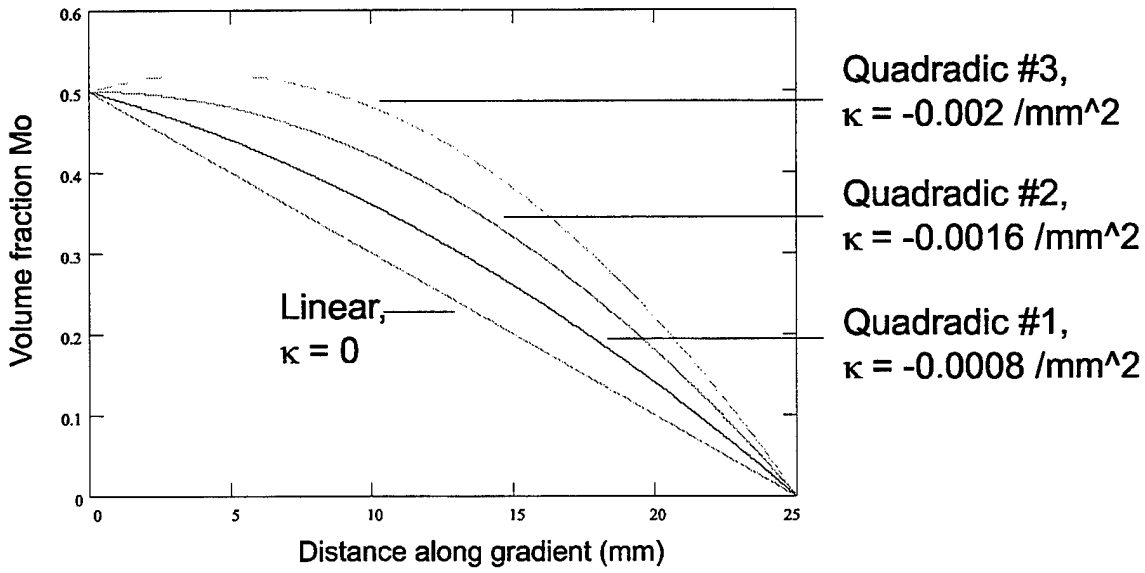

Fig. 5.10. Composition gradients with various negative curvatures used for stress analyses.

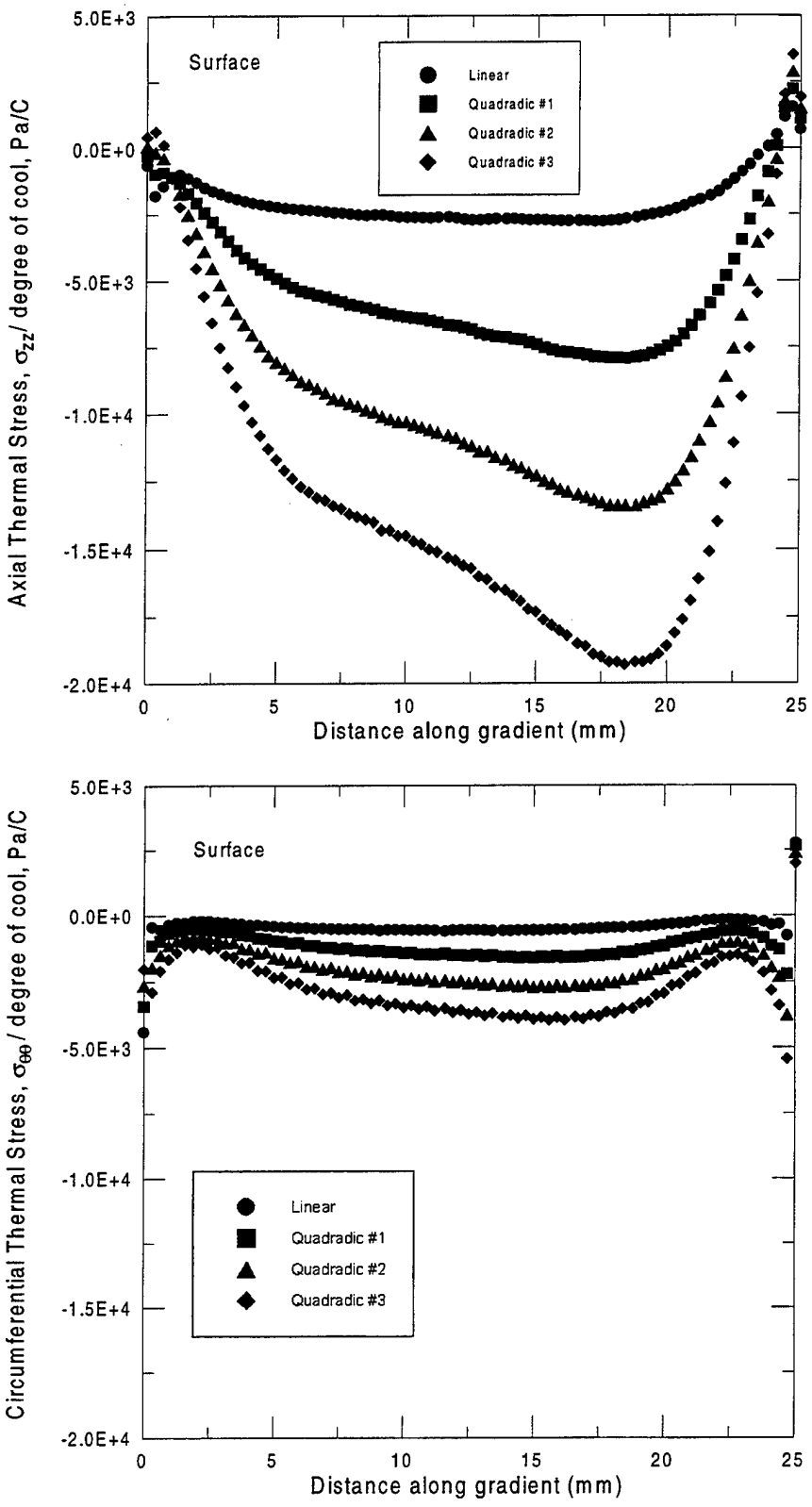

Fig. 5.11. Variation with axial position of axial (a) and circumferential (b) components of the residual stress at the surface for samples with different curvatures for the composition gradient.

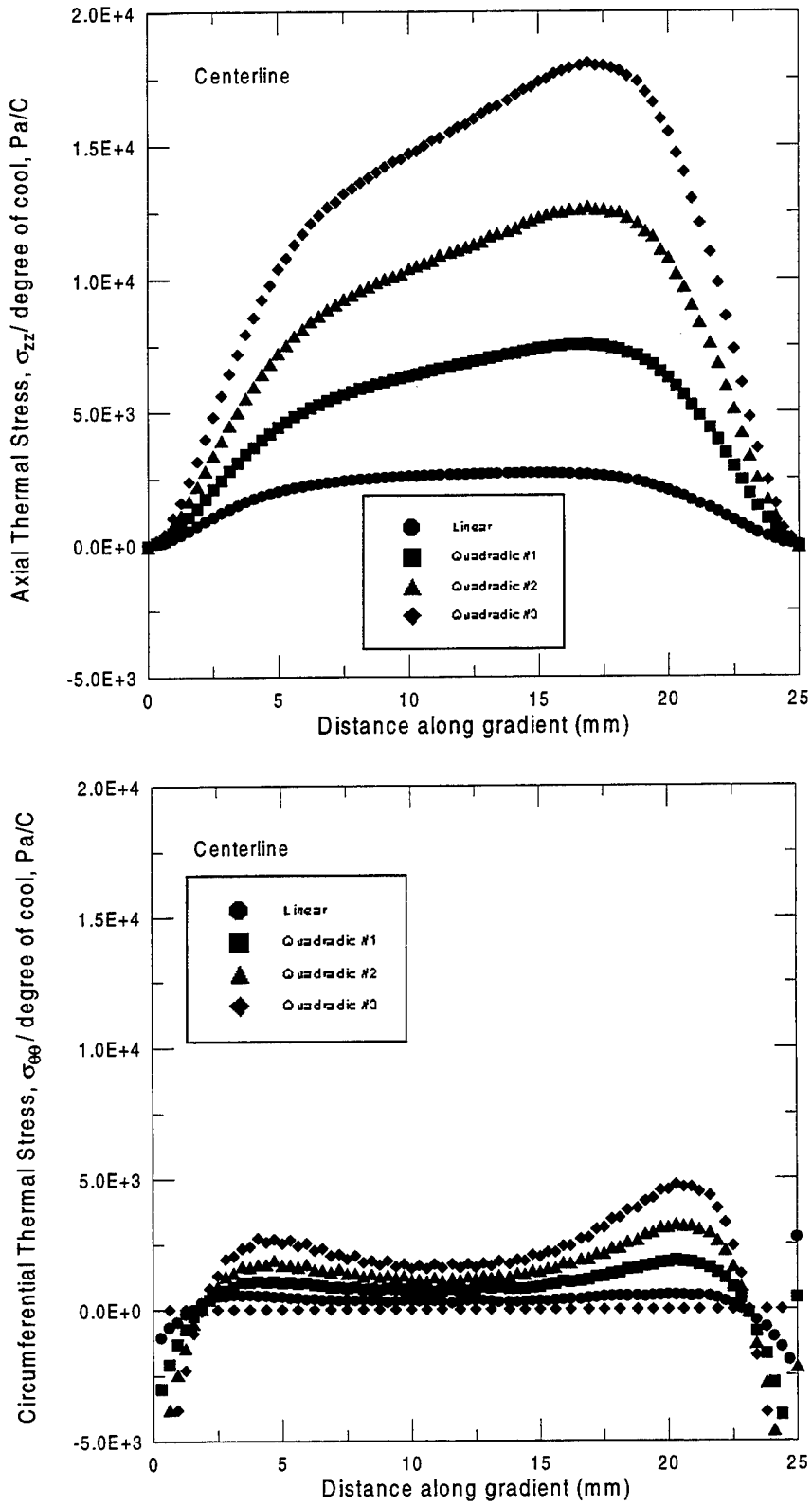

Fig. 5.12. Variation with axial position of axial (a) and circumferential (b) components of the residual stress at the center-line for samples with different curvatures for the composition profile.

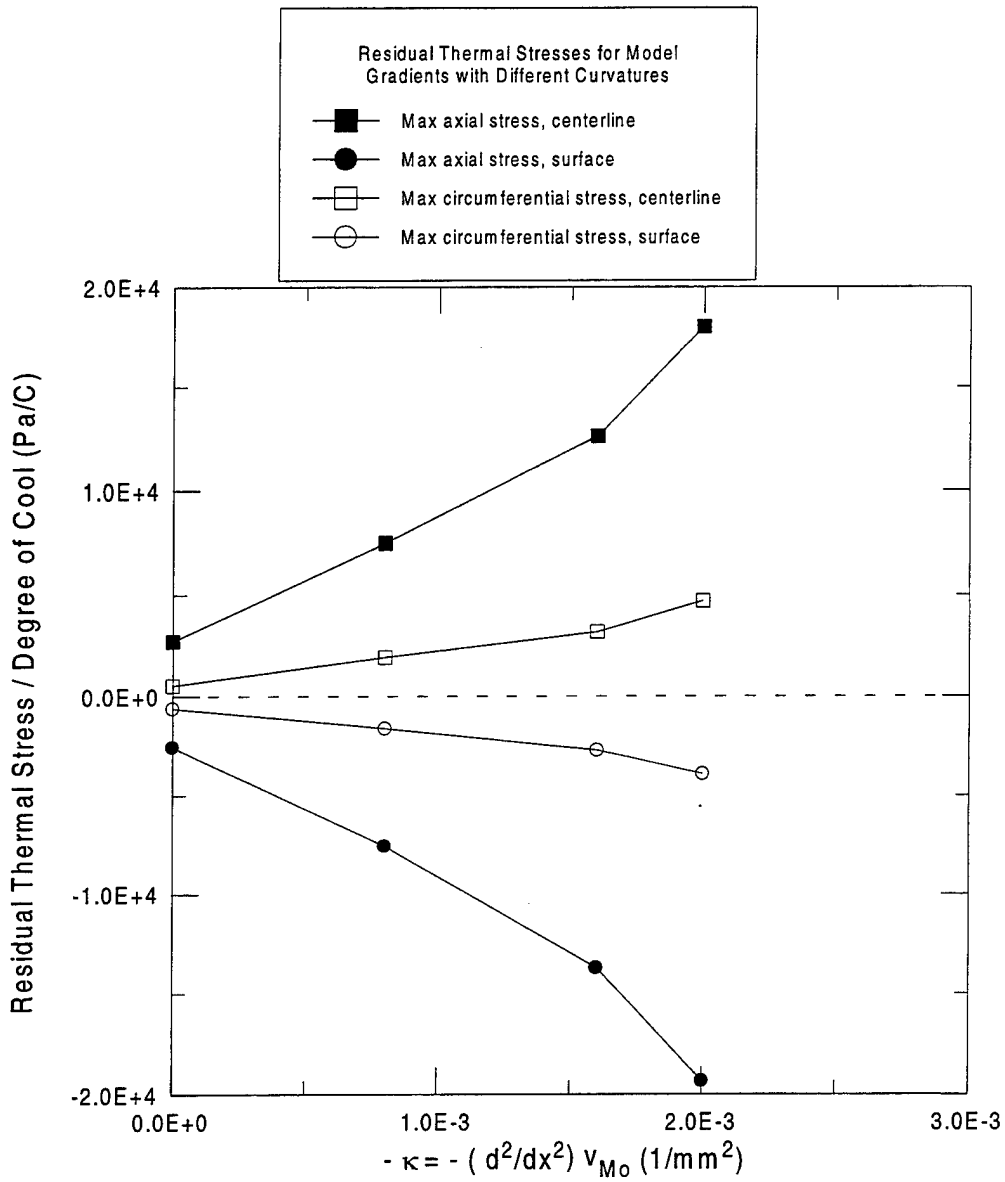

Fig. 5.13. Variation of peak values of stress component with magnitude of the curvature of the composition profile.

In order to further investigate the connection between the curvature in the composition and the residual thermal stresses a series of model sigmoidal gradients, with a shape closer to that produced with by the TOTO slip-casting process, were used for calculations. These gradients are characterized by a modified error function, ERF(z), Fig 5.14a. This allows for the development of a series of model gradients with the same beginning and ending volume fraction of molybdenum (20-0%). A cylinder of the same dimensions as the TOTO specimens was analyzed, with diameter of 11 mm and 25 mm length. The gradient was modified such that the average slope of the gradient is the same for all of the model gradients, although as can be seen in Fig 5.14b, the curvature in the gradient, $\kappa = d^2/dx^2\ (v_{Mo})$, was varied drastically.

The residual stresses for these error function gradients were again calculated using the finite element method. The variation of the residual axial stresses σ_{zz} and circumferential stresses σ_{tt} at the surface is displayed in Fig 5.15. The variation of these stress components along the centerline is shown in Fig 5.16. It is clear that the residual stresses vary drastically along the length of the sample, with the location of the peak stresses roughly corresponding to the location of the peak curvature, κ. When the peak tensile stress component is plotted against the peak curvature (fig 5.17) a nearly linear correlation is found between the stress and the logarithm of κ.

At this point it is clear that the residual stresses in a FGM are determined in part by the relative scales of the radius and length. However, the role of the gradient shape may not only be felt in the curvature effects discussed above, but may also introduce another "natural" gradient length scale. As shown in Fig 5.18 it is possible to consider a series of FGM samples with the same diameter and shape of gradient, with the exception of extended regions of constant composition. The results of finite element solution for the surface stresses in such a series of samples are displayed in Fig 5.19a,b. Stresses along the centerline show similar trends. It is clear that for a range of lengths from 15-50 mm with a diameter of 11 mm the axial stresses are only weakly affected by the addition of the regions of constant composition. The circumfrential stress for these cases, however, vary substantially with the addition of these homogeneous regions. However, the total magnitude of these stresses is nearly constant and much smaller than the axial stresses; as such these variations are unlikely to effect the mechanical properties of the FGM.

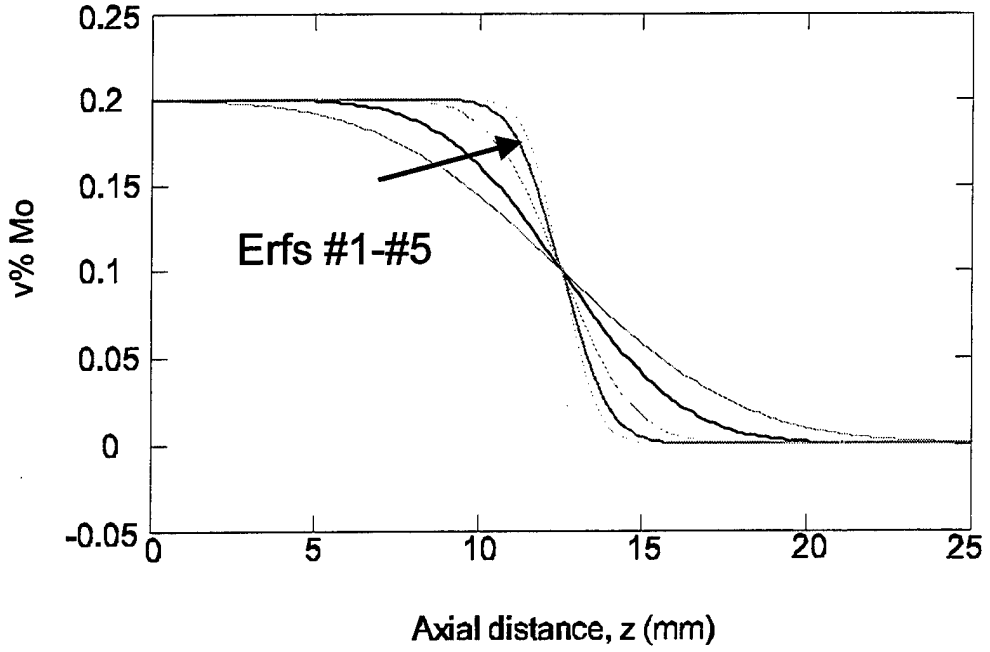

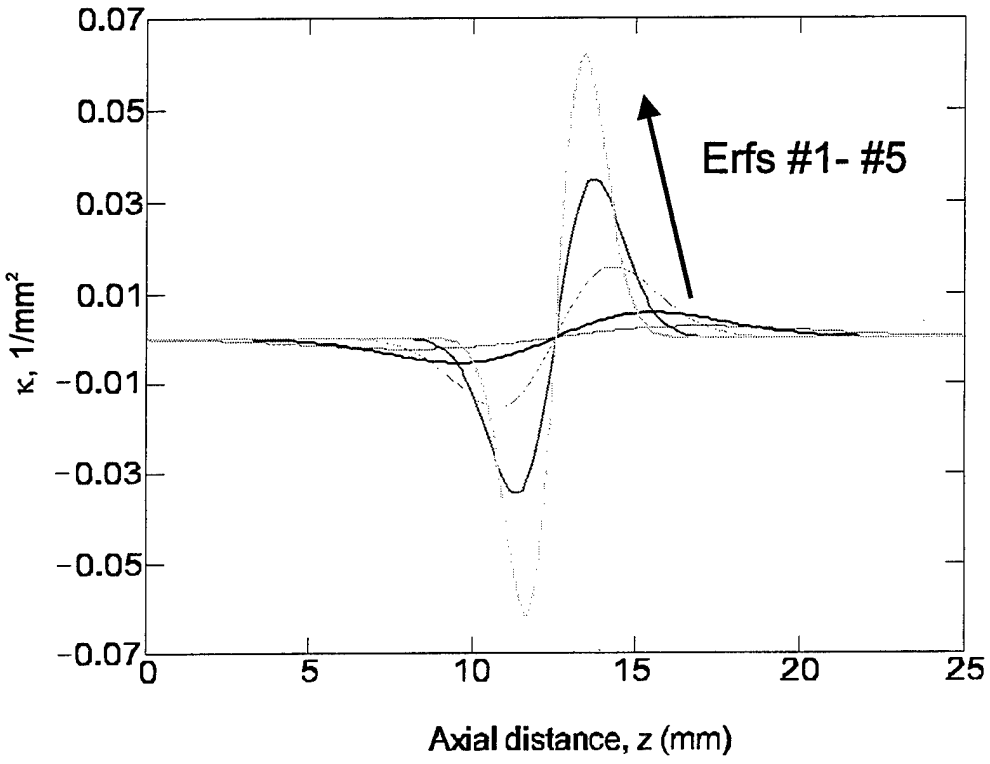

Figure 5.14. Sigmoidal composition gradients with various curvatures used for stress analyses in (a) and plots of the curvature of the composition profiles in (b).

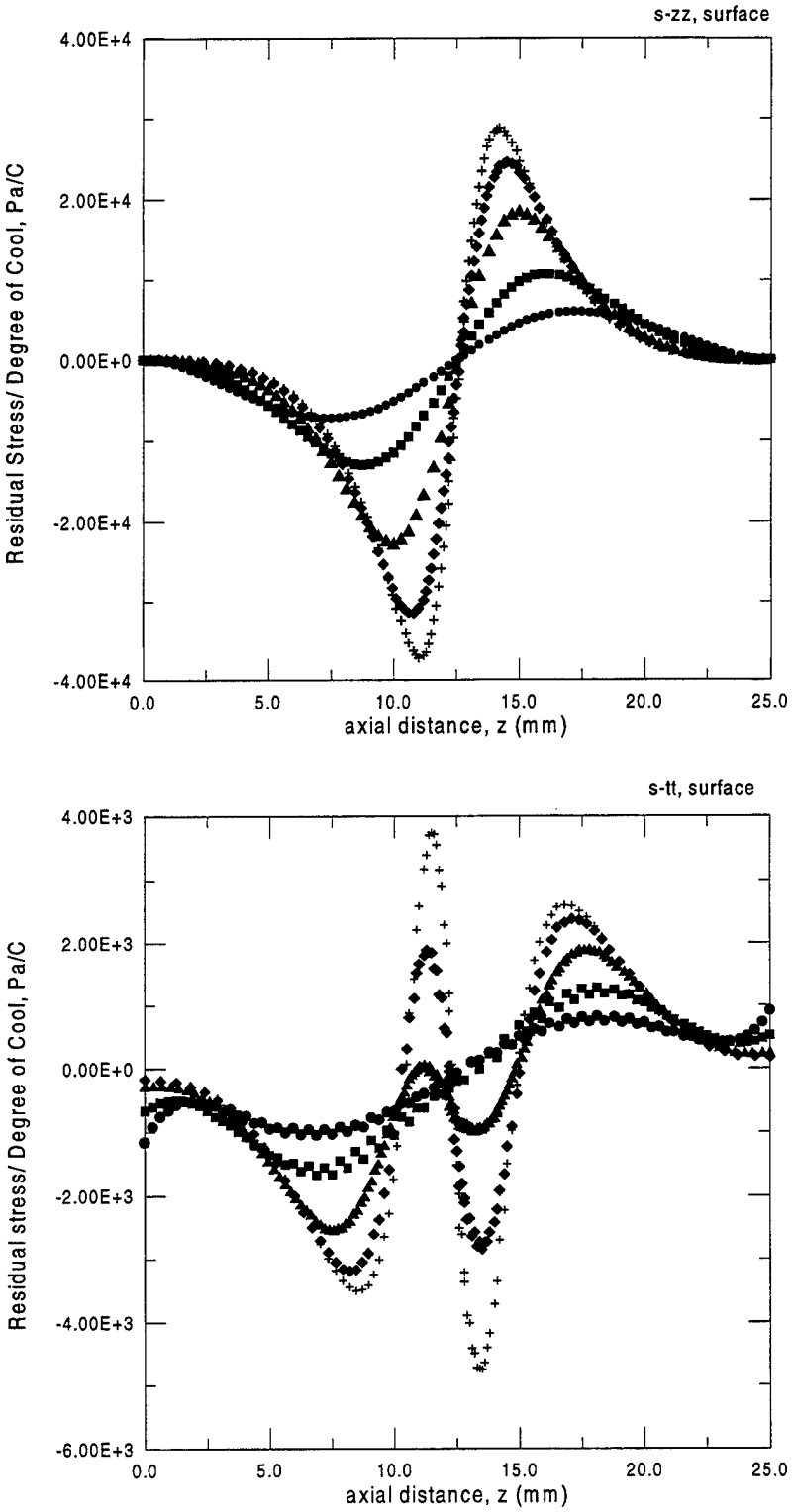

Figure 5.15. Variation with axial position of axial (a) and circumferential (b) components of the residual stress at the surface for samples with different curvatures for the sigmodial composition profiles.

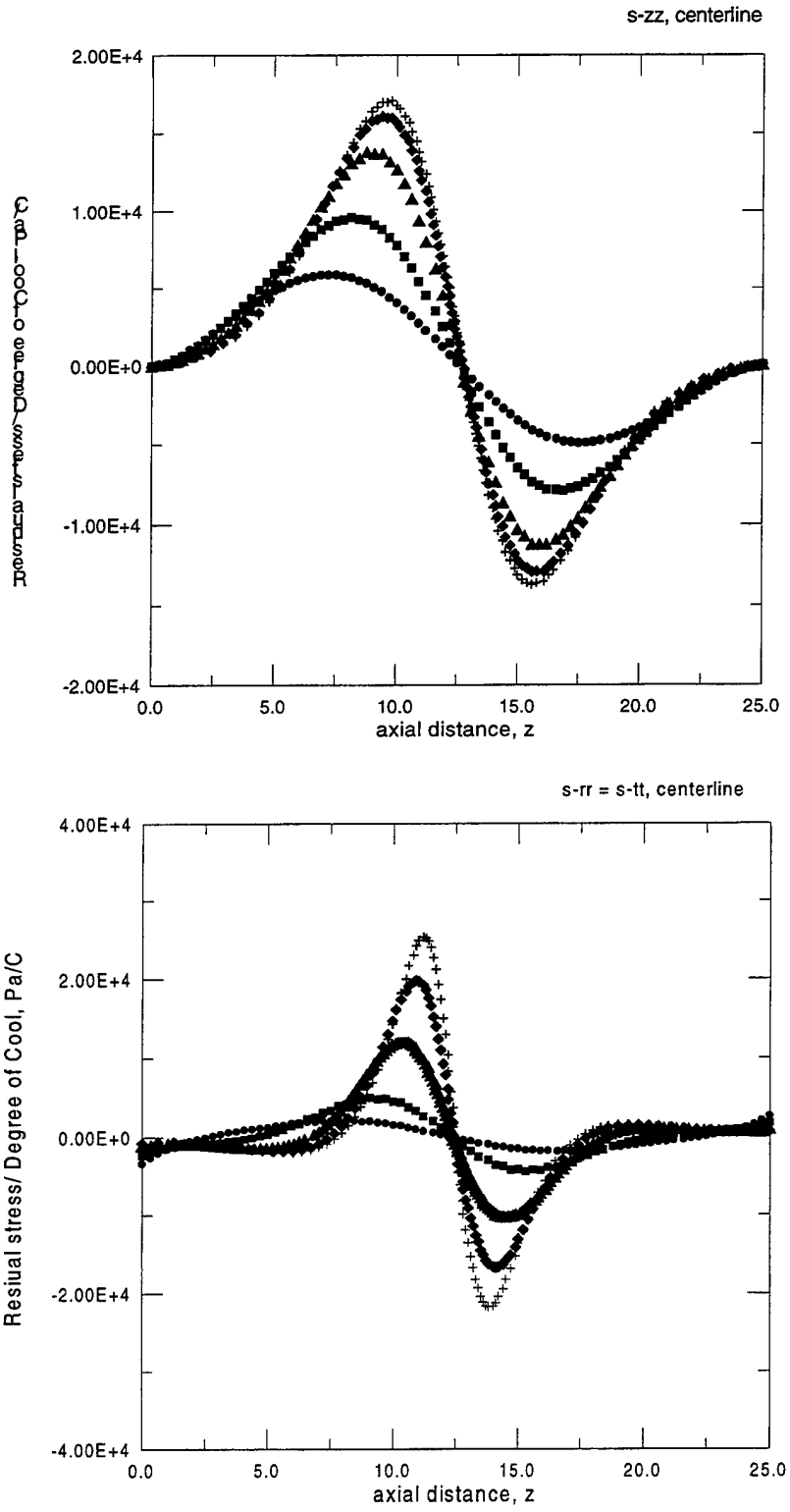

Figure 5.16 Variation with axial position of axial (a) and circumferential (b) components of the residual stress at the center-line for samples with different curvatures for the sigmodial composition profiles

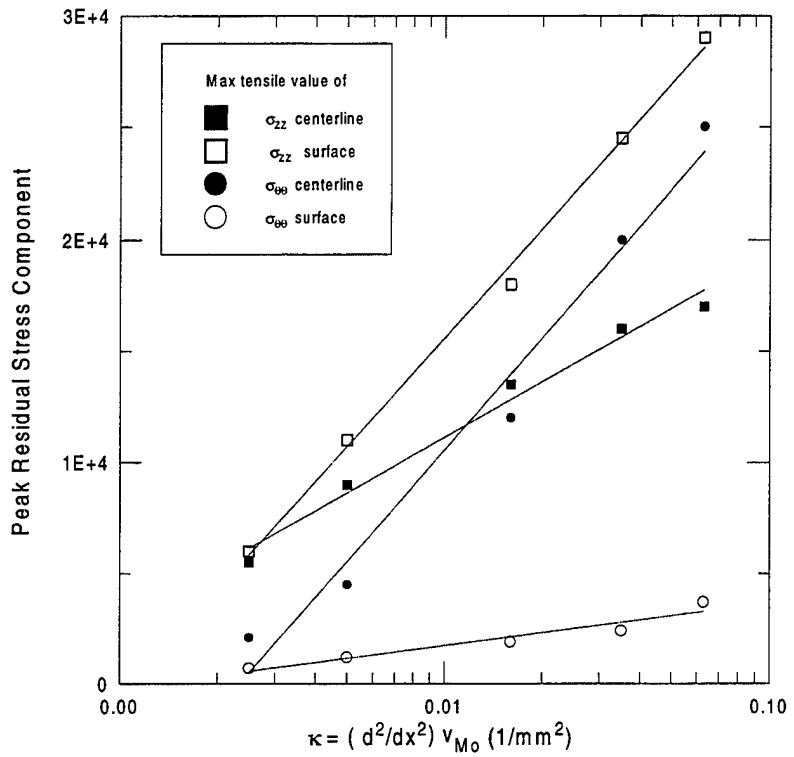

Figure 5.17. Variation of peak values of stress components with magnitude of the curvature of the various sigmoidal composition profiles.

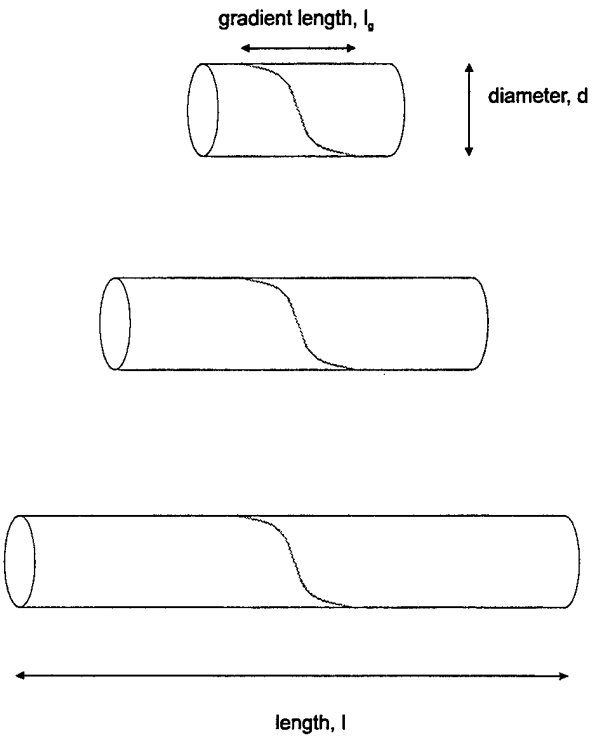

Figure 5.18. Sketches showing series of samples with specific sigmoidal composition profiles, but different sample lengths used for residual stress analysis.

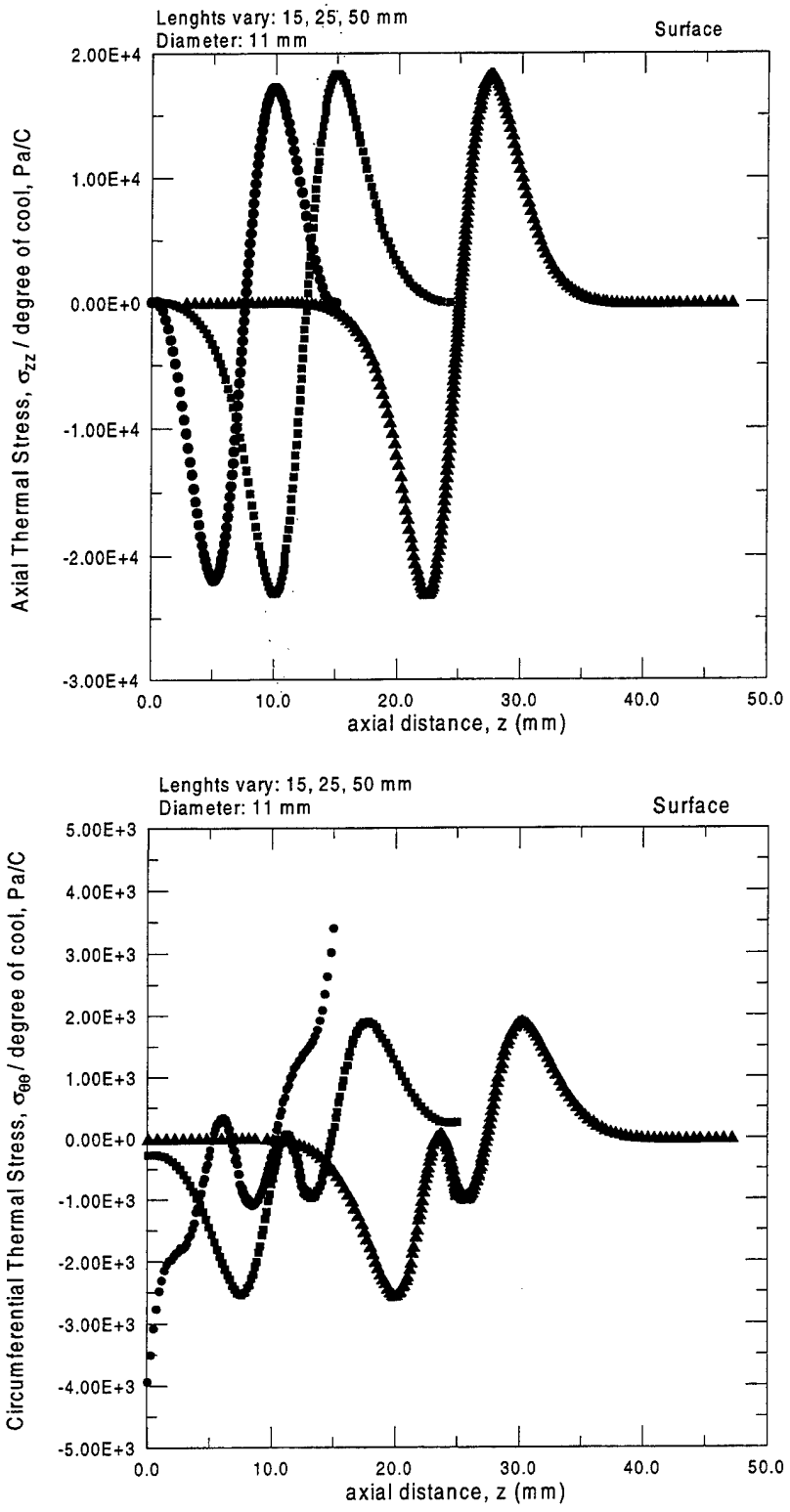

Figure 5.19. Variation with axial position of axial (a) and circumferential (b) components of the residual stress at the surface for samples with different lengths but with a fixed sigmodial composition profiles

Since all of the preceding calculations were done for solid cylinders, the translation of these results to the actual TOTO geometry is necessary. For a cylinder with a hole along the axis a comparison of the residual stresses for various hole diameters has been performed. A single TOTO gradient, #816, was arbitrarily selected for this comparison.

Assuming that the part is sintered free-standing, the hole adds the new boundary condition of the inner surface (as well as the outer surface) being traction free. Finite element calculations were performed for various hole diameters (Figs 5.20a and b).

The results show that even for very large centerline holes (~1/2 total diameter) the surface stress state changes little due to the presence of the hole (Fig 5.20b). Focusing on a single axial location, z~14mm (the location of the highest stresses, see Fig 5.4), the variation in the residual stresses with radial location is displayed in Fig 5.21. For all hole diameters studied, for ($r < 4$ mm) it can be seen that the stresses are virtually identical. This indicates that the results obtained for solid cylinders can be considered accurate for the stresses on the surface of the cylinder, where the stresses are the highest. However, for cylinders with "steps" in the hole diameter or blank holes, such statements cannot be made. Where "sharp" steps exist the elastic stresses are formally infinite. If a known fillet radius exists between two hole diameters or at the hole bottom, then the magnitude of the residual stresses depends entirely on the size of the fillet radius. In this case a detailed analysis would be required for an actual TOTO geometry.

Although these calculations fall far short of giving general solutions for the stresses in all cases, they provide a basis for a set of provisional guidelines for the design of FGM's. These are to be followed where possible:

A. For reducing the effect of the local stresses, reduce the particle size of the molybdenum.

B. For reducing the magnitude to the gradient stress:

1. produce gradients with linear variation in the thermal expansion coefficient,
2) design the component with smaller diameter/length ratio,
3) produce a gradient with positive "curvature",
4) produce a gradient with the smallest magnitude of "curvature", i.e., linear. Clearly more work is needed to explore these effects for cylindrical and other more complex geometries, and to better quantify them.

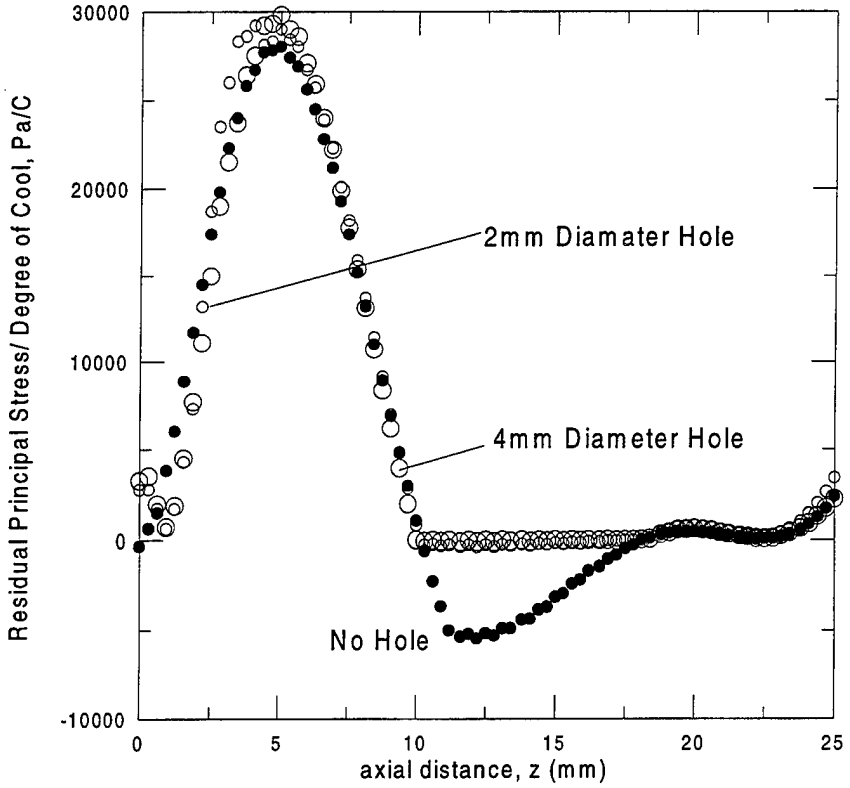

Figure 5.20. Variation with axial position of maximum principle stress along the inner (a) and outer (b) surface of FGM cylinder for various inner hole diameters for TOTO gradient #816.

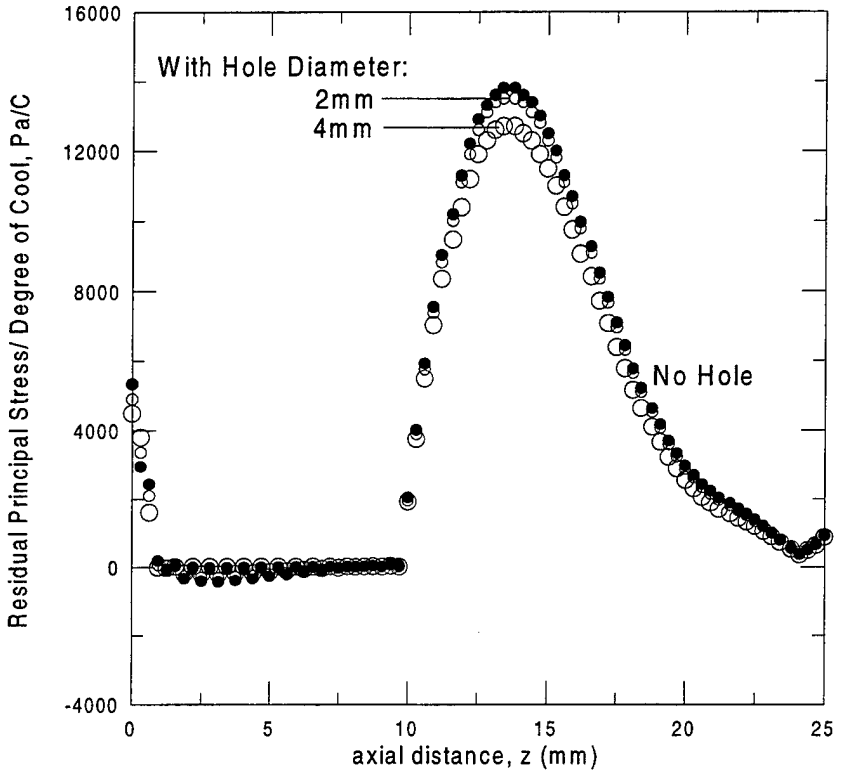

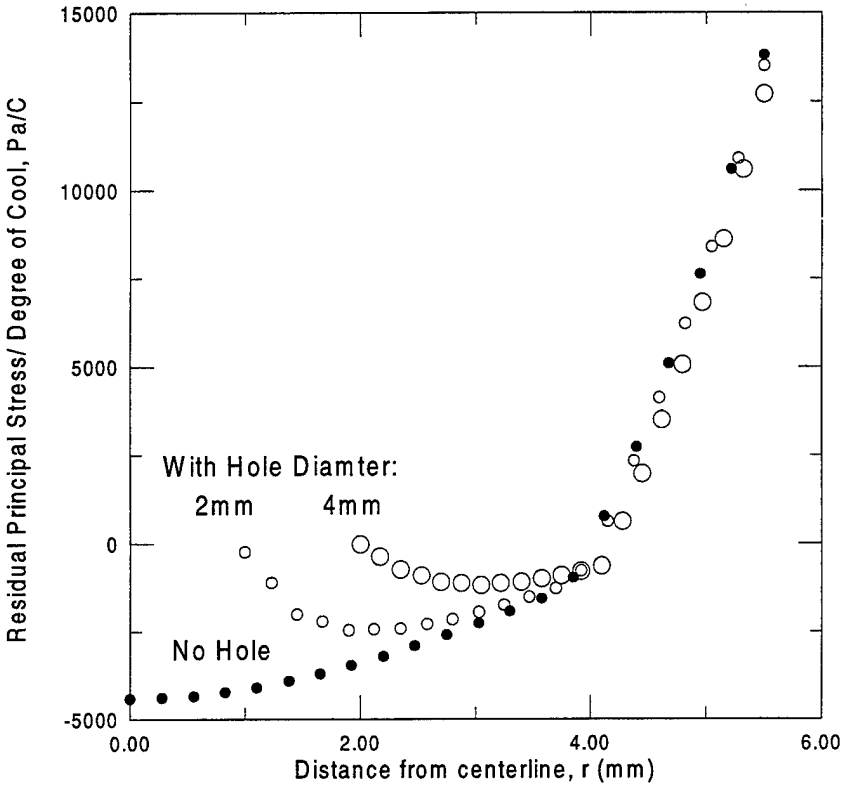

Figure 5.21. Variation with radial position of maximum principle stress for the FGM cylinder for various inner hole diameters for TOTO gradient #816. All values for single axial position, z =14 mm, the highest stress region.

6. Mechanical Strength

Work on the statistical treatment of the strength of Mo-SiO_2 FGM's has been undertaken which incorporates results of the residual stress calculations. This work seeks to predict the behavior of the FGM under general loading conditions and geometries. A summary of the results and a brief description of the techniques employed are provided below. For purposes of identification, the samples received from TOTO are divided into groups labeled as batch two, batch three and batch four (e.g. as outlined previously).

6.1 Statistical Treatment of Strength

Mechanical strength in brittle solids is often described by "weakest link" statistical mathematics. The basis for this description lies in the assumption that there is a distribution of flaws in the material which act as possible initiation sites for failure. Whether a particular site causes the failure or not is determined by the stress state existing in the material and, due to the spatial distribution of flaws, the total volume or surface area of the component. In typical glasses the major flaws arise from surface damage due to handling. However for the FGM considered here there is reason to suspect that an additional *internal* flaw population exists due to the composite nature of the material and the magnitude of the local residual stresses previously discussed (e.g., see section 5).

The severity of this internal population is unknown but prior microstructural investigation (Tomsia et al, Sept.-Nov., 1996) implies that flaw sizes on the order of the Mo conglomerate size are possible. This point remains to be investigated and relates strongly to the methodology used below.

The issue of combining the residual stress calculations and an applied stress field in order to develop a methodology for predicting survivability rates of components subjected to arbitrary stress fields in service has been addressed. This methodology considers data from a set of simple mechanical tests and, based on the statistical treatment of the test results, describes the expected reliability of the device. The basis for this approach is Weibull statistics. A simple case is considered here although a more complete analysis for any particular design is possible based on the concepts herein.

For the purposes of this analysis, we consider the surface of the component to be the most important source of flaws leading to failure. With this specification the failure probability of an elemental surface area loaded to stress, σ, may be expressed as:

$$f = \left(\frac{\sigma}{\sigma_o}\right)^m \qquad (6.1)$$

where σ_o is a scaling parameter, and both σ_o and m are determined experimentally. The failure probability for an entire component is then described by:

$$F = 1 - \exp\left[-\int_S \left(\frac{\sigma}{\sigma_o}\right)^m dS\right]. \qquad (6.2)$$

From Eq. 6.2 it is easily seen that the failure probability scales with the size of the component through the integral which is carried out over the surface, *S*. The effects of residual stress are easily incorporated by summing the applied and residual stresses and substituting this sum, as σ, in Eq. 6.2.

6.2 Strength Testing

Strength tests were conducted on two of the three batches received from TOTO: batches three and four. Sections of each sample were cut from the as-received cylinder as shown in Fig. 6.1-a. This "cap" geometry allowed testing of the as-manufactured surface flaw population while leaving much of the sample available for future testing needs. While approximately 90% of batch three and 50% of batch four remained after cutting, none of the samples from batch two survived this same process.

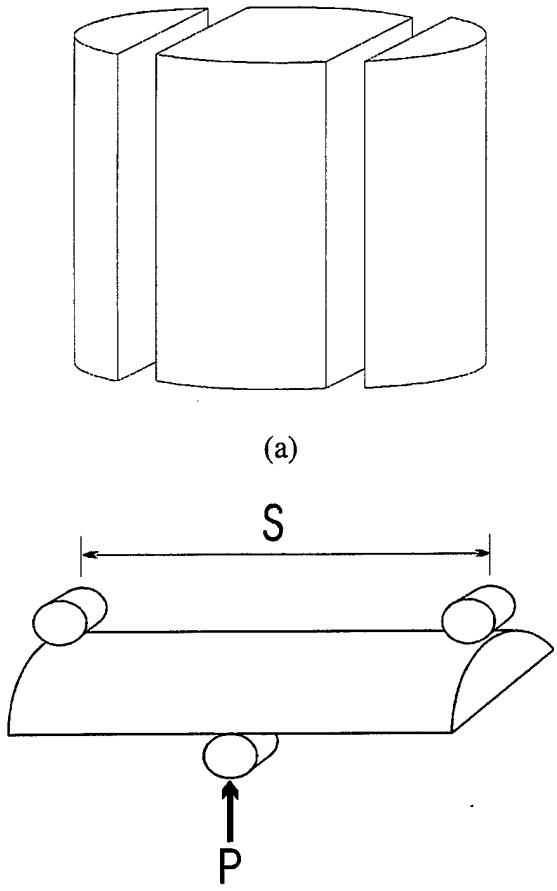

Figure 6.1. Schematics of (a) cutting location for samples and (b) testing geometry used in this study.

The residual stress state in the FGM appears to be of some importance as is implied in Fig. 6.2 where the results of 3-point bend tests on the FGM are shown versus the normalized distance from the Mo-rich end[1]. These results show a slight bias toward failure in the silica-rich end even though the stress state in the three point bend test is symmetric about the beam midpoint. This region of higher failure probability does coincide with the region previously noted to have a tensile residual stress state.

[1]note that a x-coordinate of 0.5 corresponds to the location of maximum applied tensile stress during the bend test.

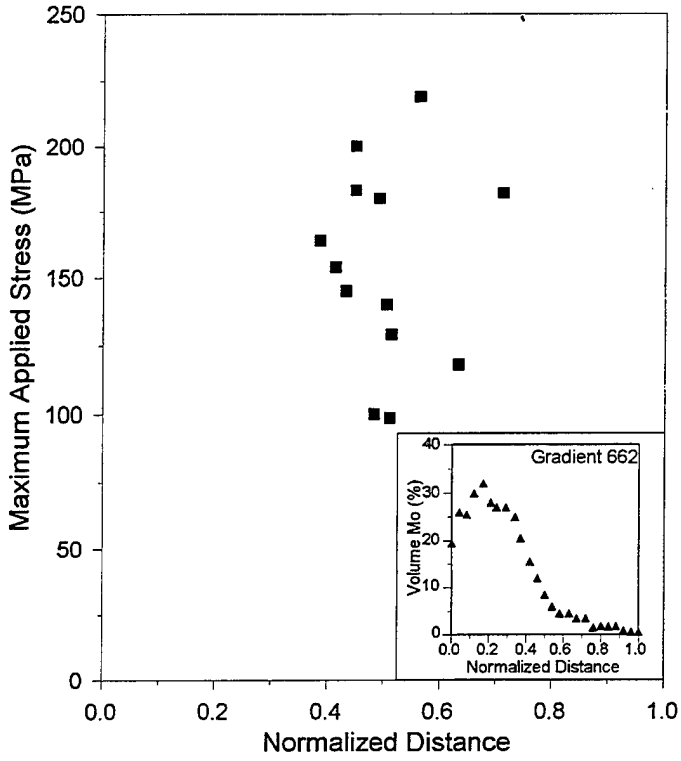

Figure 6.2. Distribution of failure sites for samples tested from batch three.

We have investigated the effect of specimen geometry and residual stress on failure probability in the case of a component in 3-point bending. For a first iteration of the modeling, it is assumed that the characteristic parameters do not depend upon the Mo content of the material (and by implication that the residual stress effects are not large for fast fracture, a result subsequently justified). The specimen geometry effects then follow from Eq. 6.2.

6.3 Batch Three Tests

Tests were conducted on batch three samples in 3-point bending with a span, S, of ≈20 mm (see Fig. 6.2-b). Results from these tests, shown in Fig. 6.3, yield failure stresses somewhat higher than those typical of glass (50-100 MPa). This is not surprising considering the minimal amount of material subjected to tensile stresses in the geometry tested. When fit to a two parameter Weibull relationship (Eq. 6.2) these data yield σ_o = 280 MPa and m = 4.

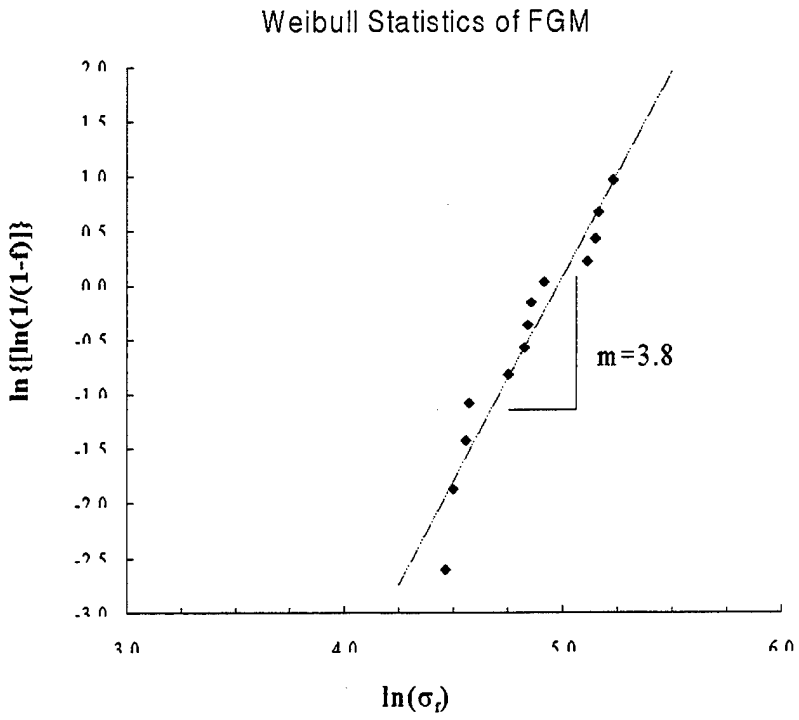

Figure 6.3. Results of 3-point bend tests conducted on the "cap" geometry samples from batch three.

Using the two fit parameters, σ_0 and m, obtained above, predictions based on the Weibull model of the FGM under other loading conditions may be made. Fig. 6.4 compares the 3 point bend, "cap" geometry with predictions for tensile loading of a 3 mm square beam 22 mm in length and for 4-point bending of 3 mm square beam as have been tested (section 3.3). It can be seen that the fracture stress levels in tension and 4-point flexure are much closer to the expected values for typical glass. It should be noted that although typical test geometries have been modeled here, the modeling is applicable to general stress states and elaborate geometries albeit with considerably greater complexity.

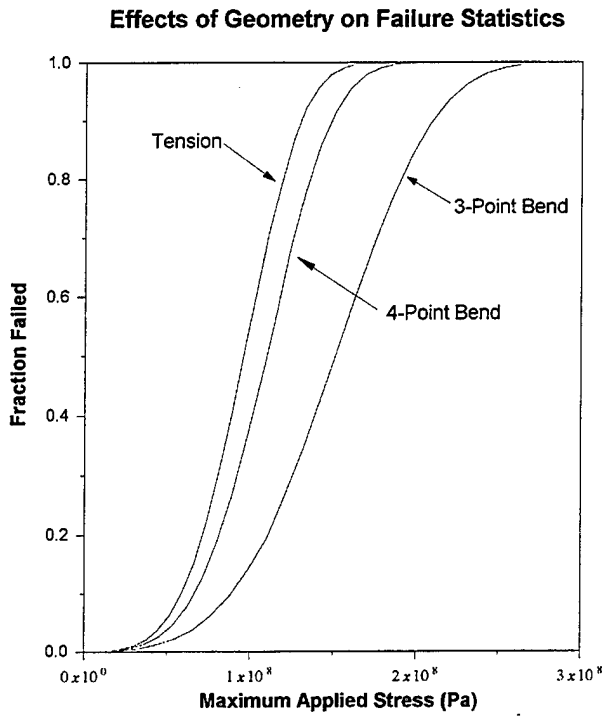

Figure 6.4. Comparison of statistical behavior for various geometries.

6.4 Batch Four Tests

Tests were conducted on the fourth batch in 3-point bending with a span, S, of ≈20 mm. Results from these tests are shown in Fig. 6.5 along with the results from batch three tests. With the exception of two tests, batch four tests exhibited significantly lower failure stresses than those of the previous batch, i.e., the newest samples mostly being less than 10% of the batch three strengths. The failure locations in these tests were noticeably grouped at 9-11mm from the Mo-rich end. This range lies appreciably away from the location of maximum applied tensile stress which suggests that this region had a significantly more severe flaw population. Crack paths in the fractured specimens uniformly indicated the existence of pre-existing flaws 3 - 5 mm long. Those few which failed at loads more typically expected were apparently free of these defects.

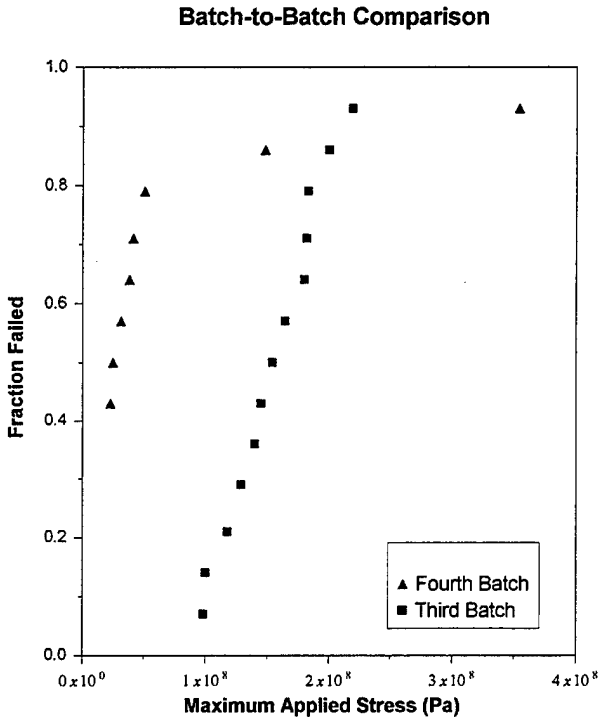

Figure 6.5. Comparison of batch three and batch four test results.

6.5 Residual Stress Effects

Effects of the residual stress from the 662 gradient are included in the plots of Fig. 6.6 where failure probability as a function of maximum applied bending stress is calculated for cases with and without residual stress. The effects can be seen, for this gradient, to be relatively small. This may be anticipated since these residual stresses are small compared to the strength in fast fracture.

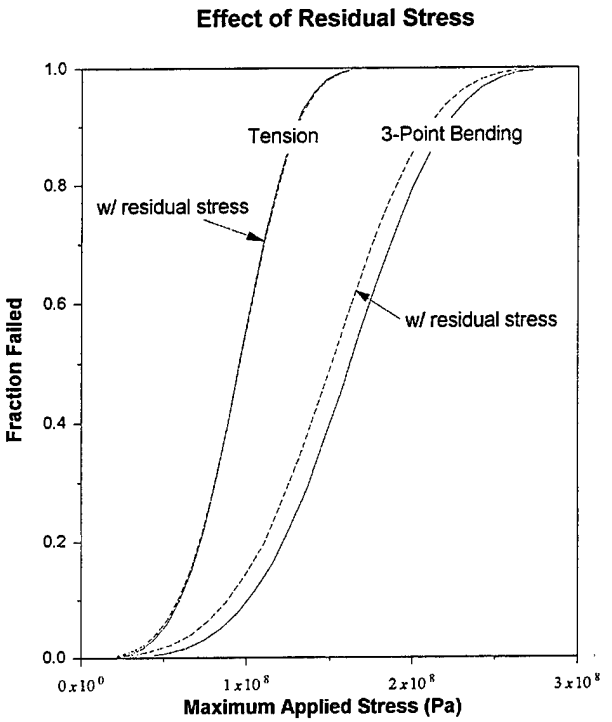

Figure 6.6. Effect of residual stress on the strength of the FGM.

The effect of residual stress states produced from different gradients is considered in Fig. 6.7, where the residual stresses from two batches, labeled gradients 321 and 662, are considered. Again there is a small but discernible effect.

6.6 Slow Crack Growth Effects

Susceptibility to subcritical crack growth (e.g., in the presence of water or water vapor) would be expected to accentuate the differences in residual stress states since the relatively higher stress levels associated with gradient 321 would allow much longer crack lengths to be attained. This is an important issue as it would allow a small flaw from surface damage to grow to much larger sizes under the higher residual stress fields of gradient 321. This gradient would lead to further degradation of strength than indicated by the computations in Fig. 6.6 which only includes fast fracture effects.

An estimate of the magnitude of this effect may be made by considering a reasonable threshold stress for slow crack growth as the average failure stress. As this stress is $\approx$ 1/3 the fast fracture stress for a wide range of glasses a provisional calculation may be made by adjusting the Weibull scaling parameter, σ_0, such that the average failure stress corresponds to the slow crack growth threshold (here considered to be 1/3 the fast fracture value). Results from these calculations are presented in Fig. 6.8. It is apparent

that the effect of the slow crack growth is much larger for relatively higher residual stresses of gradient 321 as compared to gradient 662.

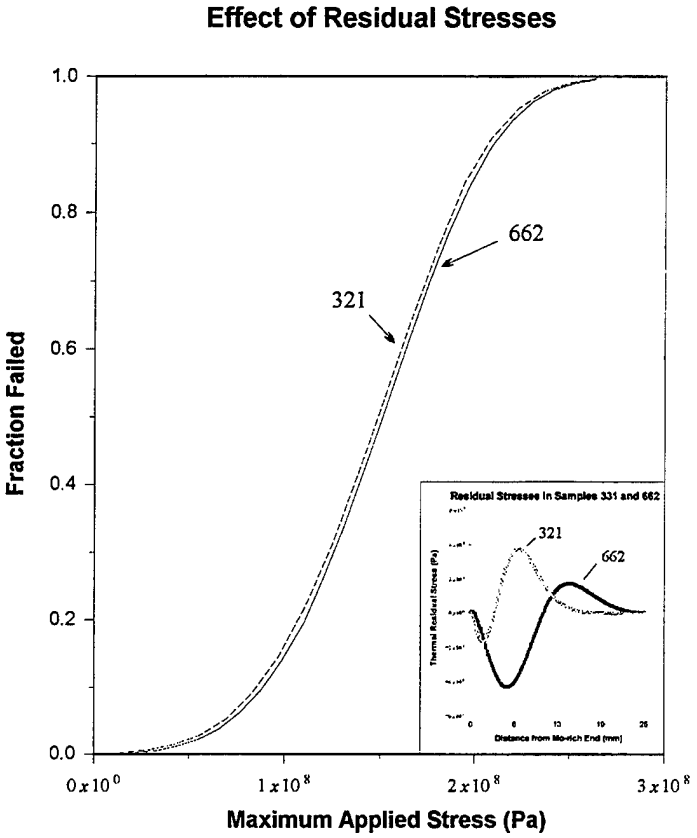

Figure 6.7. Effect of residual stresses from gradients 321 and 662 on failure characteristics.

The failure probability of an FGM component subjected only to cooldown (residual) stresses, σ_r, provides an estimate of the expected losses due to manufacture and handling. A simple calculation based on Eq. 6.2, considering the entire surface of the as-manufactured FGM with $\sigma = \sigma_r$, yields 6% rapid failure for components with gradient 321 while only 0.4% would be expected to fail in the case of gradient 662. Accounting for subcritical crack growth would increase the computed failure probabilities for both situations. As above, these effects are considerably greater for gradient 321 where an estimated 50% could be expected to fail due to subcritical crack growth versus only 5% for gradient 662 (again taking a reduction of the strength to 1/3 as plausible). Simple estimates of critical flaw sizes based on:

$$a_c = \left(\frac{K_c^2}{\pi \sigma^2} \right) \quad (6.3)$$

may be made for the FGM's that fail when subjected to cooldown stresses only. These estimates yield flaw sizes of ≈ 200 μm and 800 μm respectively for the gradients 321 and 662 (Fig. 5.4), respectively, under fast fracture conditions. However, considering the effects of slow crack growth, flaw sizes of only ≈ 20 μm for gradient 321 and ≈ 80 μm for gradient 662 would be able to grow subcritically in the residual stress fields present after cooling.

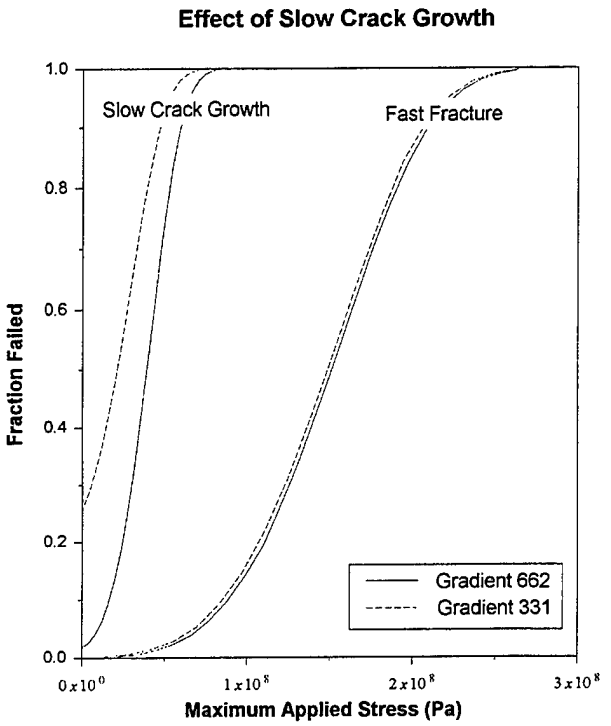

Figure 6.8. Effect of slow crack growth on failure characteristics of gradients 321 and 662.

6.7 Conclusions

A statistical approach has been employed to assess effects of geometry and residual stress on failure probabilities of an FGM composite. A key assumption is that, similar to bulk glasses, surface flaws are the dominant features controlling fracture strength. Although the two parameter model used here is simple, the calculations seem to account for observed trends in which the samples in the batch including #321 exhibited significant numbers of spontaneous fractures and were difficult to machine without further breakage. Accounting for slow crack growth both reinforces and accentuates the differences in expected behavior with changes in residual stresses.

Fracture stresses, compared under similar test conditions, are generally those typical of bulk glasses with the notable exception of one highly damaged area 9-11 mm from the Mo-rich end in the samples from the fourth batch. The origin of this damage, which corresponds generally to the region of highest surface tensile residual stresses, is unknown. Potential causes include the possibility of damage during proof testing, and/or changes in the starting powders, drying procedures or firing schedule, or possibly undetected damage arising from the thermal shock test administered to the latter samples.

7. Summary

The chemical analysis of Mo powders used for making FGMs indicated the presence of oxides of Mo in the as-received molybdenum powders. Although x-ray diffraction analyses of the Mo powders indicates only peaks of pure Mo, during annealing in H_2, the weight losses recalculated for MoO_2 correspond to an oxide content of 1.6 wt % for the 1.5 μm powder and 4.4 wt % for the 0.7 μm powder. The x-ray results are consistent with the presence amorphous Mo hydroxide in the as received powders. X-ray data of Mo powders which were annealed under vacuum clearly show the presence of MoO_2. Based on the relative size of the peaks, the amount of oxide is larger for the 0.7 μm powder. The presence of the oxide in the powder leads to loss of control of the Mo levels for three reasons – the erroneous measurement of Mo, the loss of Mo oxides by dissolution in water during processing and the loss of Mo when MoO_3 evaporates rather than being reduced during heating. It was determined that at the temperature range of 600 to 900 °C the weight losses for both powders were similar.

Thermal expansion measurements have been performed on TOTO fired and H_2 annealed FGM's in the direction perpendicular to the gradient. As expected, the thermal expansion of the both specimens increases with increasing Mo content, and the curves follow the gradient in the composition.

Average residual stresses arising from the gradient in thermal expansion were calculated for several conditions. Some of the calculations, addressed the actual gradients determined for different batches of TOTO samples, and others assumed systematic changes in the specimen dimensions or the composition gradients in order to elaborate the effects. In one series, the diameter of the sample was varied while maintaining the 662 type gradient; in another series, the form of the gradient was changed but with the same end values. As already reported, the standard 662 type sample has about 30 MPa of residual axial tension in one location along the surface, whereas the peak values from the earlier samples with the 321 gradient are nearly twice that value. Results for more recent samples showed further variations relative to the 662 gradient.

However, further calculations showed that varying the diameter, but maintaining the 662 gradient could lead to major effects, namely that the peak stresses dropped sharply with decreasing diameter, while they increased to asymptotic limits about twice as high as for the present case if the diameter is made very large. More importantly, it was shown that changing the details of the gradient can significantly change the axial variation and the magnitude of the stresses. Of particular importance are the well known

result that the stresses vanish if the gradient in thermal expansion coefficient is actually exactly linear. Moreover, it was found for a series of samples having an idealized situation of a composition profile giving a constant curvature that the surface stresses can be made almost entirely compressive if the curvature of the gradient is reversed relative to that typical considered in this project. Further series of calculations were done with a more realistic with a sigmoidal profiles. For both types of gradients, the results show the stresses increase strongly with the curvature of the composition profile.

Thus, this work identifies the curvature of the composition profile, both in sign and magnitude, as key determinants of the residual stresses. This is in contrast to the steepness of the gradient being the important parameter; the curvature seems to provide a basis for the intuitively expected result that steep gradients give higher stresses for sigmoidal profiles. Better appreciation of these effects combined with better control of the form of the gradient could lead to significantly improved situations regarding residual stresses.

Modeling has treated the statistical variability of strength including the affects of the average residual stresses, and, thereby, reflecting the affects of different gradients. The available data indicate a low Weibull modulus for these materials. This helps rationalize how the strengths from three point bend tests are higher than expected for normal glass. In addition, the results indicate how the expected effects of the residual stresses on strength would be minor if only fast fracture were important. However, with the more detrimental gradients, the residual stresses are high enough to cause spontaneous fracture of a few samples immediately upon cooling and even more when effects of subcritical crack growth are considered. The latter is an almost unavoidable consequence of ambient humidity. These results provide a rational for the difference in susceptibility to spontaneous failure or fracture during handling for the various batches of samples made at TOTO for examination at LBNL.

Most of the last batch of samples tested were exceptionally weak, i.e., 5-10% of expected values, but with a few samples exhibiting normal behavior. The cause of this is presently being evaluated, but the effect seems to be too high to ascribe simply to the affect of the residual stresses. These samples had been given a thermal shock pretest which may account for the larger flaws, or there may be a presently unknown change in processing.

Finally, using the composite thermal expansion coefficient, an estimate of the mismatch stresses at the interface between the FGM and a bonded tungsten wire were made, giving rather high stresses, ~ 200 MPa. These are high enough to provide concern for reliability despite the volume of materials under peak stresses being rather small. The results suggest that increasing the Mo content in the FGM to 60 vol % would eliminate these; but even increasing the Mo content to above 40 % would be helpful. Although experience may indicate that FGM's with such high Mo contents are extremely fragile, the computations on gradient optimization indicate that with attention to the form of the gradient, such materials could be made with acceptably low residual stresses, assuming further processing flaws did not evolve.

Report Number (14) LBNL--40886

Publ. Date (11) 199709

Sponsor Code (18) 02S , XF

JC Category (19) UC-000 , DOE/ER

DOE